Validation of super-resolution 4Pi-microscopy, and its application to the study of intra-Golgi transport

Thesis

UNRESTRICTED

Validation of super-resolution 4Pi-microscopy, and its application to the study of intra-Golgi transport.

Giuseppe Perinetti

Discipline: **Life Sciences**

Sponsoring establishment: **Consorzio Mario Negri Sud**

Thesis submitted in accordance with the requirements of

the Open University for the Degree of Doctor of Philosophy

Submission date: 6 October 2008
Date of award: 8 January 2009

CD AND ARTICLES HAVE BEEN
EXCLUDED
CONTACT UNIVERSITY

To my Parents

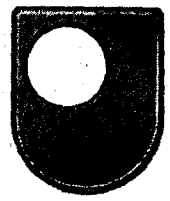

The Open University

ARC12
(September 2007)

RESEARCH SCHOOL

Affiliated Research Centre Programme

Library Authorisation

Please return this form to the Research School, The Open University, Walton Hall, Milton Keynes, MK7 6AA with the two bound copies of the thesis to be deposited with the University Library. All candidates should complete parts one and two of the form. Part three only applies to PhD candidates.

Part One: Candidate Details

Name: Giuseppe Perinetti PI: X7146005

Degree: PhD Affiliated Research Centre: Consorzio Mario Negri Sud

Thesis title: "Validation of super-resolution 4Pi-microscopy, and its application to the study of intra-Golgi transport"

Part Two: Open University Library Authorisation

I confirm that I am willing for my thesis to be made available to readers by The Open University Library, and that it may be photocopied, subject to the discretion of the Librarian.

Signed: ..... Date: February 2, 2009

Part Three: British Library Authorisation [PhD candidates only]

If you want a copy of your PhD thesis to be available on loan to the British Library Thesis Service as and when it is requested, you must sign a British Library Doctoral Thesis Agreement Form. Please return it to the Research School with this form. The British Library will publicise the details of your thesis and may request a copy on loan from the University Library. Information on the presentation of the thesis is given in the Agreement Form.

Please note the British Library have requested that theses should be printed on one side only to enable them to produce a clear microfilm. The Open University Library sends the soft bound copy of theses to the British Library.

The University has agreed that your participation in the British Library Thesis Service should be voluntary. Please tick either (a) or (b) to indicate your intentions.

(a) ☒ I am willing for The Open University to loan the British Library a copy of my thesis. A signed Agreement Form is attached.

(b) ☐ I do not wish The Open University to loan the British Library a copy of my thesis.

Signed: ..... Date: February 2, 2009

An electronic version of this form can be downloaded from http://www.open.ac.uk/research/research-degrees/affiliated-research-centre-programme/affiliated-research-centres.php

\\jensen\H_RDT\VAXM\ARC Programme\Forms\ARC12.doc

Abstract

Two problems have hampered the use of light microscopy for structural studies of cellular organelles for a long time: the limited spatial resolution, and the difficulty of obtaining true structural boundaries from complex intensity curves. The advent of modern super-resolution light-microscopy techniques and their combination with objective image segmentation now provide us with the means to bridge the gap between light and electron microscopy in cell biological applications. This study provides the first comparative correlative analysis of three-dimensional (3D) structures obtained by 4Pi-microscopy with those of transmission electron microscopy (TEM). The distribution within the cisternae of isolated Golgi stacks of the cargo protein PC3-pEGFP is here mapped in 3D by both 4Pi-microscopy and TEM for a detailed comparative analysis of their imaging capabilities. A high correlation was seen for these structures, demonstrating the particular accuracy of 4Pi-microscopy. Furthermore, for the first time, the transport of a cargo molecule (VSVG-pEGFP) through individual Golgi stacks (labelled by GalT-venusYFP) is visualized at the 4Pi-microscope super-resolution level. Following the procedures validated by the correlative analysis, the transport experiments show that: 1) VSVG-pEGFP rapidly enter/exit individual Golgi stack; 2) VSVG-pEGFP never fills the GalT-venusYFP compartment completely; and 3) the GalT-venusYFP compartment volume increases upon VSVG-pEGFP arrival. This morphological evidence supports some previous TEM-based observations of the intra-Golgi transport of VSVG-pEGFP and provides new insights towards a better understanding of protein transport across the Golgi stack. This study thus demonstrates the general applicability of super-resolution 4Pi-microscopy coupled with the zero-crossing-based segmentation technique for structural studies of sub-organelle protein distributions in living cells.

Table of contents

Chapter 3. Results

Chapter 4. Discussion

List of Tables

List of Figures

Chapter 1. Introduction

1.1 Conventional and super-resolution 4Pi- fluorescence microscopy

Where not indicated otherwise, all of the information reported below is from (Pawley, 2006).

1.1.a. Principles of light microscopy

The greatest advantage of visible light microscopy is that it allows non-invasive 3D imaging of living cells at the submicron scale with high specificity. Catalysed by the advent of GFP technologies and by a myriad of fluorescent tags, fluorescence microscopy in different variants has become the most popular light microscopy technique in cell biology. The principle behind fluorescence microscopy is that when a fluorescent sample is illuminated with light of the correct wavelength (in the absorption spectrum of the fluorochrome), it will produce an emitted light of a longer wavelength that can be detected using a charge-coupled device (CCD) camera. The camera thus acquires a 2D image of the emitted light intensity.

However, like any other conventional imaging system relying on focused light, all these microscopes are limited in spatial resolution because the smallest possible spot size is dictated by diffraction. Other limitations reside in the light emitted from out-of-focus regions that cannot be completely distinguished from the light emitted from the in-focus light. Therefore the image will be a combination of a sharp, focused image of the in-focus plane, with a blurred image of the out-of-focus light (although confocal microscopes reduce this phenomenon significantly, see below). Therefore, even after having removed the out-of-focus light, the highest achievable resolution in conventional microscopy is ~200 nm in the imaging (XY) plane, meaning that two fluorescent objects of the same kind cannot be distinguished if they are lying closer together than 200 nm. The same applies to fluorescent objects that are lying on the

axial (Z) direction. In this case, they can only be distinguished if their axial distance is at least ~500 nm, and this axial resolution is also referred to as the optical sectioning ability. The reason for this disparity between the XY-plane and Z-axis resolutions arises from the principles of optical physics and the microscope settings. In more detail, in any fluorescence microscope, there is an objective lens, the function of which is to focus a laser beam onto the focal point (structure of interest), and to ensure constructive interference of the focused wavefront at this focal point (**Figure 1.1**). Constructive interference means that the electric field of the light coming from all different angles (regions of the lens) is in phase synchrony and therefore produces a tiny, but finite, main spot of light around the focal point, which is mathematically described by the point spread function (PSF) which is the main brick that builds up the whole acquired image and is the image of a single point object. In more detail, the PSF is a function that measures the output (emitted light) of the optical system (exiting light) for an input point source. In digital imaging, the PSF is thus a function measuring the intensity of the pixels of a given object along a single or two spatial dimensions (**Figure 1.2**).

A theoretical PSF function (curve) is characterised by Gaussian behaviour with a maximum and two inflection points (IPs, where the slope of the curve is highest). A further important parameter is the full width at half maximum (FWHM), which is a measure of the width of the PSF at a level the intensity of 50% of the maximum (**Figure 1.2**).

However, although the light source may be a point, the corresponding image is not. There are two main reasons for this: 1) aberrations in the optical system that will spread the image over a finite area; and 2) diffraction effects that will also spread the image, even in a system that has no aberrations. The degree of spreading of the PSF in the image of this point object is a measure for the quality of an optical system, i.e. the larger the PSF (or greater the FWHM), the more blurred the image.

A more localised PSF will always produce a higher resolution image. Ernst Abbe discovered that the focal spot size decreased as the microscope aperture α angle (the half of which is also refereed as the Pi-angle, **Figure 1.1**) was increased, i.e. the larger the angle of the spherical wavefront that is produced by the objective lens, the smaller is the resulting PSF and the higher is the resolution (Abbe, 1873). However, lenses produce only a segment of a spherical wavefront that inevitably originates only from one side of the focal plane. As a result, the focal spot is longer (along the Z-axis, ~500 nm) than it is wide (on the XY-plane, ~200 nm) (**Figure 1.1**).

In more detail, a common (although not the most precise) way to express the spatial resolution limits in light microscopy is to look at the FWHM of the PSF (of a given structure of interest). If identical fluorescent molecules are within the FWHM distance, they cannot be separated in the resulting image. In this view, improving spatial resolution is the same as reducing the FWHM of the PSF. The FWHM of the PSF thus depends mainly on the wavelength of the exiting light (λ) and on the refractive index (*n*), rather than the aperture α angle. Regarding the resolution on the XY-plane, for instance, this dependency is FWHM $\approx \lambda/(2n \cdot \sin\alpha)$, as discovered by Abbe more than a century ago (Abbe, 1873). However, for highly convoluted structures, such as the Golgi complex, this axial sectioning will not be enough to achieve a satisfactorily resolution. This is, for instance, one of the reasons why many aspects of intra-Golgi transport are still difficult to study (see also **Section 1.4**). Moreover, when dealing with living-cell recording, another important issue in fluorescence microscopy is time resolution (i.e. the time required to acquire consecutive images).

Fluorescence microscopy includes a large series of settings based on confocalisation, single- or multi-photon excitation and other recent super-resolution developments. All of these techniques rely on the use of fluorescent probes.

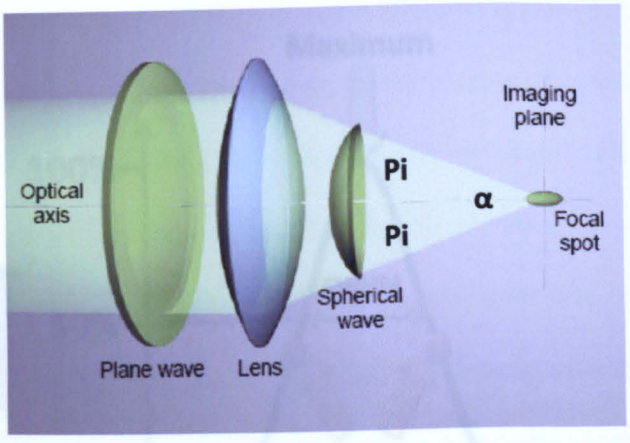

Figure 1.1. Schematic representation of the focusing process in fluorescence microscopy. A laser beam propagates along the optical axis. The plane wavefront of the beam is converted by a lens into a segment of a spherical wavefront and therefore focused onto the focal point, which lies in the imaging plane. As the focusing process is unidirectional (here from left to right), the focal spot is longer (axial direction) than wide (lateral direction). At a larger angle of the spherical wavefront (**α**), this corresponds a smaller (shorter) PSF. **Pi** refers to the Pi-angle, which is, by definition, half of the α angle (i.e. 2·Pi = α). **Optical axis** refers to the Z-axis. Note the elongation of the focal spot along the Z-axis. Adapted from (Egner and Hell, 2005).

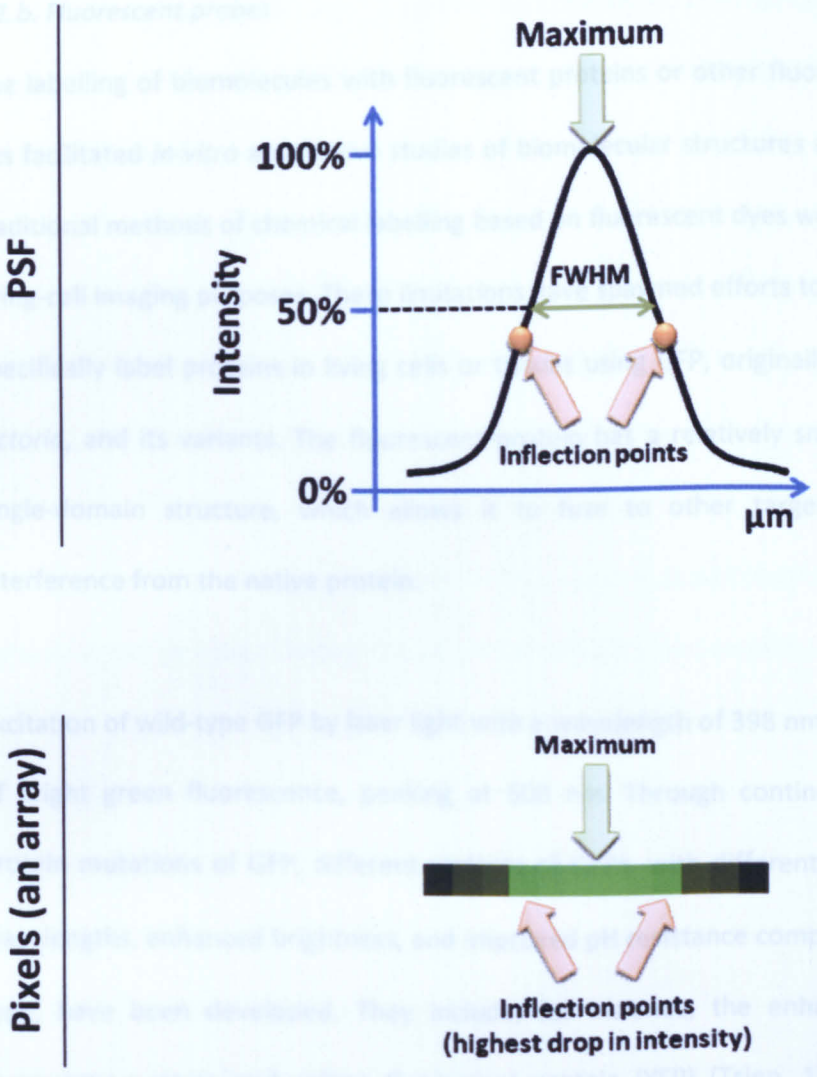

Figure 1.2. Representation of a theoretical PSF and the corresponding array of pixels. A theoretical PSF has a maximum intensity, two inflection points (in which the slope of the curve is highest), and a full width at half maximum (FWHM). In the corresponding array of pixels, the inflection points correspond to the highest drop in intensity.

1.1.b. Fluorescent probes

The labelling of biomolecules with fluorescent proteins or other fluorescent tags (as probes) has facilitated *in-vitro* and *in-vivo* studies of biomolecular structures and dynamics. However, traditional methods of chemical labelling based on fluorescent dyes were often inadequate for living-cell imaging purposes. These limitations have spawned efforts to non-invasively and site-specifically label proteins in living cells or tissues using GFP, originally cloned from *Aequorea victoria*, and its variants. The fluorescent protein has a relatively small size and a compact, single-domain structure, which allows it to fuse to other targeted proteins with little interference from the native protein.

Excitation of wild-type GFP by laser light with a wavelength of 398 nm can induce the emission of bright green fluorescence, peaking at 508 nm. Through continuous efforts to perform protein mutations of GFP, different variants of GFPs, with different excitation and emission wavelengths, enhanced brightness, and improved pH resistance compared to the original wild-type, have been developed. They include, for instance, the enhanced GFP (EGFP), cyan fluorescent protein and yellow fluorescent protein (YFP) (Tsien, 1998). In particular, later generations of YFP mutants, including the venusYFP (Nagai et al., 2002), were also developed. These variants exhibit greater resistances to low pH, greatly improved photo-stability, brighter fluorescence, and faster maturation.

1.1.c. Confocal fluorescence microscopy

A confocal fluorescence microscope has an increased resolution by rejecting the out-of-focus light, which would be fully detected in conventional optical microscopy (also referred to as wide-field microscopy). The confocal principle suppresses all of the structures that fall outside of the focal plane using an aperture (detection pinhole), which is placed in the beam path in an optically conjugated plane to the point light source. Therefore, using confocal fluorescence

microscopy, optical sectioning is possible. For acquisition of an image in the focal plane, the sample is scanned with a point laser beam in the XY-plane. Moving the sample along the Z-axis allows 3D imaging.

A basic confocal laser scanning microscope consists of a microscope stand, the scan head and the lasers. In particular, here the scan head contains not only the focusing lens (as set in **Figure 1.1**), but also the detection pinhole for suppression of the out-of-focus light. In particular, the diameter of the pinhole is variable and a combination of the diameter of the pinhole, the wavelength and the numerical aperture of the objective determines the axial dimension of the optical section (see also above). The detection unit collectes specifically the light(s) of different wavelengths emitted from the sample. The different emissions from the individual fluorochromes (fluorescent probes) are optically separated and fed to separate photomultipliers.

1.1.d. Single- and multi-photon fluorescence microscopy

Fluorescence is a phenomenon in which absorption of (exciting) light by a fluorochrome is followed by the emission of the (emitted) light of longer wavelength. In traditional fluorescence, a single photon is used to excite a fluorochrome from its ground state to an upper energy state, the excited state. When returning to the ground state, a photon of a lower energy (i.e. of longer wavelength) is emitted and can be detected as fluorescent light. The same fluorochrome can be repeatedly excited and detected. The principle of multi-photon fluorescence is based on the simultaneous absorption of two or multiple long wavelength photons by a fluorochrome to reach the excited state. Each multiple absorption induces a molecular excitation of a magnitude equivalent to the sum of the absorbed photon energies. In the case of two-photon excitation, the sample is illuminated with a wavelength around twice that of the absorption peak. For instance, the simultaneous absorption of two red photons

(each 980 nm) is equivalent to that of a single blue photon (490 nm), and the emission spectrum remains unchanged. Importantly, the phenomenon of multi-photon excitation occurs only in a very restricted spatial focus, i.e. emitted fluorescent light originates only from the focal plane. Due to this phenomenon, a confocal pinhole is not necessary for multi-photon fluorescence microscopy.

Multi-photon fluorescence microscopy is an imaging technique that has significant advantages, such as a reduction in the loss of light (allowing imaging from deep structures, even within a tissue block) and avoidance of out-of-focus bleaching. On the other hand, bleaching and photo-damage (i.e. protein denaturation) in the in-focus plane have been reported to be greater in multi-photon then in single-photon excitation (Drummond et al., 2002). Therefore, to carry out multi-photon microscopy successfully, it is recommended to use low excitation rates, so that the photo-damage caused by exposing the sample to intense light can be reduced. While most conventional confocal microscopy is based on single-photon excitation, the 4Pi-microscope relies on two-photon excitation (see below).

1.1.e. 4Pi-microscopy

Principle and setting

As mentioned above, the resolution along the Z-axis of any fluorescence microscope using a single focusing lens (including the confocal version) is limited by diffraction, to ~500 nm. While an improvement by up to a factor of two can be achieved by mathematical deconvolution (i.e. a process that eliminates blurring, see below), a substantial improvement of the axial resolution requires a change in the physics of the imaging. Therefore, new methods have been developed very recently to overcome these limitations, with one of these new technologies being 4Pi-microscopy. 4Pi-microscopy is based on the principle that two coherent laser beams focused on the same object produce a sharper signal or PSF (for a review, see Hell, 2007; 2003). Indeed, by focusing two laser beams on an objective through two opposing lenses (each having a 2Pi-angle) a doubling of the total aperture angle of each of the laser beams is achieved, by giving a total 4Pi-angle. However, while the excitation light comes from the two sides of the sample, the emitted light can be collected from a single side (Type A 4Pi-microscope), or from both sides, and again coherently combined at the detector (Type C 4Pi-microscope). A comparison of the 4Pi-microscopy principle with that of conventional confocal microscopy is shown in **Figure 1.3**, with the Type A 4Pi-microscope set-up shown in **Figures 1.4** and **1.5**. Of note, 4Pi-microscopy improves the resolution only along the Z-axis, while the resolution along the XY-plane remains the same as conventional confocal microscopy. However, the fundamental reduction in the thickness of the optical sections yields significantly improved perception of details in the focal plane. Under 4Pi-microscopy recording conditions (i.e. exciting λ of 870 nm, emitted λ of 510 nm, n = 1.33 [water immersion] and a semi-aperture aperture α angle of ~65°), the axial resolutions are of ~150 and ~105 nm in Types A and C, respectively. A further slight improvement of these resolutions is achieved by deconvolution (see below).

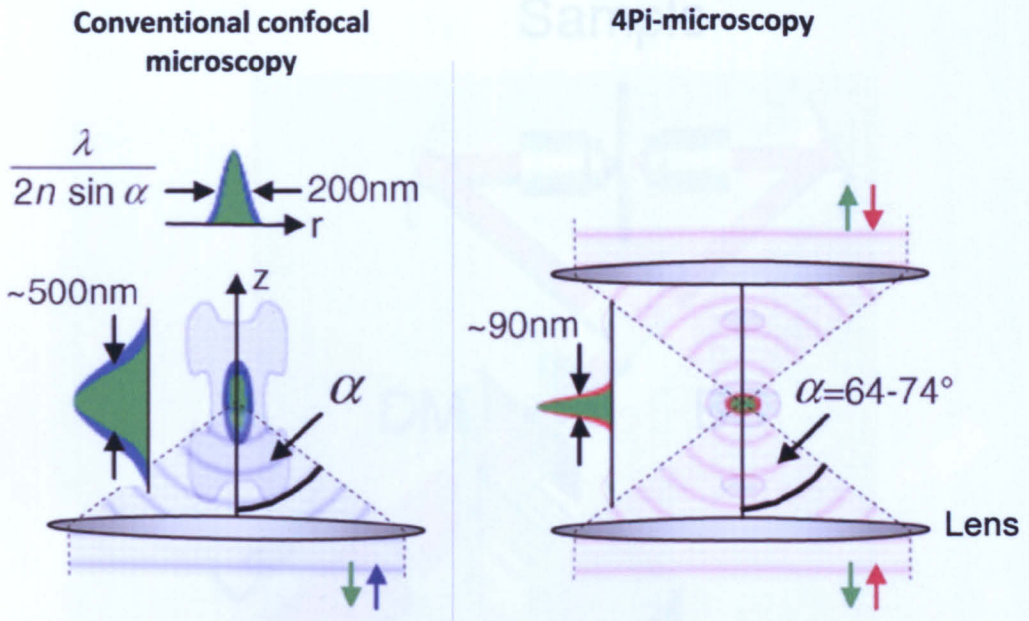

Figure 1.3. A comparison of conventional confocal microscopy and 4Pi-microscopy set-ups, and their corresponding PSFs.

Confocal microscopy: the blue and green arrows indicate the exiting and emitted light, respectively. The excitation light passing though the focusing lens is focused on the focal spot. A point-like detector (not shown) registers fluorescence mostly from the main maximum (shown in green), thus slightly improving the resolution. Nevertheless, confocal microscopy resolution is limited by diffraction to ~200 nm in the focal (XY) plane and to ~500 nm along the axial plane (Z-axis). **4Pi-microscopy**: the red and green arrows indicate the exiting and emitted light, respectively. By combining the wavefront caps of the two opposing lenses, 4Pi-microscope produces a narrower spot along the Z-axis, and hence an improved resolution of ~100 nm in both the XY-plane and the Z-axis. **λ**, laser wavelength; **α**, semi-aperture angle of the lens (in this case the equivalent of the Pi-angle); **n**, refractive index. The emitted light can be collected from a single (Type A) or from both (Type C) sides. Note that a conventional confocal microscope, with a single focusing lens, is a 2Pi-microscope; on the contrary, the 4Pi-microscopy takes its name from the 4Pi-angle derived from the two opposing lenses (each having a 2Pi angle). Adapted from (Hell, 2007).

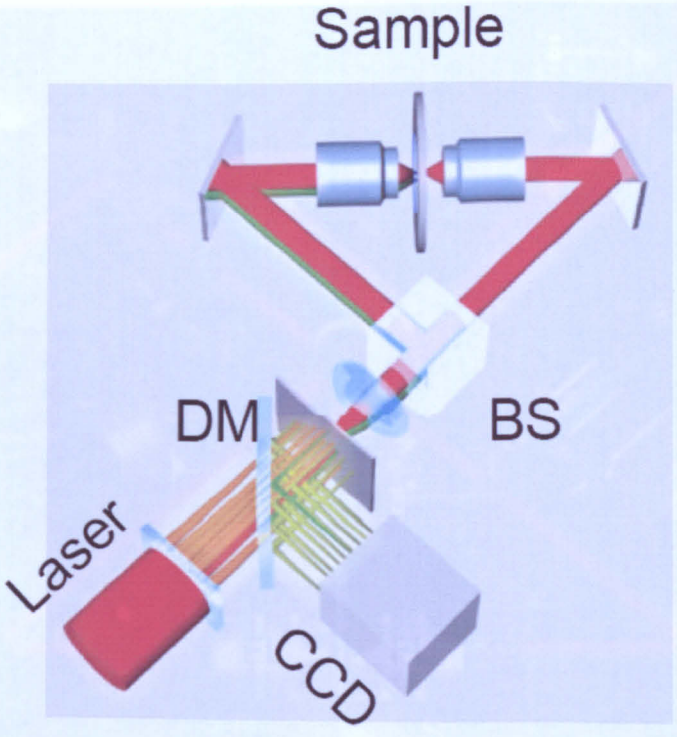

Figure 1.4. Diagram of the Type A 4Pi-microscope set-up for living-cell imaging.

The sample is placed between the two opposing (water-immersion) lenses that are jointly used for two-photon excitation, with up to 64 pairs of 4Pi-spots (MMM-principle). These spots are produced by splitting an array of pulsed laser beams at the beam splitter (**BS**). The exiting light (red) is then focused on the object (focal spot) through the opposing lens. Emitted light (green) from the spot (sample) is imaged onto a charge-couple device (**CCD**) camera, after being deflected by a dichroic mirror (**DM**). Note that the emitted light is collected only from one side of the sample. Adapted from (Hell, 2003).

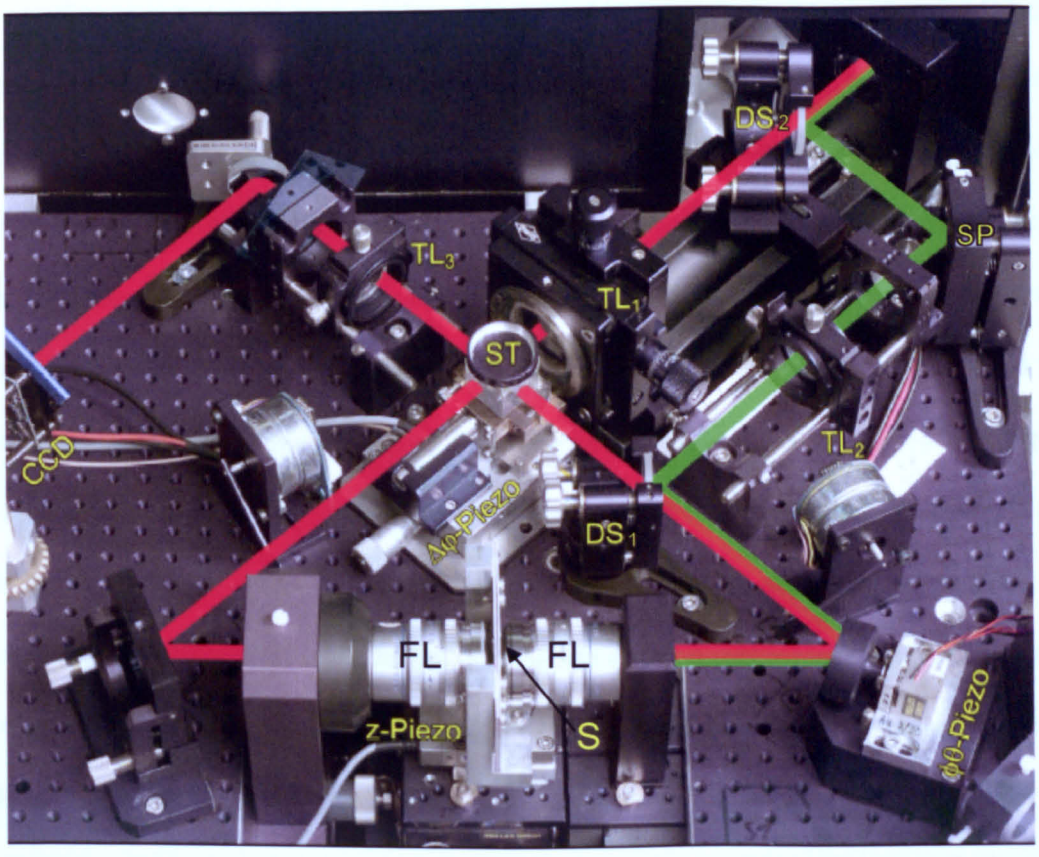

Figure 1.5. The Type A 4Pi-microscope core.
The exiting light (red) is splitted at the beam splitter (**ST**) and then focused on the sample (**S**) through the two focusing lenses (**FL**). The emitted light (green) on one side of the sample is then collected in a detector (not shown). The piezo-mechanical stages (**Piezo**) allow fine beam calibration, monitored through the charge-coupled device camera (**CCD**). **TL**, tubular lens; **DS**, dichroic mirror; **SP**, mirror. Courtesy of Stefan W. Hell.

The recording at super-resolution requires, however, a reduced pixel size, to allow for the gain in resolution. If the imaged surface/volume is kept constant, an increase in the resolution in one direction by a factor of N results in an increase in the acquisition time by a factor equal to N^2, thus notably reducing the time resolution of the 4Pi-microcope. This can be counteracted by investigating smaller regions, or by using a multifocal variant of the 4Pi-microscope, referred as multifocal multiphoton 4Pi-microscope (MMM-4Pi) (Egner et al., 2002). Here the recording process is performed by up to 64 4Pi-foci in parallel on the same XY-plane (**Figure 1.4**). Indeed, the combination of the MMM-principle with 4Pi-microscope has resulted in a fast axially super-resolving microscope (Egner et al., 2002; Egner et al., 2004). Moreover, the potential crosstalk between neighbouring exciting and emitted foci, which would compromise the resultant imaging, was seen not to be significant in a quadratic grid arrangement, whereby the 4Pi-foci are separated from each other by at least $3.5 \cdot \lambda$ of the excitation laser beam (~ 2.8 μm). Both the Types A and C 4Pi-microscopes (**Figure 1.4**) are MMM-4Pi, although they are always referred to as 4Pi-microscopes.

Importantly, the interference of spherical wavefronts that produce a sharper focal spot (referred to as the main lobe) comes at the expenses of some artefacts. In particular, the laser interference produces so-called side lobes, which are located at about half a wavelength above and below the focal plane (**Figure 1.6**). Moreover, these (primary) side lobes are accompanied by weaker periodic lobes that increase in height with decreasing aperture α angle of the focusing lens. Since the intensity of these periodic side lobes is within the range of the background signal, they do not associate to noticeable effects on the image. Instead, the side lobes produce ghost images that have to be removed by mathematically processing the data by a deconvolution procedure (see below). An explicative comparisons of the simulated PSFs obtained in standard confocal microscopy and 4Pi- microscopy (raw and deconvolved) is shown in **Figure 1.7**. In particular, by overlapping the PSFs of the confocal and 4Pi-

microscopy, it can be seen that and the main and side lobes of the latter would be fully inscribed into the PSF obtained in former technique.

The accuracy with which these ghost images can be removed depends on: 1) the relative height of the side lobes compared to the main peak; and 2) the distance between the side and main lobe peaks (**Figure 1.6**). As a rule of thumb, the side lobe height should never exceed ~50% of the main lobe (which thus represents the structure of interest). Unfortunately, the available water-immersion lenses all feature an aperture α angle < 68° (and ~65° in the 4Pi-microscope setting), so that in the best case, the side lobe height is not below 60% of the main lobe. However, efficient optical techniques for side lobe reduction in 4Pi-microscopy recording have been implemented. They include: 1) confocal detection; 2) two-photon excitation; and 3) combined interference of the excitation and the detection wavefront pairs (Type C). The principles by which these techniques suppress the side lobes are summarised in **Table 1.1**.

The use of two-photon excitation together with confocal detection has been part of the 4Pi-microscope since its initial stages of development (Hell and Stelzer, 1992a). On the contrary, the Type C approach is technically the most demanding, and has only recently been developed. Indeed, the optical set-up has to be designed such that the exiting light interferes at the sample (as in the Type A) and also at the detector. The two-photon Type C 4Pi-microscope thus combines all three mechanisms and thus features the lowest achievable side lobes, making the subsequent image restoration process (see below) easier and more reliable (Gugel et al., 2004). Additionally, Type C 4Pi microscopy obtains a ~30% better resolution than its Type A counterpart (Gugel et al., 2004). Unfortunately, the Type C variant still suffers very poor time resolution, making its application in living-cell imaging not feasible, at present.

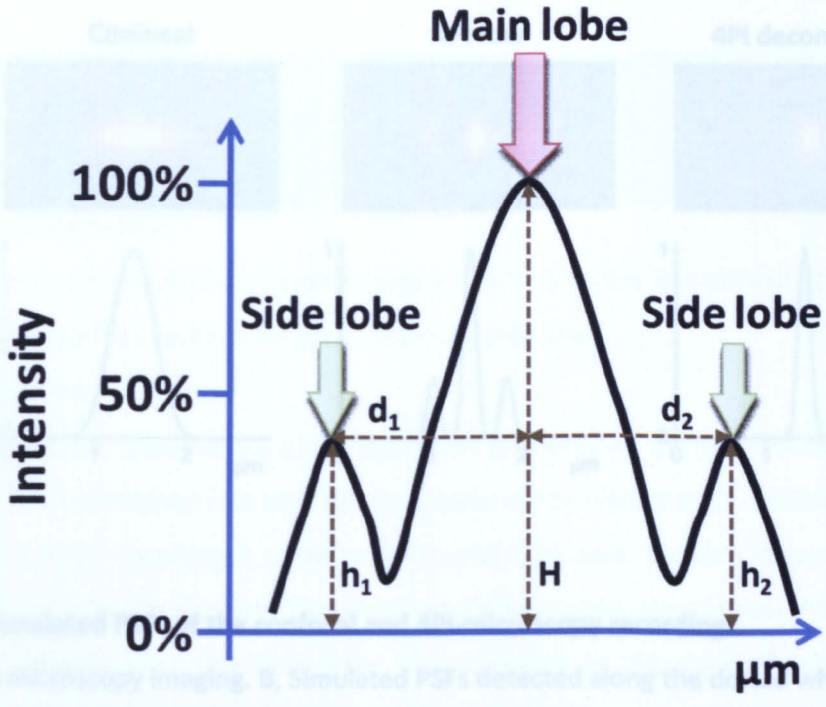

Figure 1.6. Diagram of the 4Pi-microscopy PSF.

The laser interference produces a main lobe representing the structure of interest, and primary side lobes above and below the focal plane (the X axis of this diagram and of the following represent the optical [Z] axis of the focal spot). Periodic side lobes are not shown for clarity. $\mathbf{h_1}$ and $\mathbf{h_2}$ represent the heights (intensities) of the side lobes; **H** represents the height of the main lobe. As a rule of thumb, the heights of the side lobes should never exceed ~50% of those of the main lobe. $\mathbf{d_1}$ and $\mathbf{d_2}$ represent the distance between the main and side lobes. In a theoretical and symmetrical PSF $h_1 = h_2 \leq 0.5 \cdot H$, and $d_1 = d_2$.

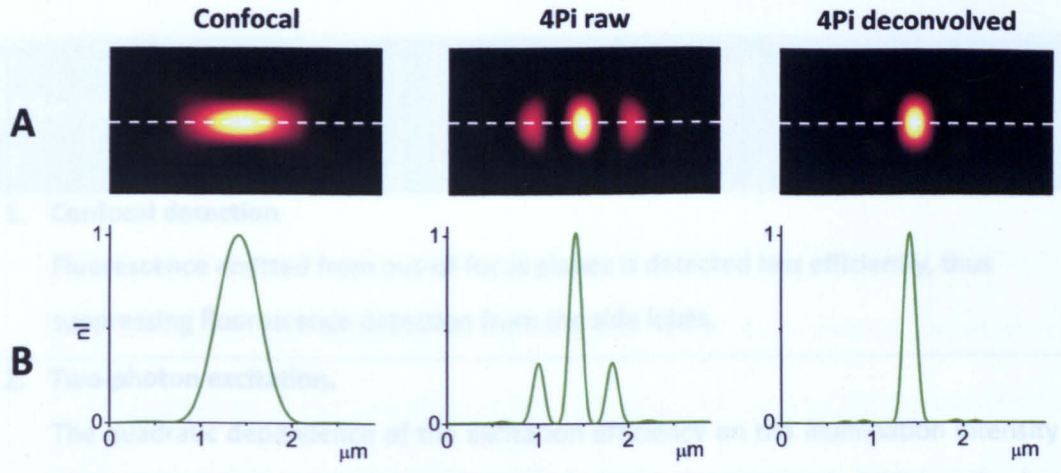

Figure 1.7. Simulated PSFs of the confocal and 4Pi-microscopy recordings.

A, Simulated microscopy imaging. **B**, Simulated PSFs detected along the dotted white lines in A. **IP**, inflection point (of maximum slope); **nI**, normalised intensity. For real PSFs, compare this **Figure** with **Figure 3.18**.

Side lobe-reduction technique
1. Confocal detection Fluorescence emitted from out-of-focus planes is detected less efficiently, thus suppressing fluorescence detection from the side lobes.
2. Two-photon excitation. The quadratic dependence of the excitation efficiency on the illumination intensity lowers the excitation side lobe height relative to the central peak. Additionally, due to the longer wavelength of the near-infrared light used, the side lobes are shifted away from the focal plane. Therefore, as the side lobes are of lower intensity and more distant from the main lobe (as compared to the case of single-photon excitation), they are better suppressed by the pinhole.
3. Combined interference of the excitation and the detection wavefront pairs (Type C). The side lobes of the excitation and detection PSFs show a peak at different points in space. Since the effective PSF is a product of the two at the detector level, the side lobes cancel each other out; on the contrary, the main lobes of the excitation and detection PSFs are the same, thus yielding to a resultant reinforced main lobe (Gugel et al., 2004). This effect is particularly pronounced when two-photon excitation is used (Gugel et al., 2004; Hell and Stelzer, 1992a)

Table 1.1. The most efficient side-lobe-reduction techniques and their principles in 4Pi-microscopy.

The refractive index problem

The investigation of biological samples normally requires mounting them in a medium with a refractive index that is usually different from that of the immersion system. This disparity introduces spherical aberrations, which depend strongly on the differences between the various refractive indices, and also on the focusing depth. While it is still possible to work with a conventional confocal microscope for strong refractive index mismatches as long as imaging is limited to regions close to the coverslip surface, this is not the case for microscopes that use two opposing objective lenses with a high aperture angle. In such cases, the objective lenses must be coupled with immersion medium where the refractive index of which has to be as close as possible to that of the sample (Egner et al., 1998). This prevents blurring (noise) and high side lobes. For living-cell imaging, a direct consequence is that water-immersion lenses must be used.

The reason for which minimal refractive index mismatches along the optical path produce unreliable imaging in 4Pi-microscopy is related to the principle of laser interference. Indeed, the PSF of the 4Pi-microscope strongly depends on the relative phase of the interfering wavefronts (Hell, 2003) which has to be constructive to have sharp main and side lobes (**Figure 1.8**). The opposite situation is completely destructive interference, which will produce a PSF characterised by two main lobes that cannot be deconvolved (see below).

In more detail, constructive laser interference is achievable if the two opposing paths are symmetrical (Schrader et al., 1998) and if the lasers coming from the two objective lenses pass through mediums (immersion and mounting) that have homogeneous and very similar refractive indices. Regarding the first issue, the symmetry of the opposing paths, the 4Pi-microscope core has been properly designed with two interferometric symmetric arms, along with a series of piezo-mechanical stages (to which mirrors or beam splitters are connected),

which allow fine laser beam calibration (**Figure 1.4**). Regarding the second issue, the refractive indices, only incomplete control can be obtained (see below). To limit mismatches, the objective lenses are of the water-immersion type and the mounting medium (which is a cell-growth medium) has 3.4% of total weight dextran added, to increase the refractive index up to 1.34 (Egner et al., 2004). This condition was shown to lead to better imaging conditions when using water media (Egner et al., 2004).

Three-point deconvolution in 4Pi-microscopy

Three-point deconvolution is among the procedures for image restoration. Such image restoration refers to a general mathematical operation that is aimed at the recovering of an original signal from an image that is degraded by blurring and noise. In fluorescence microscopy, the blurring is largely due to the diffraction-limited imaging of the instrument, while the noise is usually derived from an impairment in photon excitation. Three-point deconvolution can: 1) remove noise; 2) increase contrast; and 3) increase resolution, mainly along the Z-axis. Since axial imaging performance is the prime reason for researchers to invest in expensive optical microscopes, the ability to increase the axial resolution with a software technique has considerable value. However, while deconvolution may be helpful, although not necessarily in confocal microscopy, it is a fundamental procedure in 4Pi-microscopy for the removal of the side lobes (see above).

An efficient method for side-lobe removal is known as linear three-point deconvolution. The two main parameters for three-point deconvolution are: 1) the relative height (as a percentage of the maximum intensity) the side lobes have to be suppressed; and 2) the distance between the side and main lobes (**Figure 1.6**). Of note, in the linear deconvolution procedures like the three-point procedure, these parameters are kept constant over the whole volume of the recording (a series of XY-images along a Z-axis). Any variation in the PSF features (i.e. lack of

spatial invariance; see below) in the sample would produce areas of poor fitting with the selected deconvolution parameters, yielding unreliable outcomes. Finally, the deconvolution required for side lobe removal also sets limits on the acceptable minimum SNR, and if necessary, a method to achieve an adequate SNR is to slow the recording. This is due to the concept that although more reliable then other methods, this deconvolution procedure unfortunately results in an increase in the SNR after processing (Schrader et al., 1998).

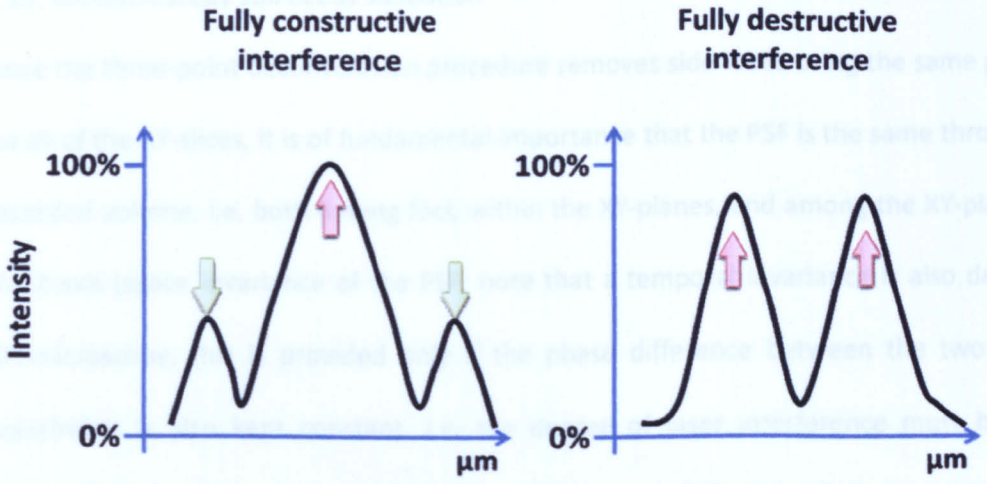

Figure 1.8. A comparison of fully constructive and fully destructive laser beam interference in 4Pi-microscopy, as seen by the PSF.

In fully constructive interference, the main lobe (red arrow) and the two (primary) side lobes (green arrows) are present in a symmetrical arrangement (periodic lobes not shown). In fully destructive interference, two main lobes (red arrows) are present. In real recording, any situation in between these two extremes is possible (i.e. variable degrees of constructive interference).

1.1.f. 4Pi-microscopy still needs validation

Since the three-point deconvolution procedure removes side lobes using the same parameters for all of the XY-slices, it is of fundamental importance that the PSF is the same throughout the recorded volume, i.e. both among foci, within the XY-planes, and among the XY-planes within the Z-axis (space invariance of the PSF; note that a temporal invariance is also desirable). In 4Pi-microscopy, this is provided only if the phase difference between the two interfering wavefronts is also kept constant, i.e. the degree of laser interference must be not only constructive, but also the same for the whole volume of the recorded structure of interest; indeed, any random change in phase would cause the PSF to vary greatly within the same recording, making the following deconvolution procedure dramatically less reliable. Therefore, the best conditions to achieve constructive laser interference must be maintained throughout the optical paths and sample.

Only when the refractive index is constant over the whole sample can the degree of laser interference be controlled solely by the piezo adjustments. On the contrary, when this varies throughout the sample (as in actual samples), it is impossible to fully correct the PSF. In this regard, it has been shown that for glycerol-mounted fixed mammalian cells, the refractive index changes within the samples are minimal, allowing constructive laser interference (Hell et al., 1997; Nagorni and Hell, 1998). Indeed, the refractive index of glycerol (1.46) is close enough to those of the lipid membranes and proteins (1.48 and 1.54, respectively). Unfortunately, the satisfactory results obtained for glycerol-mounted samples cannot be extrapolated to living-cell recording, as the use of an aqueous medium is a requisite for cell viability. Of note, the refractive index of water (1.33) is further away from those of the cellular components. This mismatch increases the difficulty of countering the complex, inhomogeneous distribution of refractive indices within living cells, the precise control of which thus remains impossible. Any local variation in the refractive index of the sample, in

turn, affects the phase difference and the corresponding derived structure of the PSF (Blanca et al., 1998). This may cause limitations in the reliability of the derived imaging. Moreover, the water-immersion objective lenses that must be used for living cells have lower aperture angles as compared to those of oil- or glycerol-immersion lenses, and thus lead to greater sidelobes. In addition, the following three-point deconvolution becomes the crucial step, as residual sidelobes can lead to structural artefacts. Therefore, the complex distribution of refractive indices in a living cell (necessarily immersed in aqueous medium) has questioned the general applicability of 4Pi-microscope. Nevertheless, in a previous study (Egner et al., 2004), a full Golgi ribbon (labelled with a GFP tag) has been recorded in a living Vero cell with an interference pattern between the two opposing lasers judged to be constructive enough for reliable image restoration (**Figure 1.9**). As a limitation, in this study and others (Egner et al., 2004; Hueve et al., 2008; Medda et al., 2006; Plecita-Hlavata et al., 2008) on 4Pi-microscopy application in living/fixed cells (see also **Section 1.4**), the 3D reconstructions that were obtained were considered as artefact-free only relying on the PSF features, which has a certain degree of destructive interference in any real recording. Therefore, to determine more precisely to what extent the destructive interference (along with other general PSF features) can be considered acceptable in terms of image reliability requires more in-depth investigations. Moreover, image segmentations were performed in all of these previous studies using the standard threshold-intensity procedure, as set on a subjective basis (Egner et al., 2004; Hueve et al., 2008; Medda et al., 2006; Plecita-Hlavata et al., 2008). Therefore, the key issues that still have to be addressed in 4Pi-microscopy are: 1) whether the current recording and deconvolution procedures are reliable; and 2) whether the following image segmentation (and thus 3D reconstructions) can be made through a reproducible and objective procedure.

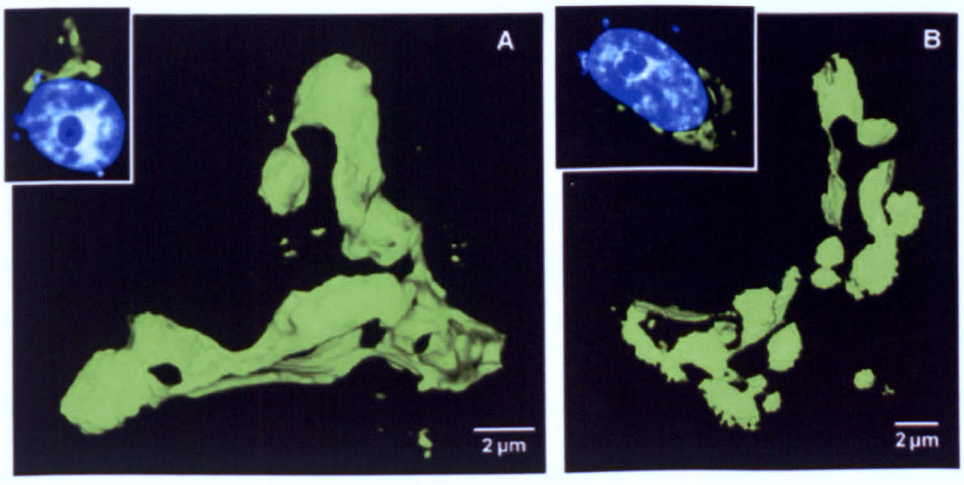

Figure 1.9. Type A 4Pi-microscopy recording of the Golgi complex in living cells.
Golgi complex labelled with GalT-venusYFP (**A**) and uronyl-2-O-sulfotransferase-pEGFP (**B**) in Vero cells at ~100 nm axial resolution. The insets show the epi-fluorescence images, to correlate the Golgi complex with the nucleus. The Hoechst staining of the nucleus indicates that the cells were in interphase. Adapted from (Egner et al., 2004).

1.2 Image processing in fluorescence microscopy

Where not indicated otherwise, all of the information reported below is from (Graf, 1999).

1.2.a The fundamentals of digital imaging

The word *pixel* derives from a contraction of *pix* (for "pictures") and *el* (for "element"); similar formations with *el* for "element" include *voxel*, which is a volume element, the 3D analogue of a 2D pixel. In digital imaging, a pixel is the smallest piece of information in an image. Pixels are normally arranged in a regular 2D grid, and are often represented using dots, squares or rectangles. Each pixel is a sample of an original image, where more samples typically provide a more accurate representation of the original. The intensity of each pixel is variable and the images are divided into greyscale, colour and binary, as detailed below.

Greyscale images

A greyscale (or greylevel) image is simply one in which the only colours are shades of grey. The reason for differentiating such images from any other sort of colour image is that less information needs to be provided for each pixel. In fact a 'grey' colour is one in which the red, green and blue components all have equal intensity in RGB (red - green - blue) space, and so it is only necessary to specify a single intensity value for each pixel, as opposed to the three intensities needed to specify each pixel in a full colour image.

Often, the greyscale intensity is stored as an 8-bit mode giving 256 possible different shades of grey from black to white. If the levels are evenly spaced then the difference between successive greylevels is significantly better than the greylevel resolving power of the human eye. Greyscale images are very common, in part because much of today's display and image capture hardware can only support 8-bit images. In addition, greyscale images are entirely

sufficient for many tasks and so there is no need to use more complicated and harder-to-process colour images.

Colour images

It is possible to construct (almost) all visible colours by combining the three primary colours red, green and blue, because the human eye has only three different colour receptors, each of them sensitive to one of the three colours. Different combinations in the stimulation of the receptors enable the human eye to distinguish approximately 350,000 colours. A RGB colour image is a multi-spectral image with one band for each of the colours red, green and blue, thus producing a weighted combination of the three primary colours for each pixel. Full RGB colour requires that the intensities of the three colour components (red, green and blue) be specified for each and every pixel. It is common for each component intensity to be stored as 8-bit, and so each pixel requires 24 bits to completely and accurately specify its colour. Image formats that store a full 24 bits to describe the colour of each and every pixel are therefore known as 24-bit colour images. In particular, using 24 bits to encode colour information allows 2^{24} (i.e. 16,777,216) different colours to be represented.

However, it is computationally expensive and often not necessary to use the full 24-bit image to store the colour for each pixel. Therefore, the colour for each pixel is often encoded in a single byte, resulting in an 8-bit colour image. The process of reducing the colour representation from 24-bits to 8-bits, known as *colour quantisation*, restricts the number of possible colours to 256. Visible differences between a 24-bit-color image and the same image displayed with 8 bits occurs, although this does not have significant effects in terms of image processing.

Binary images

Binary images are images where the pixels have only two possible intensity values. They are normally displayed as black and white. Numerically, the two values are often 0 for black, and either 1 or 255 for white. Binary images are often produced by thresholding a greyscale or colour image, in order to separate an object in the image from the background. The colour of the object (usually white) is referred to as the foreground colour. The rest (usually black) is referred to as the background colour. However, this polarity can be inverted, in which case the object is displayed with 0 and the background is displayed with a non-zero value.

1.2.b Image segmentation

In many vision applications, it is useful to be able to separate out the regions of the image corresponding to objects in which we are interested from the regions of the image that correspond to background. Therefore, segmentation refers to the process of partitioning a digital image into multiple regions (sets of pixels). The goal of segmentation is to simplify and/or change the representation of an image into something that is more meaningful and easier to analyse (Shapiro and Stockman, 1992). Image segmentation is typically used to locate objects and boundaries (lines, curves, etc.) in images. The result of image segmentation is a set of regions that collectively cover the entire image, or a set of contours extracted from the image (i.e. edge detection). Each of the pixels in a region is similar with respect to some characteristic or computed property, such as colour or intensity. Adjacent regions are significantly different with respect to the same characteristic(s) in such a way that they can be easily recognised and separated (Shapiro and Stockman, 1992).

In fluorescence microscopy (and in general digital imaging) two important entities must not be confused: noise and background. The former is expressed by the signal-to-noise ratio (SNR), which thus measures the roughness or granularity of the image, and which is independent of

the relationship between signal and background. The latter, the background, is a different type of spurious signal that is composed of electronic offset, scattered light, and light from aspecific labelled components. Of note, in fluorescence microscopy, the segmentation procedure is used to distinguish objects from background (and eventually to reduce the noise). Only after image segmentation can morphometric analyses (i.e. calculation of co-localisation between channels, or the volume of a given compartment) be performed.

Two ways of performing image segmentation are the threshold-intensity and zero-crossing procedures (although only the former has been extensively used in fluorescence microscopy). A step that is required before image segmentation, and especially when the zero-crossing procedure, is the smoothing. All of the segmentation procedures deal with the PSF of the image, which, in a real fluorescence microscopy image, is not only spread instead of point-like, but it is also affected by the noise and the background. By looking at the real PSF, the differences between the noise and the background become obvious, with the noise as the irregularity along the PSF profile at any intensity (**Figure 1.10**).

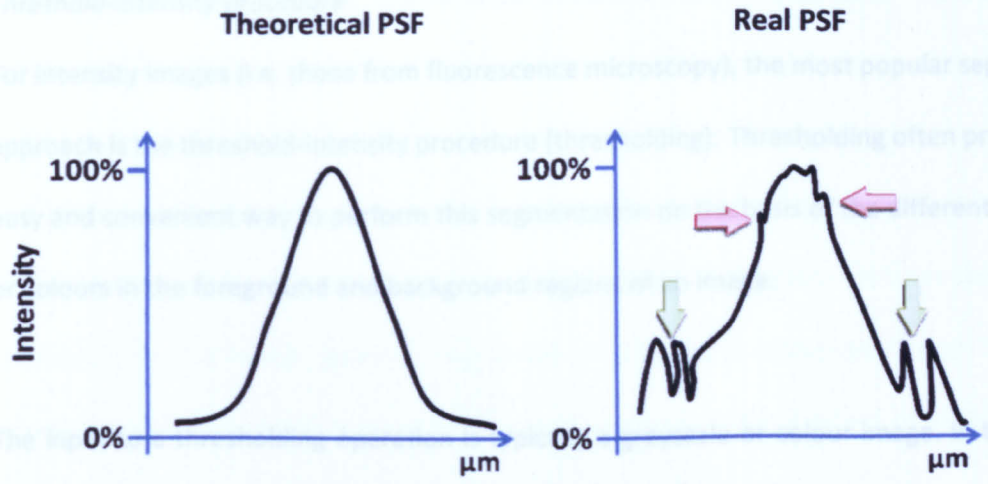

Figure 1.10. A comparison of a theoretical and a real PSF.

A theoretical PSF is a Gaussian curve. A real PSF is characterised by noise (red arrows) and background signals (green arrows). For clarity in this **Figure** and the followings, the noise is shown only on the upper part of the PSF.

Threshold-intensity procedure

For intensity images (i.e. those from fluorescence microscopy), the most popular segmentation approach is the threshold-intensity procedure (thresholding). Thresholding often provides an easy and convenient way to perform this segmentation on the basis of the different intensities or colours in the foreground and background regions of an image.

The input to a thresholding operation is typically a greyscale or colour image. In the simplest implementation, the output is a binary image representing the segmentation. Black pixels correspond to background and white pixels correspond to foreground (or *vice versa*). In simple processing, the segmentation is determined by a single parameter, known as the 'intensity threshold'. In a single pass, each pixel in the image is compared with this threshold. If the pixel intensity is higher than the threshold, the pixel is kept in the output; if it is less than the threshold, it is set to black (i.e. resorted to a null value) (**Figure 1.11**).

In more sophisticated implementations, multiple thresholds can be specified, so that a 'band' of intensity values can be set to white while everything else is set to black. For colour or multi-spectral images, it may be possible to set different thresholds for each colour channel, and so select just those pixels within a specified cuboid in RGB space. Another common variant is to set to black all those pixels corresponding to background, but leave foreground pixels at their original colour/intensity (as opposed to forcing them to white), so that information is not lost. In the microscopy approach, this last procedure is used when the co-localisation between two or three channels needs to be 'weighed' by the intensity of each co-localising pixel.

Such threshold-intensity procedures, which make decisions based on local pixel information, are effective when the intensity levels of the objects fall squarely outside the range of levels in the background. Because spatial information is ignored, however, blurred region boundaries

can create havoc. Importantly, the simplest threshold-intensity procedure has some specific limitations: 1) its subjective nature; and 2) the concept that the boundaries of the segmented images will be forced to have the same intensity (referred to as an isosurface) (see **Figure 1.12** and **Table 1.2**). An example of the dramatic effects of the threshold setting on the segmented 3D structure is shown in **Figure 1.13**. In spite of these limitations, the threshold-intensity procedure is the most popular segmentation technique nowadays used in confocal fluorescence microscopy to provide information regarding co-localisation, intensity/surface of a given structure/cell (Manders et al., 1993) (see also below).

The zero-crossing procedure

An edge-based method represents another segmentation procedure, and this is best known as the zero-crossing procedure. This technique arises from the concept that region boundaries (or edges) (within an image) and IPs (within the PSF) are closely related, due to the concept that there is often a sharp adjustment in intensity at region boundaries. Edge-detection techniques have therefore been used as one of the segmentation procedures. In more detail, the identification of the IPs on the PSF is based on the Laplacian, which is the 2nd derivative of the PSF itself (**Figure 1.11**). The Laplacian of an image highlights regions of rapid intensity change, and as such it is often used for edge detection. Therefore, the zero-crossing procedure does not assume the edges of the reconstructed structures to be located at the positions where the intensity has a certain value, as in the threshold-intensity method (**Figure 1.12** and **Table 1.2**), but assumes the edges to be located where the slope of the PSF is maximal.

Zero-crossing is a well-know procedure in the digital imaging field (Gonzalez and Woods, 1992), and was initially applied to biological research in spectrometry and fluorescence spectrophotometry (O'Haver, 1979). Of note, the zero-crossing procedure has never been proposed in segmentation of fluorescent microscopy images, except in two previous studies in

which, however, the potential of this method was not fully revealed, nor was there any proof of its reliability (Jaskolski et al., 2005; Raman et al., 2007) (see also below).

As a drawback, it is common that the zero-crossing points identified by the Laplacian occur not only at the edges of the images, but also at places that are not as easy to associate with edges of the main structures (i.e. the structure of interest). This is due to the susceptibility of the Laplacian to both noise and background (**Figure 1.10**). Thus it is common to see lots of spurious edges detected away from any obvious edges. Regarding the former, the noise, the starting point for the zero-crossing procedure has to be a smoothed image in which the noise has been reduced (see below). In particular, the stronger the smoothing is set, the more smaller features will be smoothed out of existence, and hence more edges will be removed (i.e. fewer zero-crossings will be produced). Regarding the latter, the background of a given image, this is also rich in IPs detected by the Laplacian. A proposed method to eliminate IPs from the background is to look at the gradient of the PSF at the zero-crossing (i.e. the third derivative of the original image) and to only keep the zero-crossings corresponding to PSF edges above a certain gradient. This will tend to retain only the stronger edges, but the third derivative will greatly amplify any high frequency noise in the image, as it is highly sensitive to noise.

The main limitations to the use of the zero-crossing procedure probably reside in these drawbacks, and in the technical difficulties in setting-up an experimental plan to show the reliability of the segmented images or 3D reconstructions.

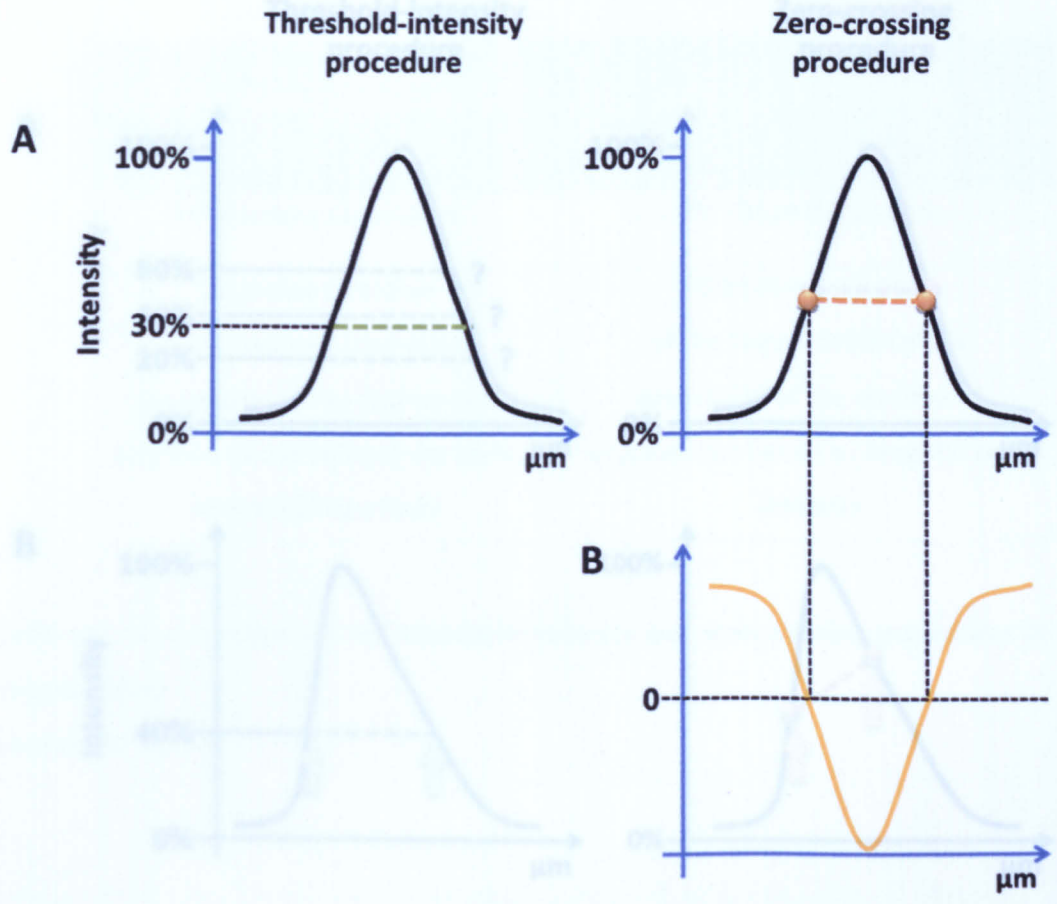

Figure 1.11. The principles of the threshold-intensity and zero-crossing procedures in image segmentation, as seen by the PSF.

The curves represent PSF in **A** and the corresponding second-derivative in **B**. In the threshold-intensity procedure, the segmentation plane (green line) is set according to a specific threshold value on the maximum intensity. In the zero-crossing procedure, the segmentation plane (orange line) connects the IPs on the two sides of the PSF. The IPs are the points with maximum slope, and their identification is based on the zero intersection of the second derivative (Laplacian) of the PSF. All of the pixels (or voxels) having an intensity above or equal to that of the segmentation planes are kept in the final (segmented) structure, the others are given a null value.

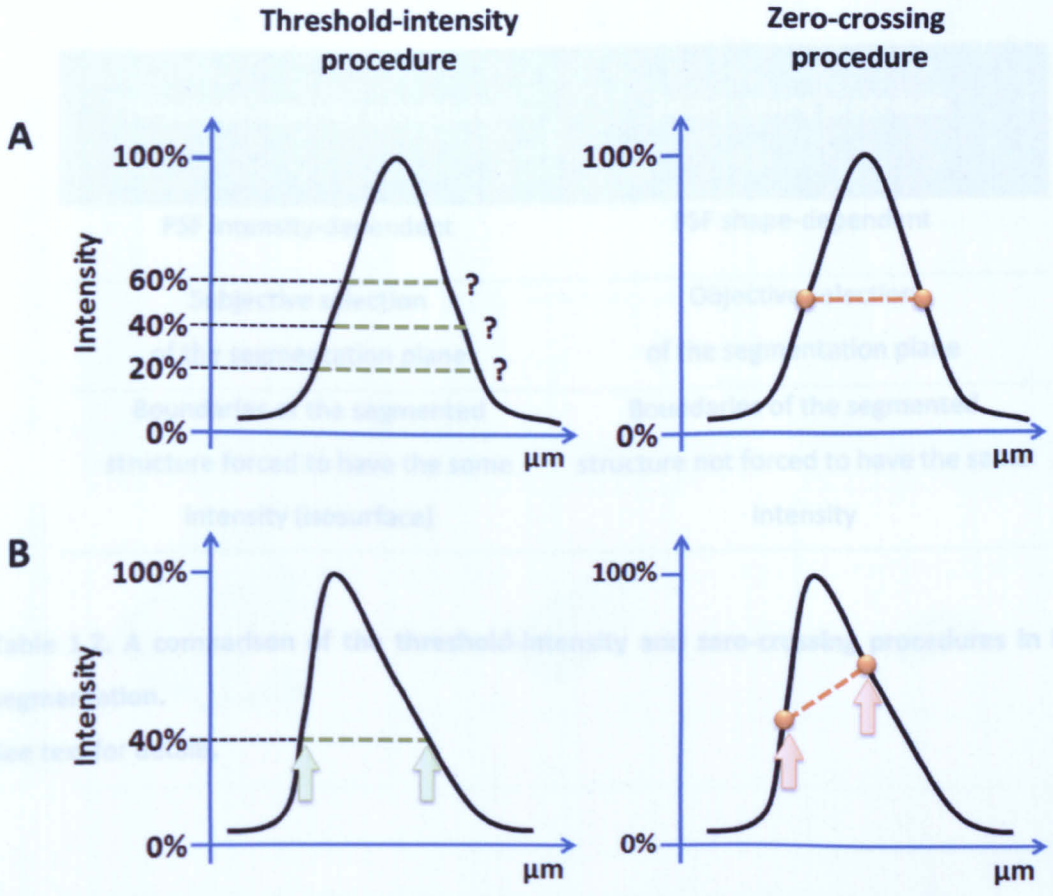

Figure 1.12. A comparison of the threshold-intensity and zero-crossing procedures in image segmentation, as seen by the PSF.

Curves in **A** and **B** represent the cases of a symmetrical (theoretical) and asymmetrical (real) PSF, respectively. A, In the threshold-intensity procedure, the choice of the cutting threshold on the maximum intensity leads to a segmentation plane (green lines) on a subjective basis. In the zero-crossing procedure, the identification of the IPs (orange circles) leads to a segmentation plane (orange line) on an objective basis. B, In the threshold-intensity procedure, as the cutting threshold leads to a segmentation plane with a fixed intensity (green line), the segmented structure will have boundaries forced to have the same intensity (green arrows). In the zero-crossing procedure, as the IPs may lie at different level of the PSF, the segmentation plane (orange line) may have variable intensities, and the segmented structure can have boundaries with variable intensity (orange arrows).

Threshold-intensity procedure	Zero-crossing procedure
PSF intensity-dependent	PSF shape-dependent
Subjective selection of the segmentation plane	Objective selection of the segmentation plane
Boundaries of the segmented structure forced to have the same intensity (isosurface)	Boundaries of the segmented structure not forced to have the same intensity

Table 1.2. A comparison of the threshold-intensity and zero-crossing procedures in image segmentation.

See text for details.

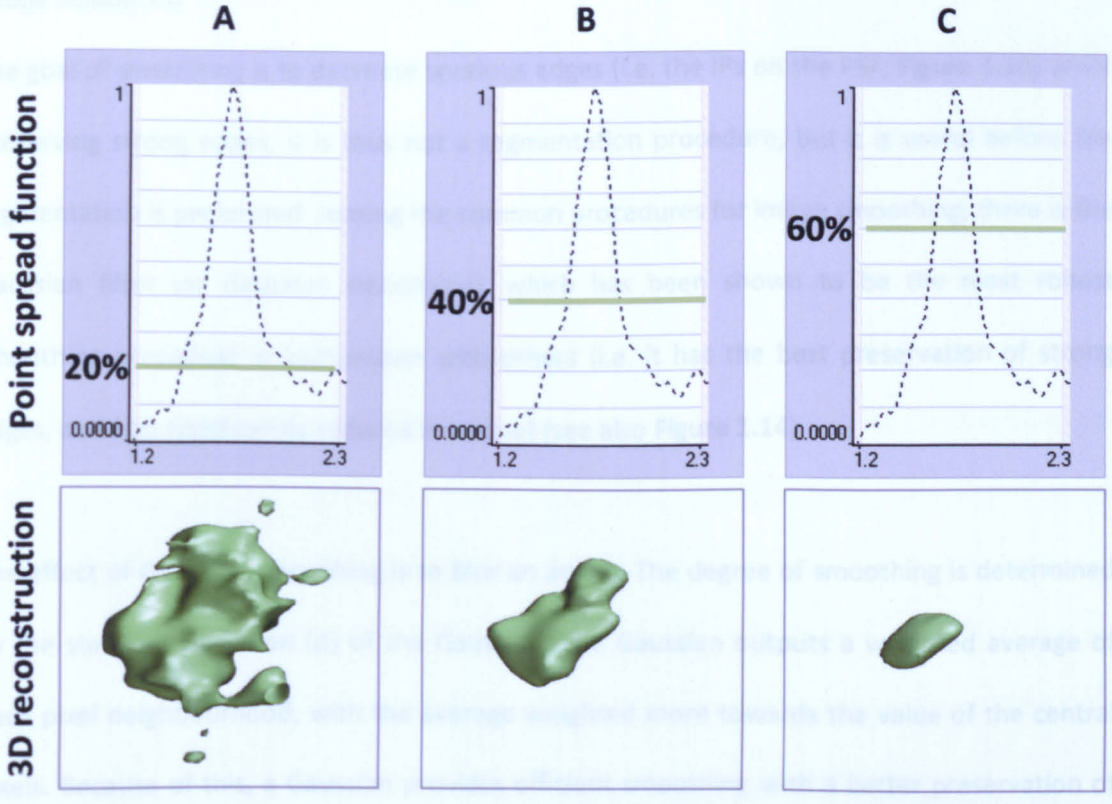

Figure 1.13. The dramatic effect of the threshold setting in the 3D reconstructions.
The same object (PSF) has been used for three 3D reconstructions with different thresholds (green lines), set as 20%, 40% and 60% of the maximum intensity (**A**, **B** and **C**, respectively). Note the dramatic differences between the resulting 3D reconstructions. This real data relates to Golgi stack 1 included in the experimental plan (see **Results**).

Image smoothing

The goal of smoothing is to decrease spurious edges (i.e. the IPs on the PSF; **Figure 1.10**) while preserving strong edges; it is thus not a segmentation procedure, but it is useful before the segmentation is performed. Among the common procedures for image smoothing, there is the Gaussian filter (or Gaussian smoothing), which has been shown to be the most robust smoothing procedure in comparison with others (i.e. it has the best preservation of strong edges, and also significantly reduces the noise) (see also **Figure 1.14**)

The effect of Gaussian smoothing is to blur an image. The degree of smoothing is determined by the standard deviation (σ) of the Gaussian. The Gaussian outputs a weighted average of each pixel neighbourhood, with the average weighted more towards the value of the central pixels. Because of this, a Gaussian provides efficient smoothing with a better preservation of edges from the main structures, as compared to other similar procedures. Hence, the σ value can be set to remove unwanted detail or noise as desired, with the strongest contours remaining even after heavy smoothing.

The outcome of the smoothing procedure also depends on the degree of image pixelisation (i.e. the dpi value). Indeed, keeping the σ value constant, the more the pixelisation, the more pronounced is the alteration introduced by the smoothing procedure. Therefore, it would be recommended to record images at low pixelisation (i.e. high dpi value). In this way, the smoothing procedure will be more efficient in removing disturbing edges on the PSF, while satisfactorily preserving its overall shape. In case, an image is heavily pixelated, an interpolation (a mathematical procedure which increases the dpi value) can be useful.

Co-localisation between fluorescent signals

Relevant data that can obtained from fluorescence microscopy is the co-localisation of ions, proteins, etc. Two types of methods have been proposed to calculate co-localisation between fluorescent signals: 1) coefficient-based intensity correlation; and 2) object-based approaches (for review, see Bolte and Cordelières, 2006). The former procedures, which can be automatic, use statistics to assess the relationships between fluorescence intensities, but loses morphological information. The semi-automatic procedures of the latter take into account the size, form and intensity distribution of the fluorescent signal to reproduce reliable image segmentation with a preservation of morphological features. Therefore, by using the intensity-correlation-coefficient-based approaches, the co-localisation data are easily calculated, but the data regarding area/volume of compartments, as well as how much of a given compartment is filled by another marker (and by which pattern), can only be obtained with all of the limitations reported above. As a consequence, information such as the degree of filling of a given Golgi complex compartment by a cargo crossing it, along with the morphological features of the compartment itself, can only be derived from object-based methods. These methods thus segment the image, and the remaining pixels are used to calculate the co-localisation coefficients, such as the Manders coefficients or others (for review, see Bolte and Cordelières, 2006).

Unfortunately, most of the co-localisation methods used nowadays are intensity-correlation-coefficient-based, such as the threshold-intensity procedure. Of note, recently a new automated threshold-intensity procedure has been presented (Costes et al., 2004). This method is based on the estimation of the maximum threshold of intensity for each colour below which pixels do not show any statistical correlation (Costes et al., 2004).

Edge detection procedures might then be proposed as object-based approaches, although these procedures have not been extensively used in co-localisation calculations. In this regard, a previous study (Jaskolski et al., 2005) used a specific edge-detection procedure (derivative approximation) based on the identification of the IPs of the first derivative of the PSF (not on the PSF itself). These IPs on the first derivative correspond to regions in the PSF where the signal increases or decreases with steep slope, and they are used to automatically define the region of interest, and ultimately to set a threshold value for image segmentation. This means that the final segmented image (or reconstruction) still relies on isosurface; moreover, the reliability of the final outcome, as for any other segmentation procedure, has not been tested for microscopy imaging. Of interest, the edge-based procedure that identifies the IPs on the PSF by using the second derivative (zero-crossing procedure, see above) has never been proposed for the calculation of co-localisation coefficients.

1.2.c Combination of the threshold-intensity and zero-crossing procedures as a new image segmentation technique has not still validated

To overcome the limitations of the threshold-intensity and zero-crossing procedures when used as individual segmentation techniques, a combination of the two after image smoothing can be proposed as a new procedure. Therefore, while the Gaussian smoothing will reduce of the noise, the initial thresholding will be useful to eliminate the background (see **Figure 1.14** and **Table 1.3**, for a comparison of their main effects on the PSF). Combining both of these procedures would thus eliminate all, or most, of the spurious signals, leaving the IPs of the main structure for the zero-crossing segmentation (**Figure 1.15**).

Of course, the choice of the parameters for both procedures (σ value and initial threshold) are still subjective. In this regard, the most critical issue is the initial thresholding, which will not interfere with the zero-crossing procedure if the IPs of the main structure lie on the PSF far enough from the background signal (**Figure 1.16**). If this is the case, then the initial thresholding would not include the IPs within an ample range of background cutting (i.e. up to 30% of the maximum intensity) (**Figure 1.16**).

However, while such a procedure has still to be validated under experimental conditions, both standard and super-resolution fluorescence microscopy would greatly benefit from a semi-automated segmentation procedure that can produce reliable outcomes. In particular, most benefits will be in the calculation of co-localisation between channels (i.e. proteins). which upon weighting of the intensity signal (i.e. segmented colour images), would be less influenced by spurious signals eventually remaining after the segmentation procedure (i.e. those from residual noise or background).

Finally, any co-localisation coefficient can be calculated after this segmentation procedure.

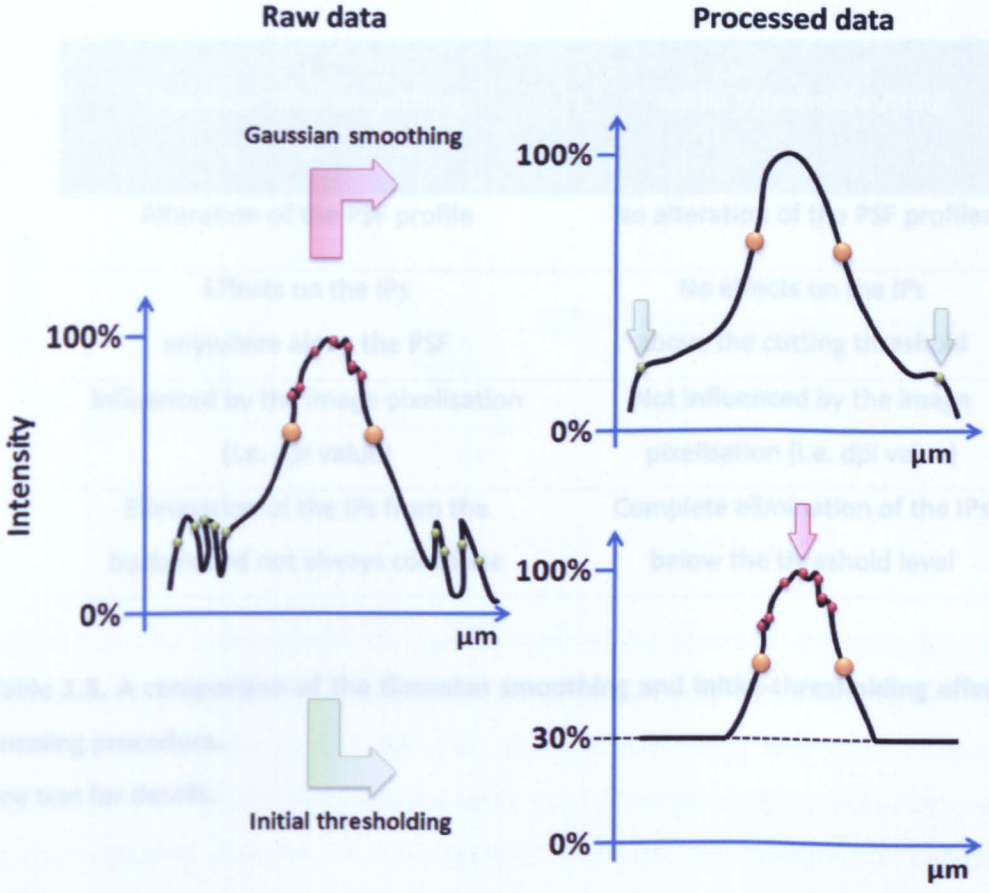

Figure 1.14. A comparison of the Gaussian smoothing and initial-thresholding effects in the zero-crossing procedure, as seen by the PSF.

Raw data refers to the real PSF, which has both noise (irregularities along its profile) and background signal. **Processed data** refers to the PSF after Gaussian smoothing (top) and initial thresholding (bottom). These noise and background signal have several IPs (red and green circles, respectively). In the Gaussian smoothing (processed data, top), the noise (and hence the number of IPs) is reduced; however, the shape of the PSF is slightly modified (according to the smoothing σ value) and IPs from background are never completely removed (green arrows). In the initial thresholding (processed data, bottom), all of the pixels below the cutting threshold (30% of the maximum intensity, in this example) are given a null value, and hence the corresponding IPs will not contribute to the segmented image. On the contrary, the pixels above this cutting threshold will be used in the zero-crossing procedure. This procedure has no effects on the IPs deriving from the noise above the cutting threshold (red arrow). Orange circles indicate IPs from the main structure.

Gaussian filter smoothing	Initial threshold cutting
Alteration of the PSF profile	No alteration of the PSF profiles
Effects on the IPs anywhere along the PSF	No effects on the IPs above the cutting threshold
Influenced by the image pixelisation (i.e. dpi value)	Not influenced by the image pixelisation (i.e. dpi value)
Elimination of the IPs from the background not always complete	Complete elimination of the IPs below the threshold level

Table 1.3. A comparison of the Gaussian smoothing and initial-thresholding effects in zero-crossing procedure.

See text for details.

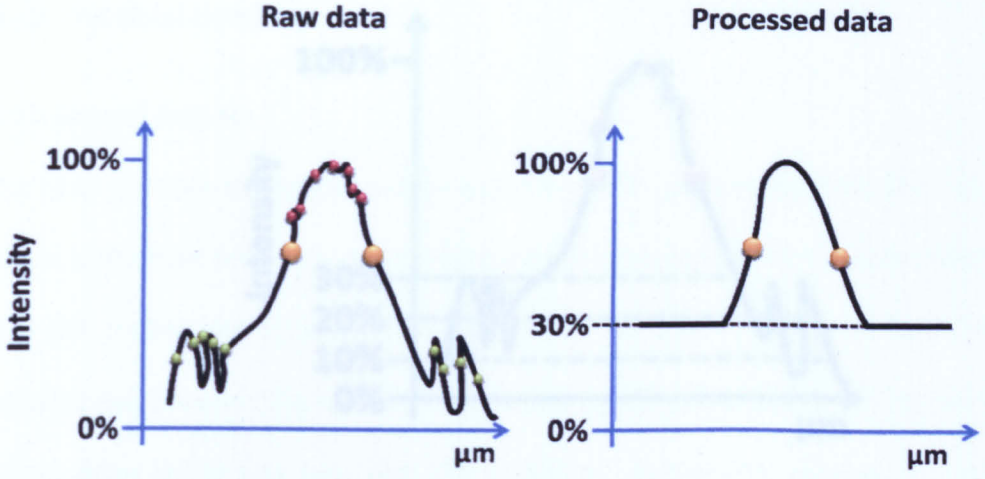

Figure 1.15. The principles of the combination of the threshold-intensity (and smoothing) and zero-crossing procedures, as a seen by the PSF, as a new image segmentation technique. **Processed data** refers to the PSF after Gaussian smoothing and initial thresholding. The Gaussian smoothing reduces the noise along the PSF profile while the initial thresholding (30% of the maximum intensity, in this example) eliminates the background. Finally, the zero-crossing procedure identifies the edges of the structure. The circles indicate IPs: orange, from the main structure; red, from the noise; green, from the background.

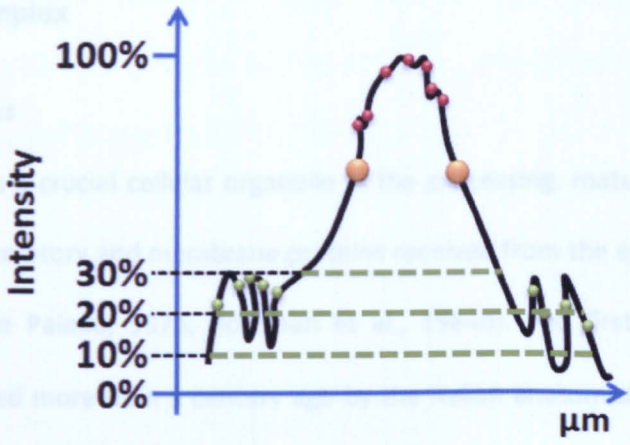

Figure 1.16. Hypothetical relationship between the locations of the IPs from the main structure and the others from the background, as seen by the PSF.

If the IPs of the main structure lie on the PSF profile far enough from the background signal, the initial thresholding would not include the IPs within an ample range of background cutting. As a result, the background is eliminated while the zero-crossing detection of the edges is not altered. The circles indicate IPs: orange, from the main structure; red, from the noise; green, from the background.

1.3 The Golgi complex

1.3.a General features

The Golgi complex is a crucial cellular organelle in the processing, maturation and sorting of newly synthesised secretory and membrane proteins received from the endoplasmic reticulum (ER) (for review, see Palade, 1975; Rothman et al., 1984b). The first report of the Golgi complex was provided more than a century ago by the Italian anatomist Camillo Golgi (Golgi, 1898). However, it was only with the advent of transmission electron microscopy (TEM) imaging that it became possible to initially establish the actual existence of the Golgi complex as an intracellular organelle (Dalton and Felix, 1954).

In mammalian cells, the Golgi complex is located around the centrosome (Rambourg and Clermont, 1990) and it is actively maintained there by its interaction with microtubules (Ho et al., 1989; Ho et al., 1990; Lippincott-Schwartz et al., 1998). In TEM images, the Golgi complex appears as a set of flattened parallel sacculi, called cisternae, that are arranged into several stacks. These stacks are associated with an array of small vesicles, as well as with tubules that are seen to emanate from both sides of the stacks (see below).

The morphological appearance of the Golgi complex indicates that it is composed of three main sub-compartments: the *cis*, medial and *trans* Golgi/*trans*-Golgi network (TGN) (**Figure 1.17A**) (Mellman and Simons, 1992). These sub-compartments are not only morphologically, but also functionally distinct areas. Indeed, the *cis* face receives proteins from the intermediate compartment (IC), and is involved in the retrieval of a subset of proteins back to the ER; it also has a role in the initial Golgi-specific carbohydrate addition and trimming reactions. The medial Golgi stack functions as a glycosylation compartment, where most of the addition and trimming of the carbohydrate moieties take place. The exit side of the Golgi

complex is the *trans* Golgi/TGN, which has an essential role in the final glycosylation reactions, the cleavage of propeptides, and the sorting of plasma-membrane (PM), lysosomal, and secretory proteins to their respective final destinations.

For a long time the isolated stacks were considered as the only essential components of the Golgi complex (Farquhar and Palade, 1981). However, more recently, a variety of approaches, including high resolution scanning electron microscopy, have allowed different groups to clearly demonstrate that the tubular-reticular areas that connect the adjacent stacks of the cisternae also have essential structural roles in Golgi organization (Clermont et al., 1994; Tanaka et al., 1986). Recent TEM tomography analyses have further confirmed this Golgi complex organization (Ladinsky et al., 1999; Marsh et al., 2001). Therefore, these studies have clearly shown that the Golgi complex is a single organelle that is characterised by two structural domains: compact regions (stacks of cisternae) that alternate with non-compact (tubular-reticular) regions (**Figure 1.17B**). The presence of these interconnections between adjacent stacks thus introduced the definition of a 'ribbon-like' Golgi network for the identification of the Golgi complex in mammal cells, where this organization is typically found (**Figure 1.17B**).

The Golgi complex has also a proteinaceous skeleton linking Golgi cisternae (Slusarewicz et al., 1994) that can also be seen at the TEM level and it is commonly referred to as the Golgi matrix. This contains a number of elongated, coiled-coil proteins of the golgin family (Barr and Short, 2003; Gillingham and Munro, 2003).

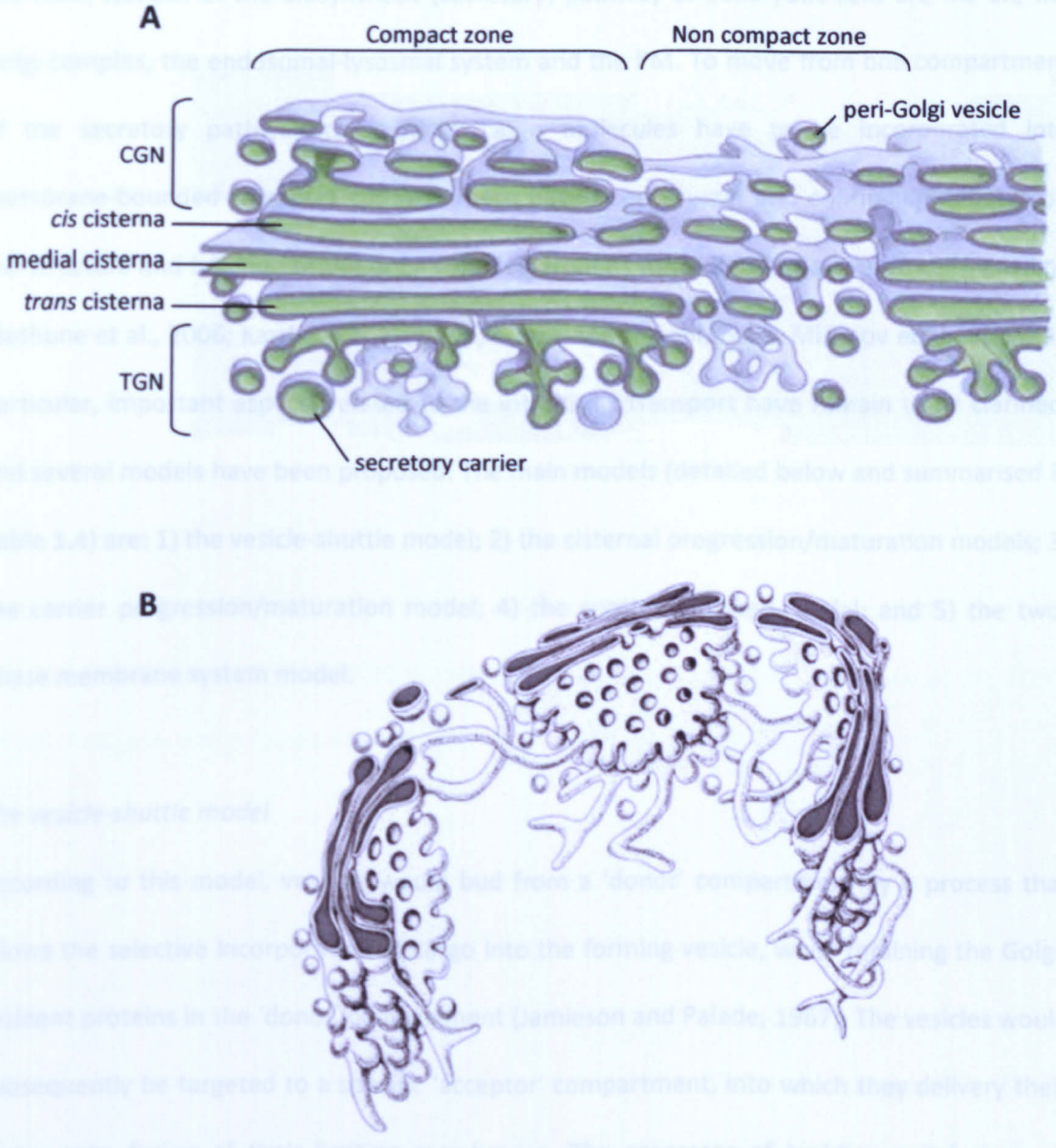

Figure 1.17. Diagrams of the Golgi complex.

A, Three-dimensional structure of the Golgi complex in a secretory animal cell, showing the compact and non-compact zones and their elements. The *cis*-face of the Golgi stack is that closest to the ER. The non-compact zones are made up of fenestrated saccules, and tubules bridge the cisternae of adjacent stacks (compact zones). **CGN**, *cis*-Golgi network, **TGN**, *trans*-Golgi network. Redrawn from (Rambourg and Clermont, 1990). **B**, Three-dimensional structure of the Golgi ribbon, showing three cisternal stacks connected by the non-compact zones. Modified from Krstic, 1972.

1.3.b Intra-Golgi transport

The main stations of the biosynthetic (secretory) pathway of eukaryotic cells are the ER, the Golgi complex, the endosomal-lysosmal system and the PM. To move from one compartment of the secretory pathway to another, cargo molecules have to be incorporated into membrane-bounded transport carriers. There have been several and continuing debates on the structure and function of the Golgi complex, from its formation to its roles in cell signalling (Bethune et al., 2006; Kartberg et al., 2005; Marsh and Howell, 2002; Mironov et al., 2005). In particular, important aspects related to the intra-Golgi transport have remain to be clarified, and several models have been proposed. The main models (detailed below and summarised in **Table 1.4**) are: 1) the vesicle-shuttle model; 2) the cisternal progression/maturation models; 3) the carrier progression/maturation model; 4) the continuity-based model; and 5) the two-phase membrane system model.

The vesicle-shuttle model

According to this model, vesicles would bud from a 'donor' compartment by a process that allows the selective incorporation of cargo into the forming vesicle, while retaining the Golgi-resident proteins in the 'donor' compartment (Jamieson and Palade, 1967). The vesicles would subsequently be targeted to a specific 'acceptor' compartment, into which they delivery their cargo upon fusion of their limiting membranes. The processes of budding and fusion are iterated across the successive cisternae until the cargo reaches the TGN, from which it departs for the PM.

In vitro studies provided striking evidence in favour of this model of intra-Golgi transport (Balch et al., 1984). In particular, it was shown that the incomplete glycosylation of VSVG in a cell line that lacks GlcNAc transferase can be rapidly restored by fusion with a wild-type cell line, suggesting the transfer of the VSVG protein between Golgi systems from different cells

(Rothman et al., 1984a). This effect was reproduced with isolated membranes from the two cell lines, which was interpreted as dissociative (i.e. vesicle-mediated) transport between independent Golgi stacks (Rothman et al., 1984b).

A key prediction of this model is that cargo proteins should be carried between Golgi cisternae within 50-60-nm peri-Golgi vesicles. However, contradictory results were reported for this aspect. *In-vitro* studies using Golgi membranes from vesicular stomatitis virus (VSV)-infected cells showed that the VSV G-protein (VSVG) entered COPI-coated vesicles (Ostermann et al., 1993). Similarly, in pancreatic cells, proinsulin was detected in a subset of vesicles, although it did not concentrate within these structures (Orci et al., 1997). In contrast, other studies reported a striking exclusion of different cargo proteins from peri-Golgi vesicles, such as albumin (Dahan et al., 1994), VSVG (Martinez-Menarguez et al., 2001; Mironov et al., 2001) and procollagen-I (PCI) (Bonfanti et al., 1998; Mironov et al., 2001).

The greatest inconsistency of the vesicular model was seen in the need to explain the transport of cargoes such as PCI (Bonfanti et al., 1998), a cargo that is too big (i.e. ~300 nm length) to fit the size of the small vesicles (i.e. ~50 nm diameter), even though a further study has proposed that such big cargoes can be transported by dissociative 'megavesicles' that would allow their rapid passage of large cargoes from the *cis*-to-*trans* cisternae of the Golgi complex (Volchuk et al., 2000) (see **Figure 1.18**).

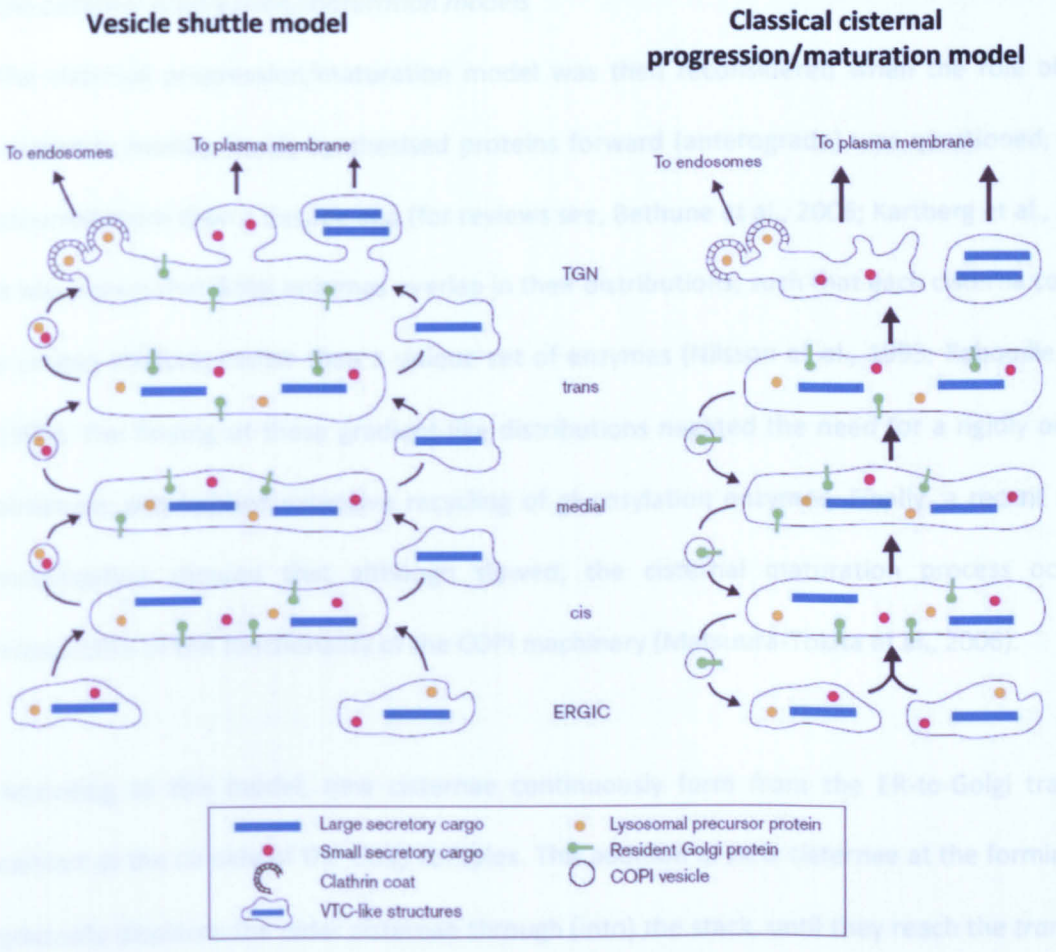

Figure 1.18. A comparison of the vesicle-shuttle and classical cisternal progression/maturation models.

Two models for anterograde transport through the Golgi complex. Thin arrows indicate transport by dissociative carriers, whereas thick arrows indicate maturation events. In the vesicle-shuttle model, ER-to-Golgi intermediate compartment (ERGIC) elements fuse with the *cis*-Golgi. Then small or 'mega' vesicles (which would be COPI vesicles and/or vesicular-tubular cluster [VTC]-like structures) bud at the Golgi rims and mediate forward transport to the next cisterna. Finally, the cargoes are sorted into either clathrin-coated vesicles or secretory carriers at the TGN level. The Golgi cisternae are considered as stable entities. In the classical cisternal maturation/progression model, ERGIC elements fuse homotypically to generate a new *cis*-cisterna, which then moves sequentially as a discrete unit through the stack towards the *trans* face, where the membranes are consumed as post-Golgi carriers, either as clathrin-coated or secretory carriers. Adapted from Glick, 2000.

The cisternal progression/maturation models

The cisternal progression/maturation model was then reconsidered when the role of COPI vesicles in moving newly synthesised proteins forward (anterograde) was questioned, which occurred more then a decade ago (for reviews see, Bethune et al., 2006; Kartberg et al., 2005). It was shown that Golgi enzymes overlap in their distributions, such that each cisterna contains a unique mixture, rather than a unique set of enzymes (Nilsson et al., 1993; Rabouille et al., 1995). The finding of these gradient-like distributions negated the need for a rigidly ordered structure, and implied extensive recycling of glycosylation enzymes. Finally, a recent *in-vivo* investigation showed that although slowed, the cisternal maturation process occurred irrespective of the functionality of the COPI machinery (Matsuura-Tokita et al., 2006).

According to this model, new cisternae continuously form from the ER-to-Golgi transport carriers at the *cis* side of the Golgi complex. This addition of new cisternae at the forming face gradually displaces the older cisternae through (into) the stack, until they reach the *trans* side, where they are consumed in the packaging of secretory cargo into post-Golgi transport carriers. Therefore, the first two key predictions of this model were that: 1) during transport through the Golgi complex, cargo proteins remain constantly within the cisterna to which they were initially delivered; and 2) new cisternae form at the *cis* pole concomitant with the consumption of mature cisternae at the *trans* pole (for review, see Elsner et al., 2003). However, over time, it became obvious that this simple model could not explain the polarity in the Golgi complex (Rabouille et al., 1995). Therefore, a counter-current of recycling vesicles was postulated that would move the Golgi-resident enzymes from the 'older' to the 'younger' cisternae (Bannykh and Balch, 1997; Bonfanti et al., 1998; Glick et al., 1997; Glick and Malhotra, 1998; Mironov et al., 1997) (see **Figure 1.18**). Thus a third feature of the model is that the Golgi-resident enzymes move retrogradely along the stack in synchrony with the formation and consumption of the cisternae. At steady-state, the rate of anterograde cisternal

progression is predicted to match the rate of retrograde vesicle transport, and the distribution of Golgi enzymes would consequently be stable. The cisternal progression model has thus been modified to the cisternal progression/maturation model, to indicate the evolving composition of the cisternae as they progress through the Golgi stack.

In spite of the studies showing a role for COPI vesicles, how the Golgi enzymes move retrogradely across the stack is still an open issue (for review, see Bethune et al., 2006). Two visible membranous structures have been proposed to mediate such enzyme transport: 1) the peri-Golgi COPI-coated vesicles (Glick and Malhotra, 1998; Storrie and Nilsson, 2002); and 2) the intercisternal tubular continuities (Trucco et al., 2004). The former is predicted in the classical version and the latter in the new version of the cisternal progression/maturation model (**Figures 1.18** and **1.19**, respectively).

As opposed to the Golgi enzymes, VSVG and PCI have not been seen to significantly diffuse across continuities between cisternae (Trucco et al., 2004). In particular, while PCI aggregates obviously cannot diffuse through these narrow tubules, the reason why VSVG should behave similarly is still not clear. One possibility is that VSVG forms clusters in the plane of the cisterna (Orci et al., 1996) that could be too large and rigid to cross the connecting tubules, thereby resulting in its progression by the maturation mechanism.

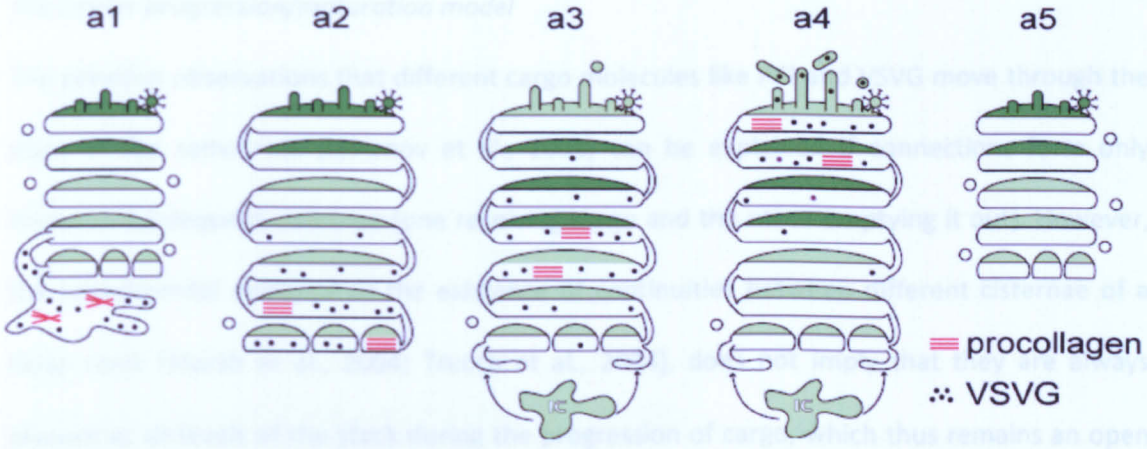

Figure 1.19. The new variant of the cisternal progression/maturation model based on continuous recycling of Golgi enzyme via tubular connections.

a1, PCI (≡) and VSVG (•) are located in the tubular-reticular IC connected with the first cisternae. IC cargo and membranes enter the stack, triggering intercisternal connections, through which the IC membranes flow into the stack. This results in the formation of new *cis* cisternae and the expansion of the old cisternae. PCI does not cross the connections and remains in the newly formed *cis* cisternae. **a2**, *Cis* cisternae continue to form by fusion between the incoming IC membranes and retrograde movement of cisternal membranes, while at the *trans*-Golgi side, membranes exit the stack in the form of tubular carriers. These two events drive the cisternal progression. At this time, the trans-Golgi enzymes (dark green) start to shift backwards from the last *trans* to the more proximal cisternae, as in **a3**, possibly as a result of the changes in their physico-chemical environment caused by the arrival of compositionally different (perhaps thicker) endosomal membranes, thus creating an enzyme-free domain ready for release. **a4**, The process continues until the cargo exits the stack via tubular carriers detaching from an enlarged TGN. **a5**, The stack returns to a quiescent state, with a reduction in cisternal number and surface area, and the disappearance of intercisternal connections. Adapted from Mironov et al., 2005.

The carrier progression/maturation model

The previous observations that different cargo molecules like PCI and VSVG move through the stack at the same rate (Mironov et al., 2001) can be explained if connections form only between subsequent cisternae (one receiving cargo and the other emptying it out). However, the experimental evidence of the existence of continuities between different cisternae of a Golgi stack (Marsh et al., 2004; Trucco et al., 2004), does not imply that they are always present at all levels of the stack during the progression of cargo, which thus remains an open issue. Therefore, the process of passage of these different cargoes might fit a carrier progression/maturation scheme, where transport carriers arriving from the ER form the so-called cargo domain within or in connection with the Golgi complex (Mironov et al., 2005; White et al., 2001) (**Figure 1.20**). This domain represents a pool of Golgi membranes derived from ER-to-Golgi carriers and enriched in cargo proteins.

This model also predicts the formation of intercisternal connections, the role of which would be to regulate the cisternal length during cargo passage through the Golgi (Mironov et al., 2005) (**Figure 1.20**). Therefore, the carrier domains and the parent Golgi elements have been proposed to be distinct regions of a continuous membrane system (White et al., 2001). In addition, the incoming carrier membrane has been suggested to redistribute through the tubules connecting successive cisternae (Mironov et al., 2005).

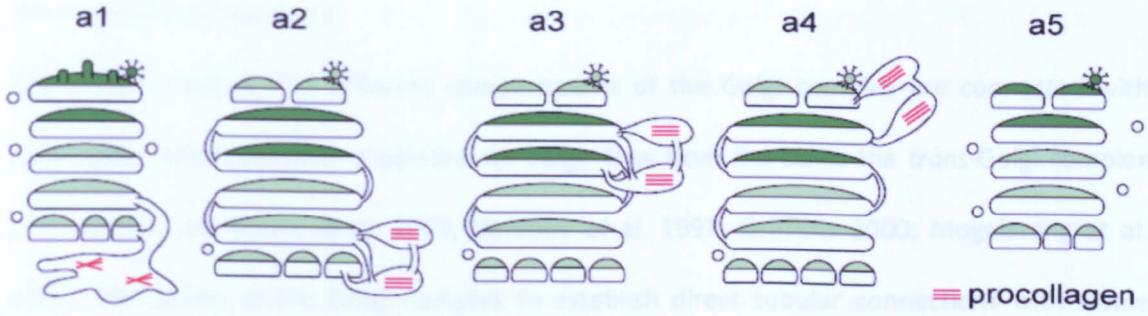

Figure 1.20. The carrier progression/maturation model.

a1, PCI (≡) is located in the tubular-reticular IC connected with the first cisternae. **a2**, IC cargo and membranes enter the stack, triggering intercisternal connections, through which the IC membranes flow into the stack, resulting in the formation of new *cis* cisternae and the expansion of the old cisternae. The carrier domain containing PCI is incorporated in the first *cis*-most cisternae. **a3**, The carrier domain containing PCI fuses with the medial cisternae of the Golgi. The excess membranes of the carrier domain redistributes between the cisternae, via intercisternal connections, leading to the maintenance of Golgi cisternae with equal length. **a4**, The fusion of the cargo domain with the *trans*-Golgi/TGN leads to the transformation of the carrier domain into post-Golgi carriers, and their departure from the Golgi complex. **a5**, The stack returns to a quiescent state. Adapted from Mironov et al., 2005.

The continuity-based model

This model predicts that different compartments of the Golgi complex are connected with each other, which provides a pipeline for cargo flow from the *cis*-to the *trans*-Golgi complex (for reviews, see Elsner et al. 2003; Mironov et al. 1997; Griffiths 2000; Mogelsvang et al. 2004). The ability of the Golgi complex to establish direct tubular connections with stable cisternae at different levels within the same stack or between adjacent stacks (**Figure 1.17B**) is the rationale for this model of transport. A role for these tubules for carrying cargo molecules was initially predicted by morphological evidence in yeast (Rambourg et al., 1993).

Moreover, the tubular connections between adjacent stacks would also be responsible for the rapid diffusion of Golgi enzymes within the intact Golgi complex of living cells (Cole et al., 1996b). However, membranous tubules linking cisternae at different levels within the same stack or between adjacent stacks have been randomly and rarely described using both SEM (Tanaka and Fukudome, 1991; Tanaka et al., 1986) and TEM (Clermont et al., 1994). Three-dimensional views of isolated *in vitro* mammalian Golgi stacks have also revealed cisternae that are apparently within the same stack and that are interconnected by peripheral tubular networks (Weidman et al., 1993).

A previous investigation (Marsh et al., 2004) showed that when pancreatic beta cells within the islets of Langerhans are stimulated to rapidly synthesise and secrete insulin, direct connections can form transiently between Golgi cisternae that normally remain distinct from one another. These authors then proposed that these connections provide a continuous lumen that facilitates the rapid transit of large amounts of newly synthesised protein for secretion, by enabling the anterograde cargo to 'bypass' interceding cisternae (Marsh et al., 2004). In a further study, the Golgi ribbon was broken down into isolated stacks of cisternae and then fully analysed by TEM tomography. Here, at steady-state it was possible to observe that up to

75% of the Golgi stacks had 13±2 intercisternal connections (Trucco et al., 2004). In contrast, these connections were not found to be positive for the presence the VSVG cargo protein (Trucco et al., 2004).

However, the possibility that small diffusible cargoes move rapidly across the Golgi stack though these tubular connections (leaving the transport of other non-diffusible cargoes explained by different mechanisms) has still to be fully explored. Previous evidence was in favour of the cooperation between maturation and diffusion (Mironov et al., 1998). Moreover, the existence of different rates of transport across the Golgi complex had also been reported previously (Lodish et al., 1983; Yeo et al., 1985). This might be explained considering the different abilities of different proteins to penetrate intercisternal connections. Thus, according to this evidence, along with the other evidence in favour of cisternal progression/maturation, a combined model for intra-Golgi transport has been proposed (Mironov et al., 2005). In particular, large cargo molecules like PCI and algal scales, which cannot enter thin tubular connections, would move across the Golgi according to a maturation scheme; in contrast, small soluble cargoes would quickly diffuse along the stack through the intercisternal connections. A third class of proteins would only partially leak through tubular continuities, thus mainly progressing across the stack in a wave-like fashion; this appears to be the case for VSVG (**Figure 1.21**). On the contrary, a recent *in-vivo* study proposed a common diffusion mechanism for all of these cargoes (Patterson et al., 2008) (see below).

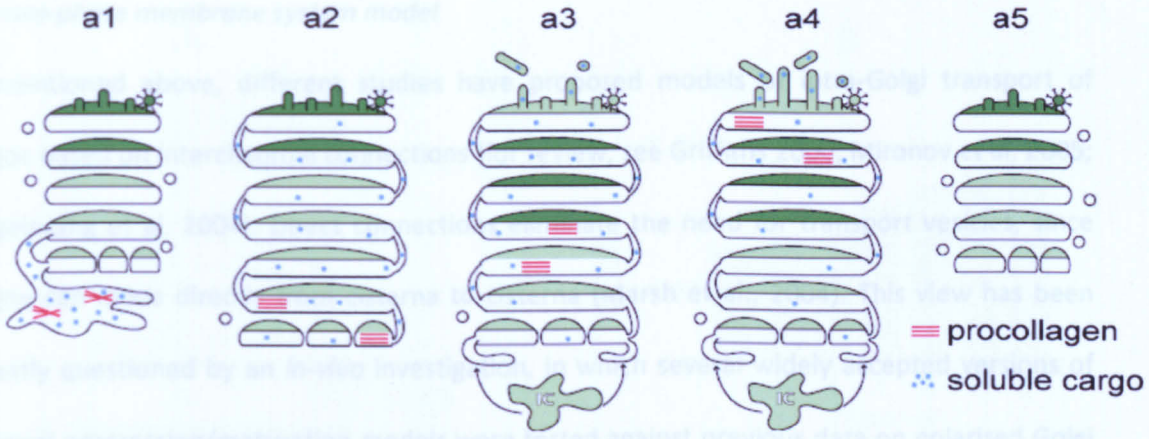

Figure 1.21. The combined diffusion-based model of intra-Golgi transport for small soluble cargoes coupled with the cisternal-maturation model, based on continuous recycling of Golgi enzymes via tubular connections, for supra-molecular aggregates.

a1, PCI (≡) and soluble cargoes (•) are located in the tubular-reticular IC connected with the first cisternae. The IC cargo and membranes enter the stack, triggering formation of the intercisternal connections through which the IC membranes flow into the stack, resulting in the formation of new *cis* cisternae and the expansion of the old cisternae. Soluble cargoes quickly diffuse along newly formed intercisternal connections and reach the trans side of the stack, while PCI remains inside the *cis*-most cisternae, as in **a2**. **a3**, Soluble cargoes are spread all over the stack and begin to exit from the TGN in saccular-tubular carriers, while PCI matures towards the medial Golgi compartment. The mechanism of PCI progression is similar to that described in **Figure 1.19**. **a4**, The exit of soluble cargoes from the Golgi continues. PCI reaches the TGN and exits the stack via tubular carriers. **a5**, The stack returns to a quiescent state, with a reduction in cisternal number and surface area, and the disappearance of intercisternal connections.

The two-phase membrane system model

As mentioned above, different studies have proposed models of intra-Golgi transport of cargoe based on intercisternal connections (for review, see Griffiths 2000; Mironov et al. 2005; Mogelsvang et al. 2004). Direct connections eliminate the need for transport vesicles, since cargoe can move directly from cisterna to cisterna (Marsh et al., 2004). This view has been recently questioned by an *in-vivo* investigation, in which several widely accepted versions of cisternal progression/maturation models were tested against previous data on polarised Golgi lipid gradients, non-uniform distribution of resident proteins, and the production of cargo waves after a temperature block (Patterson et al., 2008) (**Figure 1.22**). A new model of intra-Golgi trafficking based on partitioning of transmembrane cargo and enzymes within a two-phase membrane system has thus been proposed (Patterson et al., 2008). In this model, the stack-like organization of the Golgi complex, combined with the requirement for vesicular or tubule cargo transport across it (which prevents the system from becoming well mixed) and the partitioning of lipids between two domains, allows molecules in the system to sort spatially. Importantly, this model is characterised by mono-exponential export kinetics of a transmembrane protein (VSVG-pEYFP), a small soluble cargo (ss-pEYFP), and large insoluble aggregates (PCI-pEGFP) (Patterson et al., 2008). The existence of such spatial separation between cargoes and Golgi enzymes, in a highly dynamic system was showed by a series of simulations that resulted in a gradient in sphingolipid (SL)/glycerophospholipid (GPL) composition, with the ratio lowest in the *cis* cisterna and highest in the *trans* cisterna (see **Figure 1.22**). Resident proteins with different sphingolipid SL/GPL ratio preferences become enriched in different cisternae within the Golgi despite the processing enzymes and cargo continuously circulating both ways across the stack.

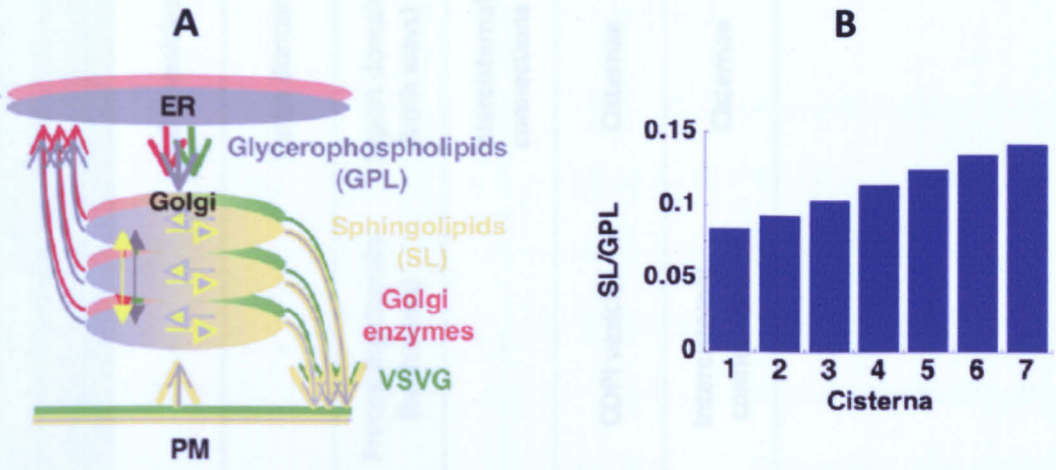

Figure 1.22. The two-phase membrane system model.

A, The lipid environment of the Golgi membrane has one component consisting of GPLs (grey) and another component consisting of cholesterol and SLs (yellow), representing the processing (grey) and export domains (yellow), respectively. Transmembrane cargo proteins move between both (processing and export) lipid environments, but concentrate in the export domain (green); in contrast, transmembrane Golgi enzymes are excluded from export domains and diffuse within the processing domain (red). Only three cisternae are shown for simplicity. **B**, Ratios of SLs and GPLs in each consecutive cisterna at steady-state according to simulations of the rapid partitioning model. Of note, there is a progressive increase in the SL/GLP from the *cis*- to the *trans*-side of the Golgi complex. Adapted from Patterson et al., 2008.

Model	Golgi Compartments	Kinetics of cargo entrance/exit	Degree of cargo-enzyme mixing	Pattern of cargo-enzyme mixing	Retrograde enzyme transport	Anterograde cargo transport
Vesicle-shuttle	Stable	Linear	Complete	Homogeneous	-	COPI vesicles
Cargo progression/maturation	Stable	Linear and then mono-exponential	Not complete	Lateral segregation of cargo	-	Cargo domain
Two-phase membrane system	Stable	Mono-exponential	Not complete	Lateral segregation of cargo	Processing domain (both ways)	Export domain (both ways)
Diffusion based on continuities	Stable	Linear	Complete	Homogeneous	-	Intercisternal connections
Classical cisternal progression/maturation	Reversible increase in volume	Linear	Complete	Homogeneous	COPI vesicles	Cisternae
New variant of cisternal progression/maturation	Reversible increase in volume	Linear	Complete	Homogeneous	Intercisternal connections	Cisternae

Table 1.4. The main comparative features of the present intra-Golgi transport models.

The models have been ordered for clarity. See text for details and references.

1.4 Statement of the problem and objective of the study

The applicability of microscopy for functional/structural studies is unquestionable. From the multitude of techniques available, fluorescence microscopy and TEM are the most commonly used. TEM provides superior resolution in the nanometre range and information on the structures surrounding those that contain the fluorescent label. However, fluorescence microscopy benefits from its use under living-cell conditions, and it is particularly useful to study processes such as intracellular trafficking. In addition, a fluorescent label provides a much clearer representation of the distribution of a protein than immunogold labelling can do, although this is partially offset by the imaging that TEM provides of membrane structures after specific staining. Therefore, in any direct comparison with TEM, the major drawback of fluorescence microscopy is its limited resolution (see **Section 1.1**). Furthermore, the determination of organelle boundaries from light microscopy images necessitates image segmentation, which is commonly achieved by applying somewhat arbitrary thresholds in a procedure that can produce unreliable structural boundaries (see **Section 1.2**).

Nowadays, super-resolution microscopy methods can make it possible to answer many previously unanswerable questions in the biological field. In more detail, methods such as 4Pi-microscopy (Hell, 1990), interference microscopy (I^5M) (Gustafsson et al., 1995), stimulated emission depletion microscopy (STED) (Hell and Wichmann, 1994), reversible saturable optical (fluorescence) transitions (RESOLFT) (Hofmann et al., 2005) sharpen the focal spot, while imaging schemes like photoactivated localisation microscopy (PALM) (Betzig et al., 2006), stochastic optical reconstruction microscopy (STORM) (Rust et al., 2006), fluorescence photoactivation localisation microscopy (FPALM) (Hess et al., 2006) and PALM with independently running acquisition (PALMIRA) (Egner et al., 2007) rely on single molecule switching and localisation. However, a spatially uneven resolution (STED) (Hell and Wichmann,

1994) or prohibitively slow image acquisition rates (PALM) (Betzig et al., 2006) are the main limitations of these techniques. An exception is provided by 4Pi-microscopy, which combines to date most of the characteristics that are needed for studying intra-cellular trafficking: it has optical sectioning and can achieves 3D resolution in the 100-nm range inside whole living cells (Egner et al., 2002), it allows the use of fluorescent proteins as markers for complex 3D structures under living conditions (Egner et al., 2004), and its imaging speed is not far from that of modern confocal microscopes.

Very recent investigations have shown the potential of 4Pi-microscopy in studying single protein complexes and the cellular nanomachinery in general (Hueve et al., 2008), and the mitochondrial network morphology relative to oxidative phosphorylation events (Plecita-Hlavata et al., 2008). However, as in these studies (Hueve et al., 2008; Plecita-Hlavata et al., 2008), fixed cells mounted in glycerol medium were used, a full exploration of the potential that this new technology can provide for living-cell imaging has not been performed. Moreover, the 3D-reconstructed structures (and the resulting morphometric analyses) were performed using a standard threshold-intensity image segmentation, which was manually adjusted with no proof as to its reliability (see also **Section 1.1.e**).

The present study asked to what extent 4Pi-microscopy can be used to at least partially bridge the gaps mentioned above, without losing the ability to work in 3D with living cells combined with an objective image segmentation procedure. To this end, adaptation of the correlative light-electron microscopy (CLEM) (Polishchuk et al., 2000) technique to 4Pi-microscopy (here referred as 4Pi-CLEM) has been set-up, thus allowing the recording of highly resolved images of individual intracellular structures by 4Pi-microscopy, and analysing exactly the same structures under TEM using 3D reconstruction procedures. Moreover, a comparison of the standard intensity thresholding, as is used routinely in fluorescence microscopy, with the

automated, intensity-independent zero-crossing segmentation procedure (O'Haver, 1979), was performed both for conventional confocal microscopy and for 4Pi-microscopy, to determine which is the more reliable for determining true organelle boundaries.

Therefore, the first 3D comparative correlative analysis of super-resolution light microscopy and TEM is presented here, as applied to protein distribution at a sub-organelle level. This has allowed the characterisation of the resolving power of 4Pi-microscopy. The results show that the combination of 4Pi-microscopy and zero-crossing image segmentation provided highly resolved and reliable imaging.

Finally, to show the applicability of 4Pi-microscopy in combination with the zero-crossing segmentation procedure, the recording of the passage of the temperature-sensitive VSVG-pEGFP protein through the *trans*-Golgi compartment (labelled with GalT-venusYFP) under living-cell conditions in a time-lapse manner was performed. The reason for applying the 4Pi-microscopy to the intra-Golgi transport study resides in the difficulties to monitor how secreted material traverses the Golgi complex by using confocal fluorescence microscopy (see **Section 1.1**) (Pawley, 2006) to ultimately uncover any superiority of the 4Pi-microscopy over conventional microscopy.

Chapter 2. Materials and Methods

2.1 Cells and growth media

2.1.a Materials

Baby hamster kidney (BHK), African green monkey (COS7) and HeLa cells were purchased from American Tissue Culture Collection (ATCC, USA). Dulbecco's modified Eagle's medium (DMEM) was from Invitrogen (UK). Foetal calf serum (FCS), penicillin, streptomycin, trypsin-EDTA and L-glutamine were from Biochrom KG (Germany). All of these reagents were purchased as 10X stock solutions. All of the plasticware for cell culture was from Corning (USA) or Falcon (USA). Filters (0.45 and 0.2 μm) were from Albet (USA).

2.1.b Growth media

BHK/COS7, HeLa cells were grown in DMEM with 4/2 mM glutamine, 10% heat-inactivated FCS, 100 U/ml penicillin, and 0.1 mg/ml streptomycin. Complete media were prepared by diluting thte concentrated stock solutions (see above) with sterile water from Diaco (Trieste, Italy) and filtering the mixture through 0.2 μm filters.

2.1.c Growth conditions

All of the cells were grown under a controlled atmosphere in the presence of 5% CO_2 at 37 °C. Maintenance of the cell lines involved growing them in a flask until 90% confluence. To detach these cells from the surface of the flask, the medium was removed and 0.25% trypsin-EDTA in normal saline solution was added, for 2-5 min at room temperature (RT). Complete medium as then added back to block the protease action of the trypsin, and the cells were collected in a plastic tube and centrifuged at 300 xg for 5 min. The cell pellet was resuspended in fresh medium and the cells were seeded in new plastic flasks.

2.2 Transformation of bacteria by heat shock and DNAs amplification

2.2.a Materials

The cPLA2ε-pEGFP, mito-pEGFP and PC3-pEGFP plasmids (see **Results, Section 3.1**) were available in our Department, while the GalT-venusYFP plasmid was a gift of Alexander Egner at the Department of Neurobiology, Max-Planck-Institute for Biophysical Chemistry (Göttingen, Germany). The pEGFP vectors were from DB Bioscience Clontech (USA). The XL-1 Blue *Escherichia coli* bacteria were purchased from Stratagene (USA). BactoTM tryptone, BactoTM yeast extract and agar were purchased from Becton, Dickinson and Company (USA). NaCl was purchased from Carlo Erba (Italy). Glycerol and Tris-HCl were purchased from Merck (Germany), and EDTA from Sigma (USA). The Qiagen plasmid kit for large-scale plasmid DNA preparation was purchased from Qiagen (USA).

2.2.b Procedure

For the transformation of the bacteria, each plasmid DNA (1 μg/μl) was diluted in 10 mM TrisHCl-EDTA to a final concentration of 50 ng/μl. One μl of the DNA (50 ng/μl) was added to 200 μl of competent bacteria that had been thawed on ice. After gentle mixing, the bacteria were incubated on ice for 20 min, heat shocked for 90 s at 42 °C, and after addition of 800 μl Luria Broth (LB), they were incubated under shaking (200 rpm) at 37 °C for 45 min. The bacteria were plated on LB-agar containing the appropriate selective antibiotic and incubated overnight (O/N) at 37 °C. The following day, an isolated bacterial colony was picked and inoculated into 2 ml of LB containing the appropriate antibiotic. The culture was incubated at 37 °C O/N, 700 μl of 50% sterile glycerol were added to 700 μl of the bacterial culture, and this was stored at –80 °C.

For the large scale preparation of plasmid DNA, a single colony of XL-1 Blue *E. coli* bacteria transformed with the plasmid of interest was inoculated into 500 ml LB plus the selective antibiotic. After a 15-20-h incubation, the bacteria were collected by centrifugation at 6,000 rpm in a JA10 rotor for 10 min at 4 °C and processed according to manufacturer instructions (Quiagen plasmid kit). The DNA obtained was resuspended in TE buffer (10 mM TrisHCl, 1 mM EDTA, pH 7.5) to a final concentration of 1 mg/ml and stored at -20 °C.

2.3 Cell electroporation

2.3.a Materials

All of the constituents of the cytomix were purchased from Sigma (USA); the only exception was for HEPES, which was purchased from Merck (Germany). The Gene Pulser II electroporator was purchased from Bio-Rad (USA). The 100-mm petri dishes were from Corning (USA); Multiwell™ (6 well) tissue culture plates were purchased from Becton Dickinson (France). Coverslips with photo-etched, numbered grids were purchased from (Bellco Biotechnology, USA); normal glass coverslips were purchased from Carlo Erba (Italy).

2.3.b Procedure

For DNA transfection, BHK, COS7 and HeLa cells were passaged into 100-mm-diameter dishes two days before transfection so as to provide a sub-confluent density on the day of transfection. The cells were then trypsinised (see above) and washed with PBS, and the pellet was resuspended in the DNA solution containing 5 μg cPLA2ε-pEGFP/mito-pEGFP (for the HeLa and BHK transfection, respectively) or 10 μg PC3-pEGFP (for the BHK transfection), and 5 μg GalT-venusYFP or a combination of 17/1 μg of VSVG-pEGFP/GalT-venusYFP (for the COS7 transfection/co-transfection), in 400 μl cytomix (120 mM KCl, 10 mM KH_2PO_4, 10 mM MgK_2HPO_4, 2 mM EGTA, 5 mM $MgCl_2$, 25 mM HEPES, 0.15 mM $CaCl_2$, 5 mM GSH, and 2 mM

ATP, pH 7.4) (Majoul et al., 2001) . The cells were immediately electroporated using a 4-mm-path cuvette in the Gene Pulser II electroporator (pulse, 0.220 kV; capacitance, 800/950 μF for the BHK/COS7, HeLa cells). Subsequently, all of the transfected BHK and HeLa cells for the correlative analyses were grown on cover slips with photo-etched, numbered grids; while, the other COS7 cells for the non-correlative analyses (localisation of the GalT-venusYFP) and for the time-lapse 4Pi-microscopy recording were grown on normal glass coverslips within the Multiwell™ tissue culture plates.

Finally, the HeLa, BHK and CO7 cells expressing cPLA2ε-pEGFP, mito-pEGFP and GalTvenusYFP, respectively, 24 h after electroporation were fixed at steady-state for immuno-TEM analysis (see **Sections 2.8.a**, **2.8.b** and **2.8.c**).

2.4 Synchronisation protocols and testing of 4Pi-microscopy recording conditions

2.4.a Materials

Dipyridyl and ascorbic acid were purchased from Sigma (USA); nocodazole and cycloheximide purchased from CalBiochem (Merck KGaA, Germany). Silicone impression material (Express) was purchased from 3M ESPE (USA). The 4Pi-microscopy cell medium (DMEM from Invitrogen [USA], plus dextran MW 39,400; 3.4% of total weight, from Sigma [USA]) (Egner et al., 2004) was gifted from Alexander Egner of the Department of NanoBiophotonics at the Max-Planck-Institute for Biophysical Chemistry (Göttingen, Germany).

2.4.b Procedure

In the BHK cells expressing PC3-pEGFP, cargo transport was synchronised by a combination of 300 μM dipyridyl, and 100 μg/ml cycloheximide and 50 μg/ml ascorbic acid treatment, in conjunction with the temperature shift, as detailed in the Results (see **Results, Section 3.3**).

For all of the experiments, these BHK cells were fixed after 1 h of PC3-pEGFP release for confocal and/or 4Pi-microscopy. The efficacy of the synchronisation protocols were checked by evaluating the degree of co-localisation of PC3-pEGFP with the Golgi marker giantin, as seen under confocal microscopy after 1 h of release (see **Results, Section 3.3**).

For the COS7 cells, those expressing GalT-venusYFP alone were fixed and labelled for immuno-TEM at steady-state 24 h after electroporation (see **Sections 2.8.a**, **2.8.b** and **2.8.c**). The other COS7 cells, co-expressing VSVG-pEGFP, were incubated after electroporation for 6 h at 37 °C, and then O/N at 40 °C, to accumulate the VSVG in the ER (White et al., 2001) (**Figure 3.24A**). Initially, the rate of VSVG-pEGFP transport through the secretory pathways was checked under the very same experimental conditions used for the 4Pi-microscopy. Nocodazole (33 μM) and cycloheximide (100 μg/μl) treatment were used in conjunction with temperature shift to synchronise VSVG-pEGFP transport, as detailed in the Results (see **Section 3.9**). As the cargo was released, the two glass coverslips were manually mounted and held together by silicone material (Egner et al., 2004). Moreover, the medium included between the coverslips was that recommended for 4Pi-microscopy, again with added cycloheximide and nocodazole (concentrations as before). The reason for using a cell medium with added dextran was to compensate for the linear phase shift induced by the residual difference between the refractive index of the water immersion liquid, used in the 4Pi-microscopy objectives, and the mounting medium itself (Egner et al., 1998) (see **Introduction, Section 1.1.e**).

Once the viability of the cells and their ability to transport the VSVG-pEGFP through the secretory pathway under the 4Pi-microscopy recording conditions was shown, the time-lapse experiments were initiated with the procedures as detailed above and in the Results (**Section 3.10**). However, due to the technical manipulation of the samples (i.e. mounting of the cover

slips), effective time-lapse 4Pi-microscopy recording started 3 to 6 min after the temperature shift.

2.5 Conventional wide-field and confocal microscopy

2.5.a Materials

The mouse monoclonal anti-giantin antibody was a gift from Dr HP Hauri (University of Basel, Basel, Switzerland). The secondary goat anti-mouse antibody conjugated with Alexa Fluor® 546 was purchased from Molecular Probes (The Netherlands). Paraformaldehyde was purchased from Electron Microscopy Sciences (EMS, USA). BSA and NH_4Cl were purchased from Sigma (USA).

Leica DM6000B wide-field and TCS SP5 confocal microscopes (Leica Microsystems CMS GmbH, Germany) were used in the correlative analyses. A Zeiss LSM 510 META confocal microscope, along with its dedicated software (LSM-510 META) (Carl Zeiss, Germany), was used for the non-correlative imaging.

2.5.b Routine fixing, blocking and staining for the visualisation of giantin

All of the samples recorded under conventional wide-field and confocal microscopy (for the correlative and non-correlative analyses) were initially fixed. The cells were fixed with 4% paraformaldehyde in 0.15 M HEPES buffer, pH 7.4, for 10 min at RT, and then washed 6 times with phosphate-buffered saline (PBS). When no immuno-labelling was performed, the coverslips were mounted with mowiol. When immuno-labelling of giantin was needed, the cells were permeabilised with blocking solution containing 50 mM NH_4Cl, 0.1% saponin, 0.5% BSA in PBS, pH 7.4, for 30 min at RT. Subsequently, the samples were incubated with the specific primary anti-giantin antibody diluted 1:400 in blocking solution, for at least 1 h at RT.

After incubation with the primary antibody, the cells were washed 6 times with PBS, to remove excess primary antibody, and then incubated with the fluorescent-probe-conjugated secondary antibody (Alexa Fluor® 546), again diluted 1:400 in blocking solution, for 1 h at RT and protected from light. The excess secondary antibody was removed by washing the samples with PBS, and then the coverslips were mounted with mowiol.

2.5.c Procedure

For the correlative wide-field microscopy, both differential interference contrast (DIC) and fluorescence pictures were taken with the 10x and 40x objectives (HC PL Fluotar 10x/0.30 and HCX PL Fluotar 40x/0.75, respectively). A GFP filter cube was used for fluorescence imaging (470/40; 500; 525/50) with a definition of 512 pixels/inch. The correlative confocal microscopy images were acquired using a 63x water-immersion objective (HCX PL APO 63x/1.20), with an excitation wavelength of 488 nm, and a pinhole size of 1 airy unit, with a definition of 1,024 pixels/inch. These correlative wide-field and confocal images were recorded in collaboration with Alexander Egner at the Department of NanoBiophotonics, Max-Planck-Institute for Biophysical Chemistry (Göttingen, Germany). All of the non-correlative confocal images were obtained using excitation at 488 nm and 543 nm (for the pEGFP/venusYFP and Alexa Fluor® 546, respectively) with the 63x oil-immersion objective, again with a definition of 1,024 pixels/inch.

Finally, for the co-transfected COS7 cells expressing both pEGFP and venusYFP, the Zeiss LSM-510 software lambda mode was used. EGFP and venus-YFP were simultaneously excited at a wavelength of 488 nm. The fluorescent light from the sample was collected in a single channel (490-550 nm) which was imaged by the camera. As these fluorescent proteins exhibit strong overlap of their emission spectra, we used the linear un-mixing function of the Zeiss LSM-510

software to separate the individual signals, using 505 nm and 520 nm as the emission peaks for EGFP and venusYFP, respectively.

The files were exported as lif and lsm formats, for the Leica and Zeiss microscopes recordings respectively.

2.6 4Pi-Microscopy

2.6.a Materials

A two-photon type A 4Pi-microscopy prototype (Egner et al., 2002) developed at the Max-Planck-Institute for Biophysical Chemistry (Göttingen, Germany) and set as reported in **Introduction, Section 1.1.e**, was used. The mode-locked Ti-sapphire laser was purchased from Mai Tai, Spectra Physics (Germany). All of the lenses, including the water-immersion focusing lenses with a α angle of ~65°, were purchased from Leica Microsystems CMS GmbH.

2.6.b Procedure

The head of the 4Pi-microscopy included the beam-splitter and the objective lenses that were illuminated through the balanced interferometric arms (see also **Introduction, Section 1.1.e**). Axial scanning was performed by moving the sample along the optic Z-axis. The beam of the Ti-sapphire laser was split by an array of microlenses, producing the array of beamlets (4Pi foci) that, after passing through a dichroic mirror, were focused onto an array of pinholes. The pinholes acted as point sources for creating the 4Pi illumination spots in the sample. After passing the pinholes, each beamlet was collimated by an achromatic lens and directed towards a rapidly oscillating galvanometric mirror. The rapid tilt of the mirror results in lateral scanning of the illumination 4Pi foci along the X-axis. Scanning of the beamlets in the *Y-axis was* accomplished by translating the combined microlens and pinhole array. The fluorescence was

collected by the objective lens on the left-hand side and deflected by a galvanometric mirror in order to be back-imaged onto the pinhole array. The diameter of the pinholes corresponded to 1.25-fold the diameter of the back-projected Airy disk (i.e. the diameter of the first dark ring). This slight confocalisation allowed the suppression of the axial side lobes and also reduced the residual aberrations stemming from the microlenses (see also **Table 1.1**). After having been filtered by the pinholes, the fluorescence light was reflected by the long-pass dichroic mirror towards the reflective backside of the galvanometric mirror. The tilt movement of such galvanometric mirror scanned the array of fluorescence beamlets across a CCD camera (Egner et al., 2002). Moreover, two-photon excitation of EGFP was performed at a wavelength of 890 nm (1.5 mW) and an array of 20 4Pi foci, separated from each other by ~ 2.8 µm, were used. Other general setting information are reported in **Introduction, Section 1.1.e**. The linear phase shift induced by the residual difference between the refractive indices of the water immersion liquid and the mounting medium was actively compensated for (Egner et al., 1998) (see **Section 2.4.b**). Typical stacks comprised 100-nm XY-images that were axially separated by 80 nm and scanned at a rate of 2 s per XY-slice

For two-colour 4Pi-microscopy, EGFP and venus-YFP were simultaneously excited at a wavelength of 890 nm. The fluorescent light from the sample was split into two channels (475-525 nm and 525-600 nm), which were both imaged onto the same chip of the CCD-camera. As these fluorescent proteins have a strong overlap of their emission spectra, we used linear un-mixing (Zimmermann et al., 2003) to separate the individual signals.

The files were exported as spe format.

2.6.c Three-point deconvolution

In 4Pi-microscopy, illumination by two opposing objective lenses produces a PSF that is comprises a sharp central maximum flanked in the beam directions by the lower side lobes (see **Introduction, Section 1.1.e**, and **Figure 1.6**) (Hell and Stelzer, 1992a). To remove these side lobes in the correlative part of this work, the raw 4Pi-microscopy data were deconvolved with a three-point linear filter (Hänninen et al., 1995). Because the time-lapse experiments were carried out at a lower SNR, 3D recordings were deconvolved by a Richardson-Lucy algorithm (Richardson, 1972). This allowed the recording of up to nine consecutive time points. The three-point deconvolved data were finally stored as msr format.

The three-point deconvolutions illustrated throughout the present study were mostly performed by Tobias Müller, using the ImSpector software developed by Andreas Schönle, both from the Department of NanoBiophotonics, Max-Planck-Institute for Biophysical Chemistry (Göttingen, Germany).

2.7 Three-dimensional reconstructions from confocal and 4Pi-microscopy data

2.7.a Software

The Zeiss LSM-510 software (Zeiss, Germany), the MATLAB (MATLAB, R2006b) coupled with the DIPImage software (version 1.6, http://www.diplib.org/), and the Visual Molecular Dynamics (VMD) packages (version 1.8.5, http://www.ks.uiuc.edu/Research/vmd/) (Humphrey et al., 1996) were used.

2.7.b Procedure

To visualise the endosomal, mitochondrial and Golgi stack structures after the confocal microscopy recordings, all of the files were first converted into dbl format by ImSpector

software. Subsequently, through a dedicated MATLAB routine, the DIPimage software was used to develop the 3D reconstructions into dx format. Specifically, MATLAB is a software package designed for (among other things) data processing for working on large amounts of numerical algorithms, and DIPimage is a MATLAB toolbox used for scientific image processing and analysis. The same was done for the three-point deconvolved 4Pi-microscopy data. This dx format is then readable in the VMD package, which was used to visualise the 3D reconstructions (including those merging the 4Pi-microscopy and TEM data; see below). VMD is a molecular visualisation programme for analysing, displaying and animating large bimolecular systems using 3D graphics; in the present study, it was adapted for the rendering of the intracellular compartments.

After smoothing the 3D data sets with a Gaussian filter (with a σ value set at 2), the threshold-intensity and zero-crossing procedures were implemented in MATLAB and used for the 3D reconstruction of the Golgi stacks. For the standard threshold-intensity procedure, dx files with the entries identical to those of the 4Pi-microscopy recordings were loaded into VMD and the appropriate intensity threshold was set for the 3D reconstruction. For all of the zero-crossing-based procedures of the time-lapse experiments, the background pixels below 20% of the maximum PSF intensity (Young et al., 1995) were cut before calculating the zero-crossing algorithm (O'Haver, 1979) (see **Results, Sections 3.3** and **3.7**).

The dedicated MATLAB routine was written by Alexander Spaar from the Department of Cell Biology and Oncology, Consorzio Mario Negri Sud (Santa Maria Imbaro [CH], Italy).

2.8 Transmission electron microscopy

2.8.a Materials

The primary rabbit polyclonal anti-EGFP antibody was from Abcam (UK); the Fab fragments conjugated with nanogold (1.4 nm gold particles) were purchased from Nanoprobes (USA). GoldEnhance™-EM was purchased from Nanoprobes (USA). Osmium tetraoxide, paraformaldehyde and glutaraldehyde were purchased from Electron Microscopy Sciences (USA). Sodium cacodylate, and the Epoxy resin kit (Epon-812, Epoxy Embedding Medium Kit) were purchased from Sigma (USA). Potassium ferrocyanide, ethanol and acetone were purchased from Carlo Erba (Italy). The stereomicroscope and ultra-microtome were purchased from Leica Microsystems CMS GmbH (Germany). The diamond knife was purchased from Diatome (Switzerland). The metal loop (Perfect Loop) was purchased from Agar Scientific Ltd (UK), and the slot grids covered with carbon-formvar supporting film were purchased from Electron Microscopy Science (EMS, USA). A Philips Tecnai-12 electron microscope (Philips, Eindhoven, The Netherlands) was used to acquire the TEM images.

2.8.b Routine fixation, blocking and immuno-TEM labelling of the EGFP/venusYFP

The samples used to localise the GalT-venusYFP chimera within the Golgi complex were fixed 24 h after electroporation, at steady-state with 0.05% glutaraldehyde in 0.15 M HEPES for 10 min at RT. Afterwards, the cells were washed 6 times in PBS at RT and incubated with blocking solution for 30 min at RT. Finally, the cells were incubated with the primary antibody sensitive to the EGFP tag, which also labelled the venusYFP tag, diluted 1:500 in blocking solution and left O/N at 4 °C, as previously described (Ladinsky et al., 1999).

For the other samples used in the correlative analyses (expressing cPLA2ε-pEGFP or mito-pEGFP/PC3-pEGFP), immediately after the confocal/4Pi-microscopy recordings, they were

further fixed and incubated with blocking solution as above. These cells were also incubated with the same primary antibody sensitive to the EGFP tag (see above) as for the labelling of venusYFP.

2.8.c Nanogold labelling

This procedure is among the pre-embedding techniques based on the concept that labelling is performed before sample embedding. Briefly, the samples were chemically fixed and the antigen was labelled using a specific primary antibody that was recognised by a secondary antibody conjugated with ultra-small gold particles. The detection of the gold particles was almost unequivocal, and they could be exactly quantised; however, one limitation of the use of colloidal gold conjugates (5, 10, and 15 nm gold particles) was that they generally do not penetrate cells, even after permeabilisation. Therefore, their use in pre-embedding immuno-staining has up to now been restricted, both for the labelling of cell-surface antigens, and for tracing the endocytic pathways in living cells. Recently, 1.4 nm gold conjugates that penetrate cells and tissues much more readily have been used successfully to immuno-label intracellular structures. Ultra-small immuno-gold probes label more efficiently than do the larger colloidal gold particles (1.4> 5> 10> 15 nm). The only drawback of this approach is that to detect 1.4 nm gold probes by conventional TEM, the gold enhancement reaction had to be developed, and this procedure typically produces particles of variable diameters, unlike the 5, 10, and 15 nm particles that instead are uniform in diameter. Another advantage of this approach is the possibility of cutting serial consecutive sections of the specimen, which were used for the 3D reconstruction of organelles (see **Section 2.9b**).

Nanogold labelling was then performed and developed using the GoldEnhance^{TM}-EM protocol. Specifically, on the following day to the incubation with the primary antibody, the samples were washed 6 times with PBS at RT and incubated with goat anti-rabbit or anti-mouse Fab

fragments coupled to 1.4 nm gold particles (diluted in blocking solution 1:100) for 2 h, protected from light, and finally washed 6 times with PBS at RT. Meanwhile, the activated Goldenhance™-EM reaction mixture was prepared according to the manufacturer instructions, and 100 µl was added to each well. The reaction was monitored by a conventional light microscope at RT for 5-10 min while the cells acquired a typical 'dark' colour (due to gold particles deposition), and then stopped by washing 6 times with PBS. At this stage, in the non-correlative samples, the cells were gently detached using a manual scraper, collected in an Eppendorf tube by micropipette, and centrifuged at 13,400x *g* for 5 min at RT prior to the following procedures.

2.8.d Osmium post-fixation and embedding

Osmification followed immediately after nanogold labelling. The samples were washed 3 times with distilled water and then incubated for 1 h at RT in a 1:1 mixture of 2% osmium tetraoxide in distilled water and 3% potassium ferrocyanide in 0.2 M sodium cacodylate pH 7.4, and then washed 6 times with distilled water. The samples were then dehydrated: 3x 10 min in 50% ethanol; 3x 10 min in 70% ethanol; 3x 10 min in 90% ethanol; 3x 10 min in 100% ethanol. The samples were subsequently incubated for 2 h in a 1:1 mixture of 100% ethanol and Epoxy resin at RT; the mixture was then removed with a pipette and finally the samples were embedded for 2 h in Epoxy resin at RT. The resin was polymerised for at least 10 h at 60 °C in an oven.

2.8.e Ultrathin sectioning of the samples and TEM recording

After resin polymerisation, with the non-correlative samples as cells collected in a pellet, they were directly trimmed into a small pyramid matching the dimensions of the carbon-formvar supporting film. In contrast, for in the correlative samples, the coverslips were dissolved in 40% hydrofluoric acid. The cells of interest were then identified again under the stereomicroscope, using the negative imprint of the reference grid on the surface of the

embedded sample and the relative positions of the surrounding cells. Subsequently, these samples were trimmed to obtain a small pyramid with the cell of interest in the centre. For all of the samples, sections of 80-nm thickness were obtained by using an ultra-microtome with the diamond knife. Subsequently the sections were collected with the Perfect Loop, placed on slot grids covered with carbon-formvar supporting film, and without additional staining, they were observed by TEM equipped with an ultra-view CCD digital camera. In particular, under 120 kV, different magnifications (from 600x to 60,000x) were used to capture the images of the cells and their corresponding intracellular structures.

2.9 Morphometric analysis and 3D reconstructions from TEM data

2.9.a Software

The analySIS software (Soft Imaging Software Corporation, USA), the PhotoPaint software (version 8, Corel Corporation, Canada), and the Imod software (version 3.9.3, http://bio3d.colorado.edu/imod/) were used.

2.9.b Procedure

The analySIS software was used in the non-correlative analyses to evaluate the morphology of the Golgi complex after nocodazole treatment, and the localisation of the GalT-venusYFP chimera. However, since the morphology of the Golgi stacks and the localisation of the GalT-venusYFP yielded unequivocal results (see **Results, Sections 3.9**), neither quantitative analyses nor 3D reconstructions were performed.

For the correlative analyses, the serial TEM images were handled using the PhotoPaint software. To accurately align the images, a first alignment with lower resolution images was performed. This was used to initially understand the architecture of the structures of interest

and to have several other intracellular organelles/compartments structures on the same images, to use them in the alignment. Subsequently, a second alignment, using high-resolution images, was performed on the basis of the first one.

Once the high resolution serial images had been aligned, subsequent 3D reconstructions were performed using the Imod software. The boundaries of the endosomal/mitochondrial or Golgi stacks (including cisternae and carriers, as defined in the Results [**Section 3.6**]), were traced on Imod software according to the immuno-labelling. Subsequently, 3D reconstructions were directly performed on the same Imod software, while for the overlapped 3D analyses (see **Section 2.10**), each serial image containing the tracing of the boundaries was exported as TIFF format.

2.10 Three-dimensional overlap of the 4Pi-TEM reconstructions

2.10.a Procedure

After the manual tracing of the boundary membranes of the compartments positive for cPLAε-pEGFP, mito-pEGFP or PC3-pEGFP in the serial TEM recordings, the corresponding images (as TIFF files) carrying only the traced contours on a white background, were loaded into VMD through the MATLAB routine. Finally, the 3D overlaps between the confocal/4Pi-microscopy and the TEM reconstructions were performed within the VMD software. A manual alignment of the 4Pi-microscopy and TEM reconstructed structures was performed by only shifting and rotating the structures along the three axes, without any rescaling, using a dedicated MATLAB routine written by Alexander Spaar from the Department of Cell Biology and Oncology, Consorzio Mario Negri Sud (Santa Maria Imbaro [CH], Italy).

2.10.b Manders coefficients

The calculation of the overlap coefficient is another method to characterise the degree of overlap between the two channels in a microscopy image. This parameter is not sensitive to differences in signal intensities between the two channels, photo-bleaching or amplifier settings, and its values range from 0 (no co-localisation) to 1 (all pixels co-localised). However, a consequence of the symmetry of the way both channels contribute to the overlap coefficient is that it cannot distinguish between situations when a not-co-localised signal is added to channel 1 *versus* channel 2. To cancel out this effect, the overlap coefficient can be split into two different coefficients, the so-called Manders coefficients (Manders et al., 1993). Briefly, k1 represents the percentage of co-localised volume with respect to the volume of the TEM reconstruction, and k2 that with respect to the 4Pi-microscopy reconstruction:

$$k_1 = \frac{\sum(R_i G_i)}{\sum R_i^2} \quad \text{and} \quad k_2 = \frac{\sum(R_i G_i)}{\sum G_i^2}$$

where Ri represented the value of the voxel i of the TEM reconstruction, and Gi the voxel i of the 4Pi-microscopy reconstruction (after normalisation of both image stacks). Using the standard threshold-intensity procedure, the volume of the 4Pi-microscopy data reconstruction, and thus k1 and k2, depend directly on the choice of threshold value. At the best values, k1 and k2 are equal (see **Figure 3.17**). Before calculating the Manders coefficients, however, the membrane outlines obtained by TEM recording of serial sections had to be transformed into a true three-dimensional object. For this, the serial sections of a Golgi stack recording were aligned, its outlines were filled homogenously, and each 2D image was assigned a width of 80 nm, in accordance to the width of the sections after cutting. To make it comparable to the 4Pi-microscopy recordings, the resulting structure was convolved with a simulated effective 4Pi-microscopy PSF. The full width at half maximum of this PSF was set as equal to that measured

in the recordings of GS1 and GS2, respectively, after side lobe removal. The calculations of the Manders coefficients were performed using a dedicated MATLAB routine (MATLAB, R2006b), written by Jan Keller at the Max-Planck-Institute for Biophysical Chemistry (Göttingen, Germany).

2.11 Quantitative analyses in time-lapse 4Pi-microscopy

2.11.a Centres of gravity of the fluorescent signals

In the time-lapse experiments, the consecutive recordings of one series were aligned to the first recording with respect to the centre of gravity of the red channel (GalT), after thresholding and applying the zero-crossing procedure. Here, the centre of gravity is defined as:

$x_{CG} = \left(\sum x_i I(x_i)\right) / I_{tot}$, where I_{tot} is the total intensity $I_{tot} = \sum I(x_i)$.

Moreover, the distance between the centres of gravity of the two channels (EGFP and venusYFP) was also recorded at each time point. The calculations of the centres of gravity were performed using a dedicated MATLAB routine, written by Alexander Spaar from the Department of Cell Biology and Oncology, Consorzio Mario Negri Sud (Santa Maria Imbaro [CH], Italy).

2.11.b Weighted/non-weighted co-localisation

Weighted and non-weighted co-localisations were calculated as is usual. First, a threshold has to be set and only those voxels with an intensity above this threshold for each channel are taken into account. These voxels are subdivided into three regions: region 1 is defined as the sum of all of the voxels where the intensity of only channel 1 is above the threshold, and

region 2 is defined the same way for voxels of channel 2. All of the voxels where both channels have an intensity higher than the threshold belong to region 3. For the non-weighted co-localisation, the ratio between the number of pixels in region 3 to the number of voxels in region 1 or 2, respectively, is calculated. For the weighted co-localisation, the ratio is not calculated between the numbers of voxels, but between the intensities of the corresponding voxels. The calculation of the weighted/non-weighted co-localisation were performed using a dedicated MATLAB routine written by Alexander Spaar from the Department of Cell Biology and Oncology, Consorzio Mario Negri Sud (Santa Maria Imbaro [CH], Italy).

Chapter 3. Results

3.1 Validation of the zero-crossing procedure by CLEM

To test the reliability of the zero-crossing procedure and the effects of the different thresholding before its application, a CLEM analysis was performed using two different intracellular structures. The workflow of the CLEM technique is shown in **Figure 3.1** (in which the 4Pi-microscopy recording performed in the following experiments is also shown). In a first analysis, a recently identified ε isoform of the cytosolic phospholipases A_2 ($cPLA_2\varepsilon$) tagged with the pEGFP vector (Ohto et al., 2005) and mito-pEGFP (Pistor et al., 1994) were expressed in HeLa and BHK cells, respectively.

According to unpublished observations carried out by Maria Grazia Capestrano from our Department, $cPLA_2\varepsilon$ resides in a highly dynamic tubular-vesicular compartment, where thick tubules reach lengths of up to 15-20 μm. These resemble a subset of the early and recycling endocytic compartments. Mito-pEGFP was generated by cloning the cDNA of the membrane anchor of the *Listeria monocytogenes* surface protein ActA (Pistor et al., 1994) into a pEGFP vector, similarly to that reported by Grubinger and Gimona (Grubinger and Gimona, 2004). When expressed in eukariotic cells, the membrane anchor of ActA shows a selective affinity for the mitochondrial membrane, so that it can be used to target a fusion protein to the mitochondria. The structures labelled by the cPLA2ε-pEGFP and mito-pEGFP should thus be within the resolution limit of confocal microscopy, providing an ideal target for this comparative analysis of the 3D reconstructions obtained by the parallel recording under confocal microscopy and TEM.

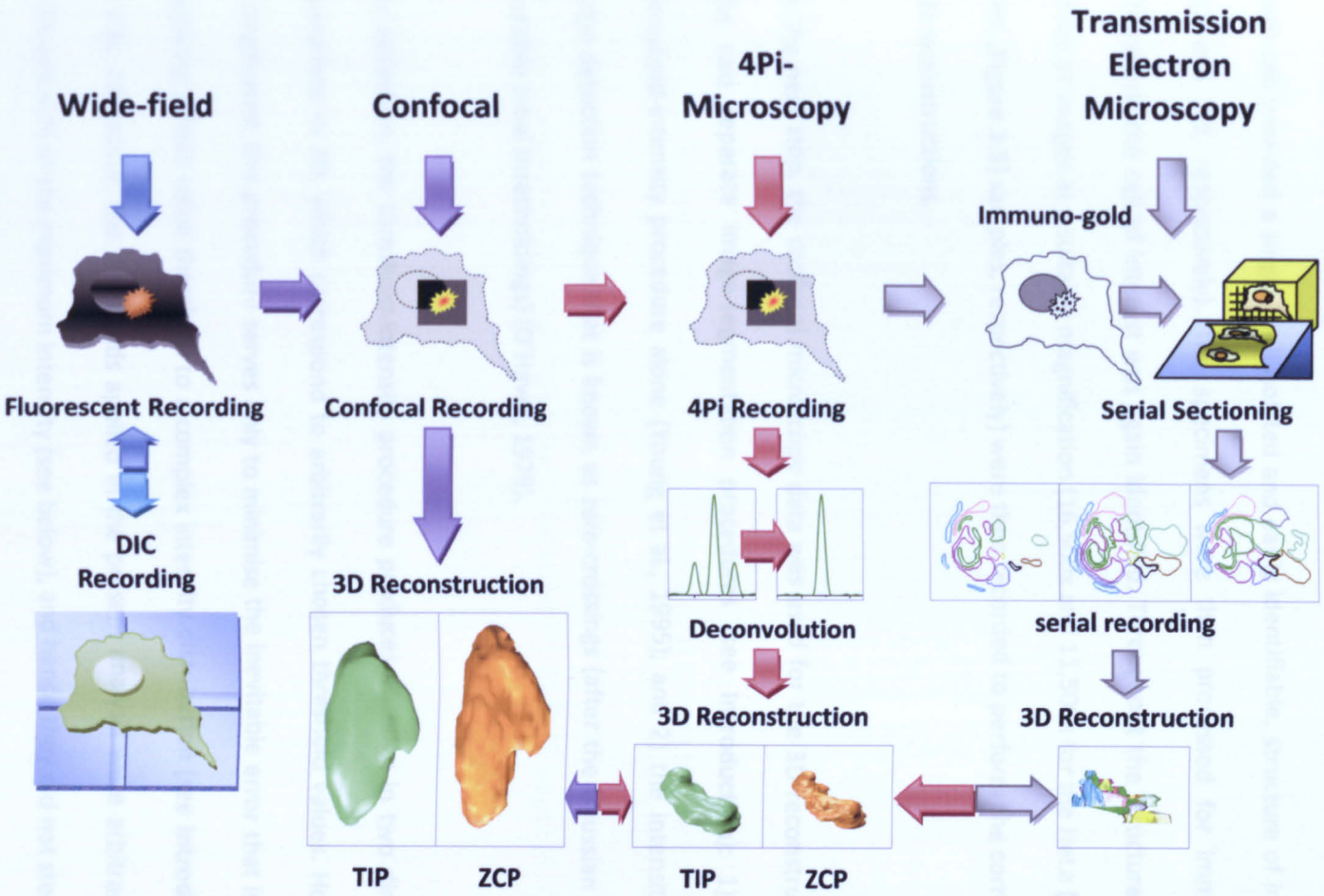

Figure 3.1. Diagram of the 4Pi-CLEM technique.
DIC, Differential interference contrast; **TIP**, Threshold-intensity procedure; **ZCP**, Zero-crossing procedure. See text for details.

The cells were transfected and fixed after 24 h at steady-state, with no additional treatments. Under confocal microscopy, once a cell that showed clearly identifiable endosomal/mitochondrial structures was identified, a 3D sequence of the structures of interest was acquired (see **Figure 3.1**). A HeLa and a BHK cell, were chosen for the analysis, and each cell provided a single, well isolated and easily identifiable, structure of interest (**Figures 3.2** and **3.3**, respectively). The specimens were then processed for immuno-TEM, and afterwards the cell of interest was again identified. Throughout the structures of interest, a series of images at a suitable magnification (16,500x and 11,500x for the HeLa [**Figure 3.4**] and BHK [**Figure 3.5**] samples, respectively) were then recorded to perform the corresponding TEM 3D reconstructions.

In the next step, the confocal microscopy data was used for the 3D reconstruction following the two separate image-segmentation procedures (see **Introduction**): 1) the standard threshold-intensity procedure alone (Young et al., 1995); and 2) the intensity-independent, edge-detection technique that is known as zero-crossings (after the Gaussian smoothing and variable intial thresholdings) (O'Haver, 1979).

By definition, the threshold-intensity procedure produces an edge in two dimensions or an isosurface in 3D, which correspond to arbitrarily chosen threshold values. However, even if complicated, this procedure serves only to minimise the inevitable error that is introduced by applying a fixed value threshold to a complex intensity distribution (see **Introduction, Section 1.2.b**). Moreover, the thresholds applied in the present analysis were arbitrarily set as 20%, 30% and 40% of the maximum intensity (see below), and hence they did not stem directly from any structural consideration from the light microscopy. Therefore, the zero-crossing procedure was applied to provide a further reconstruction of the confocal microscopy data of the structures of interest (O'Haver, 1979; Young et al., 1995).

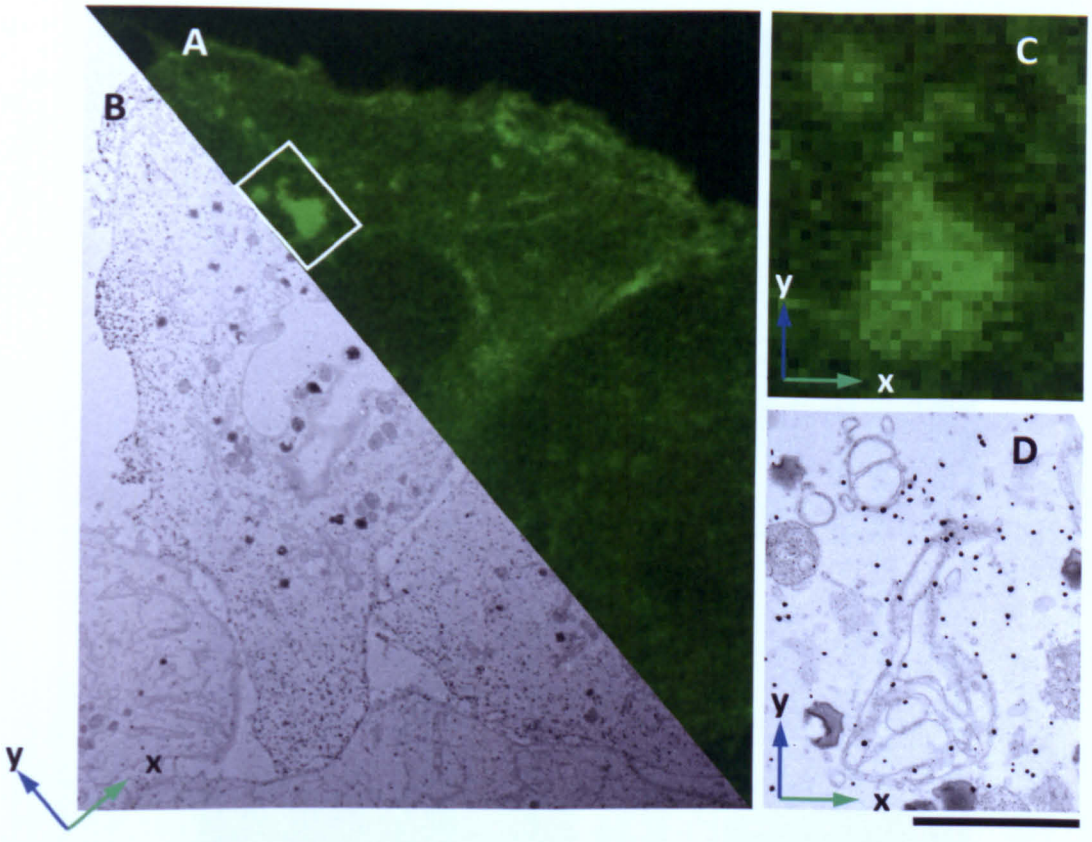

Figure 3.2. Overview of the cell, with the identification of the endosomal structures.
A, Confocal fluorescent microscopy recording of the cell including the endosomal structures. **B**, Low magnification TEM recording. The white box in **A** represents the views of the mitochondrial structures detailed in **C** (confocal) and **D** (TEM). Bars, 10 µm (A, B); 1 µm (C, D).

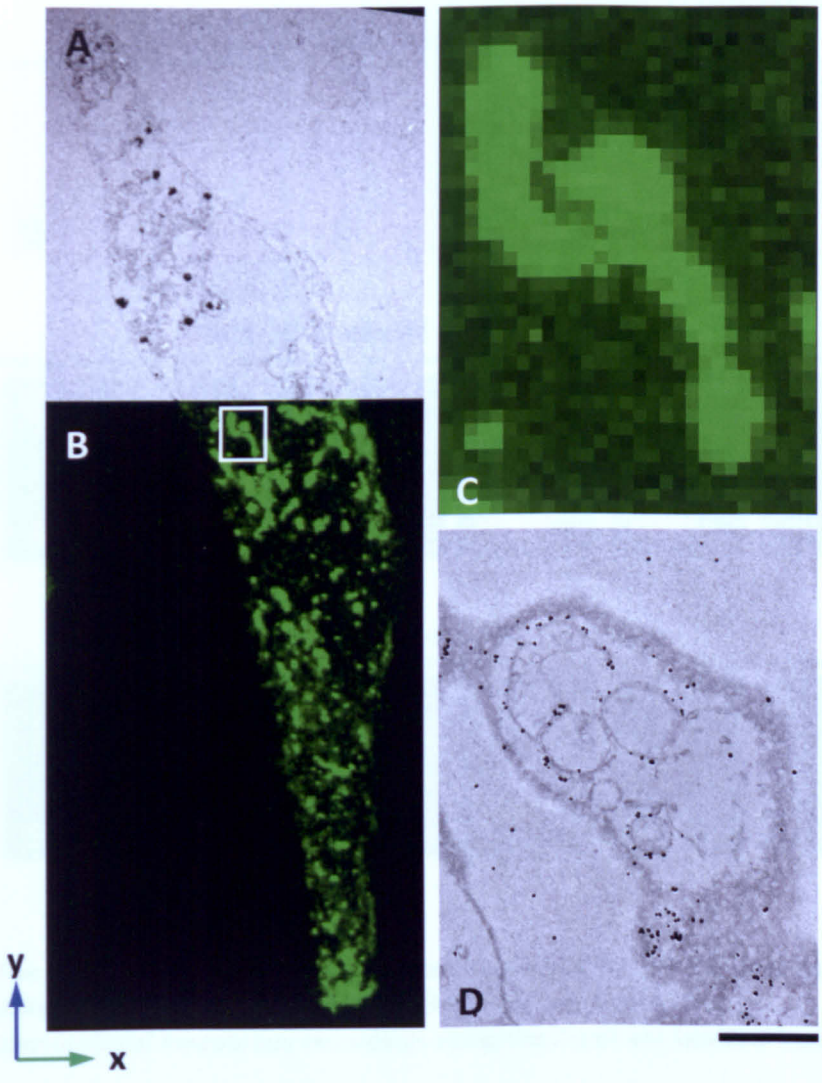

Figure 3.3. Overview of the cell, with the identification of the mitochondrial structures.
A, Low magnification TEM recording; **B**, Confocal fluorescent microscopy recording of the cell including the mitochondrial structures. The white box in **B** represents the view of the mitochondrial structures detailed in **C** (confocal) and **D** (TEM). Bars, 10 µm (A, B); 1 µm (C); 1.2 µm (D).

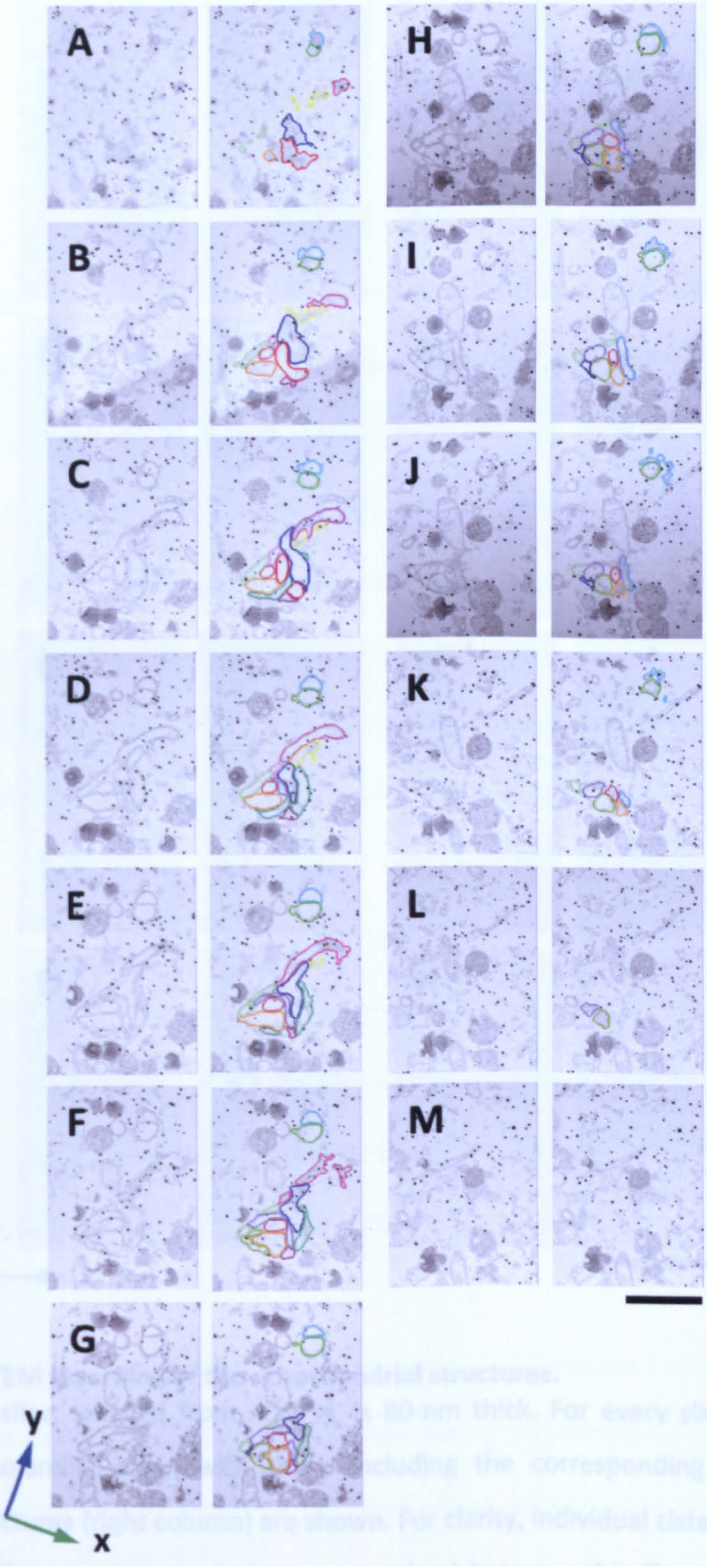

Figure 3.4. Serial TEM recording of the endosomal structures.
Each consecutive slice, labelled from **A** to **M**, is 80-nm thick. For every slice, the raw TEM recordings (left columns) along with those including the corresponding outlines of the reconstructed structures (right column) are shown. For clarity, individual cisternae and carriers are outlined in different colours, which are maintained between this **Figure** and **Figures 3.5 and 3.7**. Bar, 2 μm.

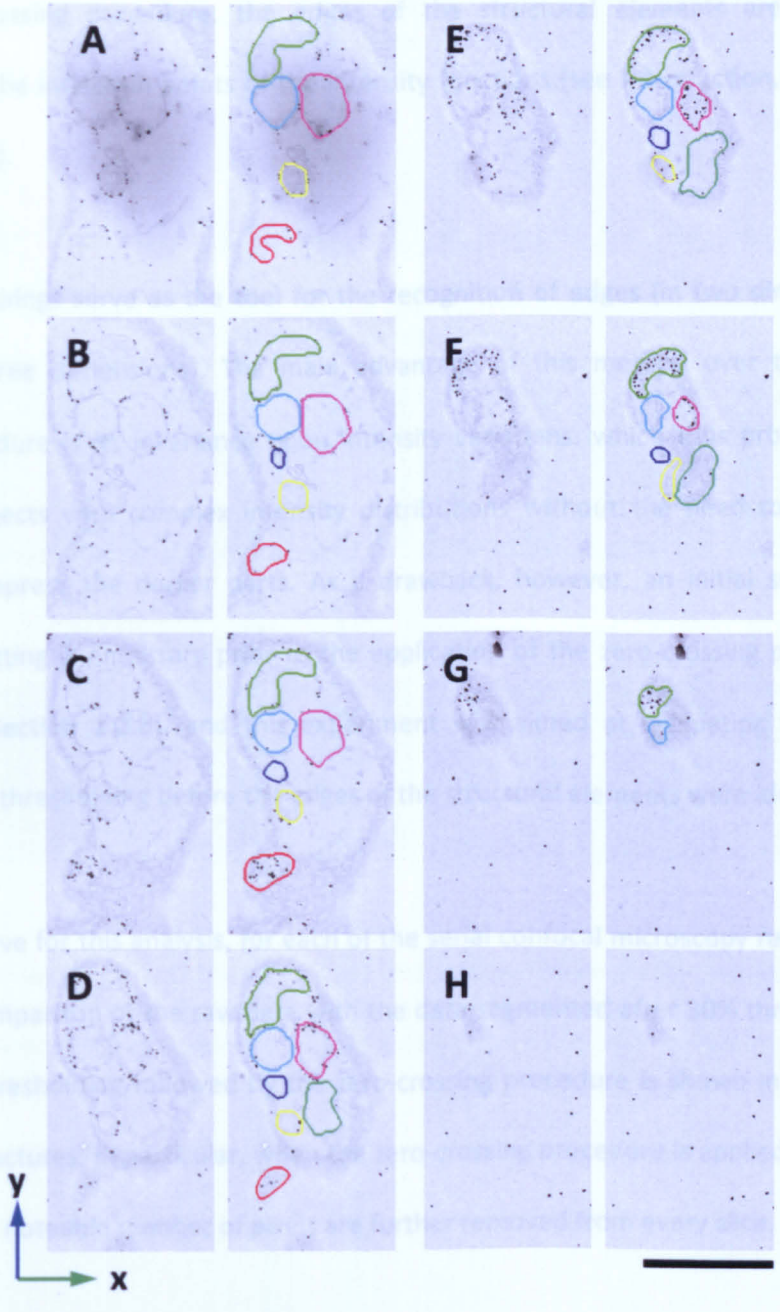

Figure 3.5. Serial TEM recording of the mitochondrial structures.
Each consecutive slice, labelled from **A** to **H**, is 80-nm thick. For every slice, the raw TEM recordings (left columns) along with those including the corresponding outlines of the reconstructed structures (right column) are shown. For clarity, individual cisternae and carriers are outlined in different colours, which are maintained between this **Figure** and **Figure 3.8**. Bar, 2 µm.

In this zero-crossing procedure, the edges of the structural elements are assumed to correspond to the inflection points of the intensity functions (see **Introduction, Section 1.2.b** and **Figure 1.11**).

These zero-crossings serve as the tool for the recognition of edges (in two dimensions) and surfaces (in three dimensions). The main advantage of this method over the threshold-intensity procedure is its invariance upon intensity variations, which thus produces reliable surfaces of objects with complex intensity distributions without the need to enhance the brighter or suppress the darker parts. As a drawback, however, an initial smoothing and background cutting is necessary prior to the application of the zero-crossing procedure (see **Introduction, Section 1.2.b**), and this experiment was aimed at evaluating the effects of different initial thresholding before the edges of the structural elements were identified.

As representative for this analysis, for each of the serial confocal microscopy recordings along the Z-axis a comparison of the raw data with the data segmented after 30% thresholding, and for the 30% thresholding followed by the zero-crossing procedure is shown in **Figure 3.6** for endosomal structures. In particular, when the zero-crossing procedure is applied after the 30% thresholding, a noteable number of pixels are further removed from every slice.

Subsequently, all of the reconstructions from the confocal microscopy (both by the threshold-intensity procedure only, and followed by the zero-crossing segmentation) and TEM recordings were overlapped in 3D to determine the reliability of the zero-crossing procedure for image segmentation (**Figures 3.7** and **3.8** for endosomal and mitochondrial structures, respectively). This was accomplished using the VMD software in which the TEM data were correctly interfaced using a dedicated MATLAB routine (see **Materials and Methods, Section 2.10**).

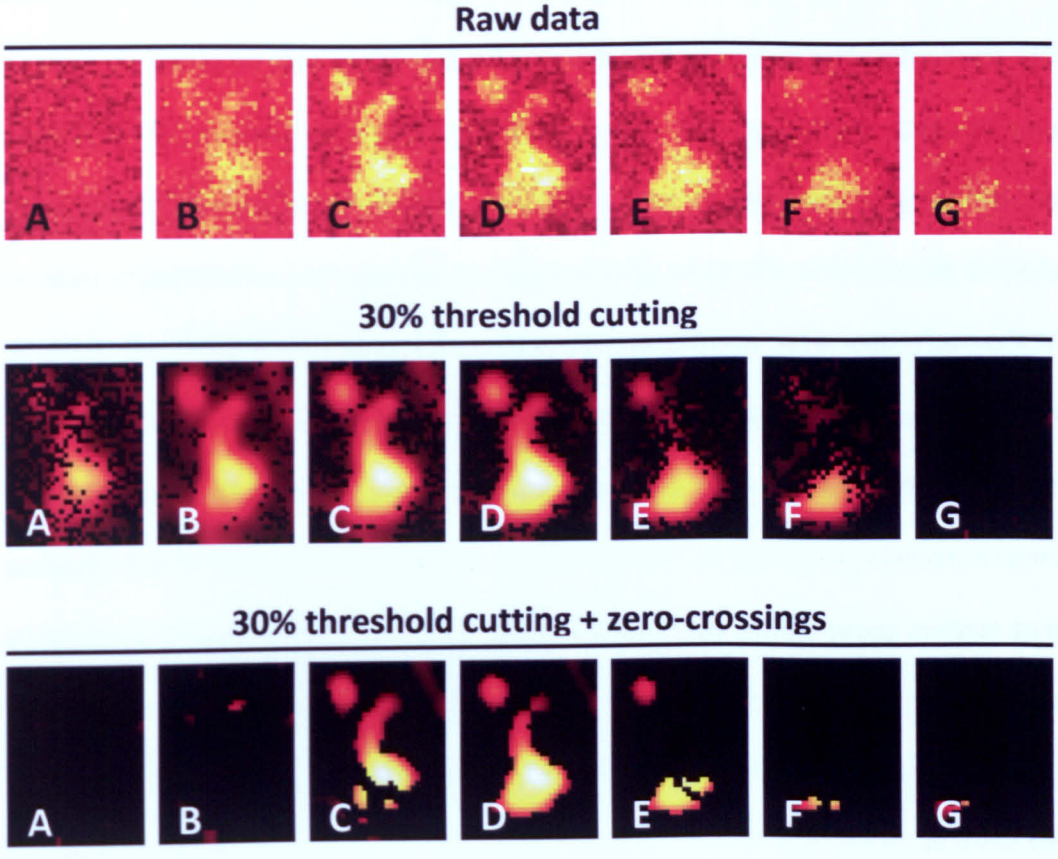

Figure 3.6. The raw data and the corresponding segmentation by the standard threshold-intensity and the zero-crossing procedures for the endosomal structures.
The consecutive confocal microscopy recordings along the Z-axis are labelled from **A** to **G**.

Here, similar results were obtained for the endosomal and mitochondrial structures of interest. As shown in **Figures 3.7** and **3.8**, at each of the initial thresholding levels (20%, 30% and 40% of the maximum intensity), the fitting is poor when the zero-crossing procedure was not applied (**Figures 3.7/3.8A-F, M-R**). Even using higher thresholding of up to 70%, the fitting remains unsatisfactory (not shown). On the contrary, when the zero-crossing procedure was added to the initial thresholding, strikingly better correlations were seen (**Figures 3.7/3.8G-L, S-X**). Of note, the different initial thresholding did not significantly preclude the reliability of the corresponding zero-crossing procedure outcomes (**Figures 3.7/3.8G-L, S-X**). This was probably due to the relatively high intensity of the PSFs at the IPs, as compared to the mean background intensities. Thus, an initial thresholding of 30% would prove suitable to obtain a reliable outcome. Of interest, all of the 3D reconstructions from the confocal microscopy recording (for both endosomal and mitochondrial structures) are larger in the Z-axis as compared to those from the TEM recordings. This is due to the Z-dimension of these structures being below the resolution limits of the confocal microscopy. Similarly, the fitting along the XY axes is also satisfactory, with discrepancies in the range of lateral resolution of the confocal microscopy (~200-300 nm). The final 3D reconstructions of both the endosomal and mitochondrial structures of interest, with an initial thresholding of 30% followed by the zero-crossing procedure, and overlapped with the corresponding TEM data, are also shown in the **Supplemental Videos 3.1, 3.2** and **3.3, 3.4**, respectively

After these experiments, the zero-crossing procedure was applied and further tested in 4Pi–microscopy with the 4Pi-CLEM analysis, as reported below.

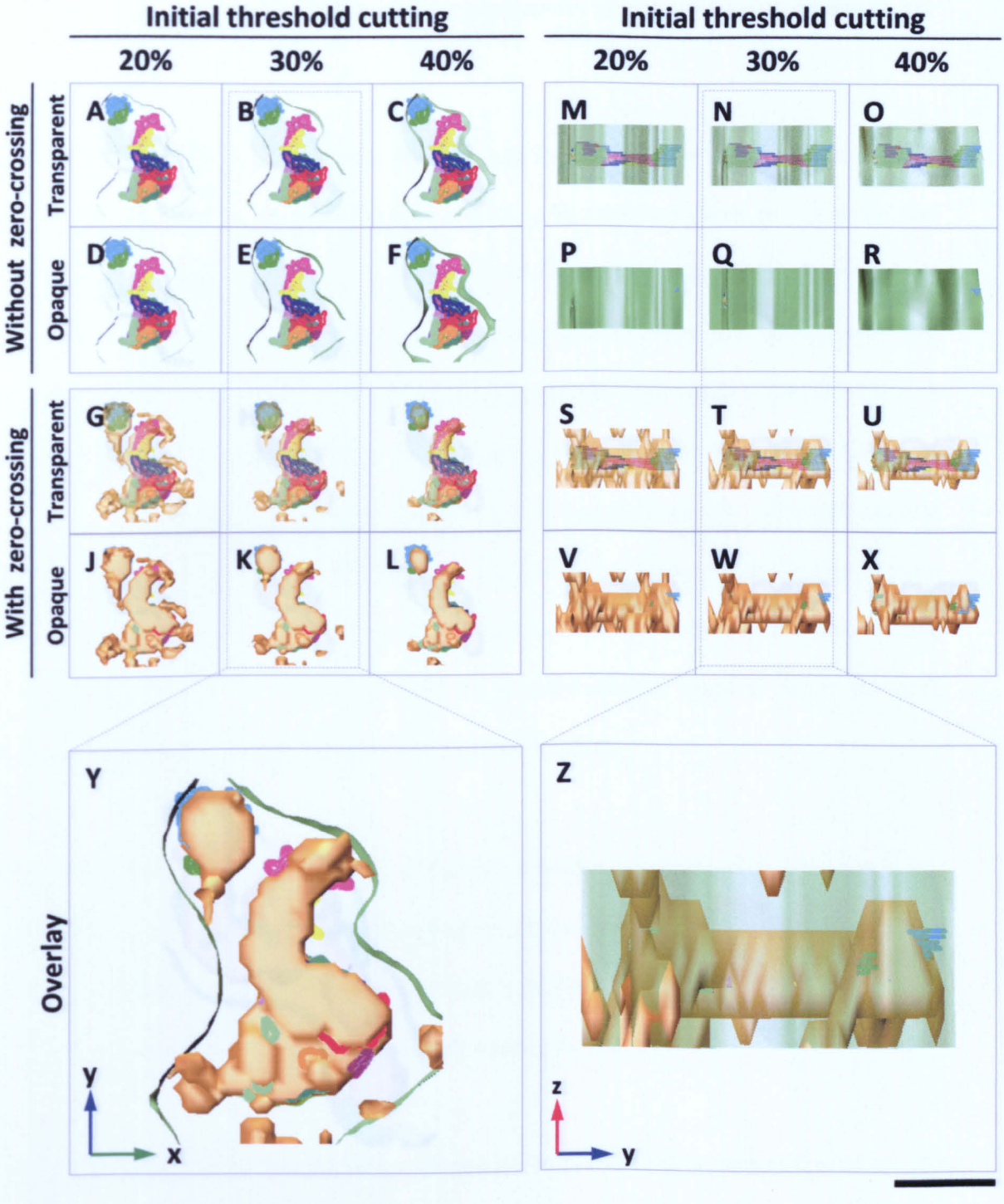

Figure 3.7. The merged confocal and TEM 3D reconstructions of the two endosomal structures.

A-Z, Merged confocal microscopy (as compartments) and TEM (as lines) 3D reconstructions. The individual threshold-intensity and zero-crossing reconstructions are shown in both transparent (A-C, M-O and G-I, S-U, respectively) and opaque (D-F, P-R and J-L, V-X, respectively) modes. Y, Z, overlays for the threshold-intensity and zero-crossing 3D reconstructions (transparent and opaque, respectively) with the TEM 3D reconstruction; note Y-X and Z-Y axis orientations, respectively. For clarity, individual endosomal structures are outlined in different colours, which are maintained between this **Figure** and **Figure 3.4**. Bar, 2 µm (A-X); 630 nm (Y, Z).

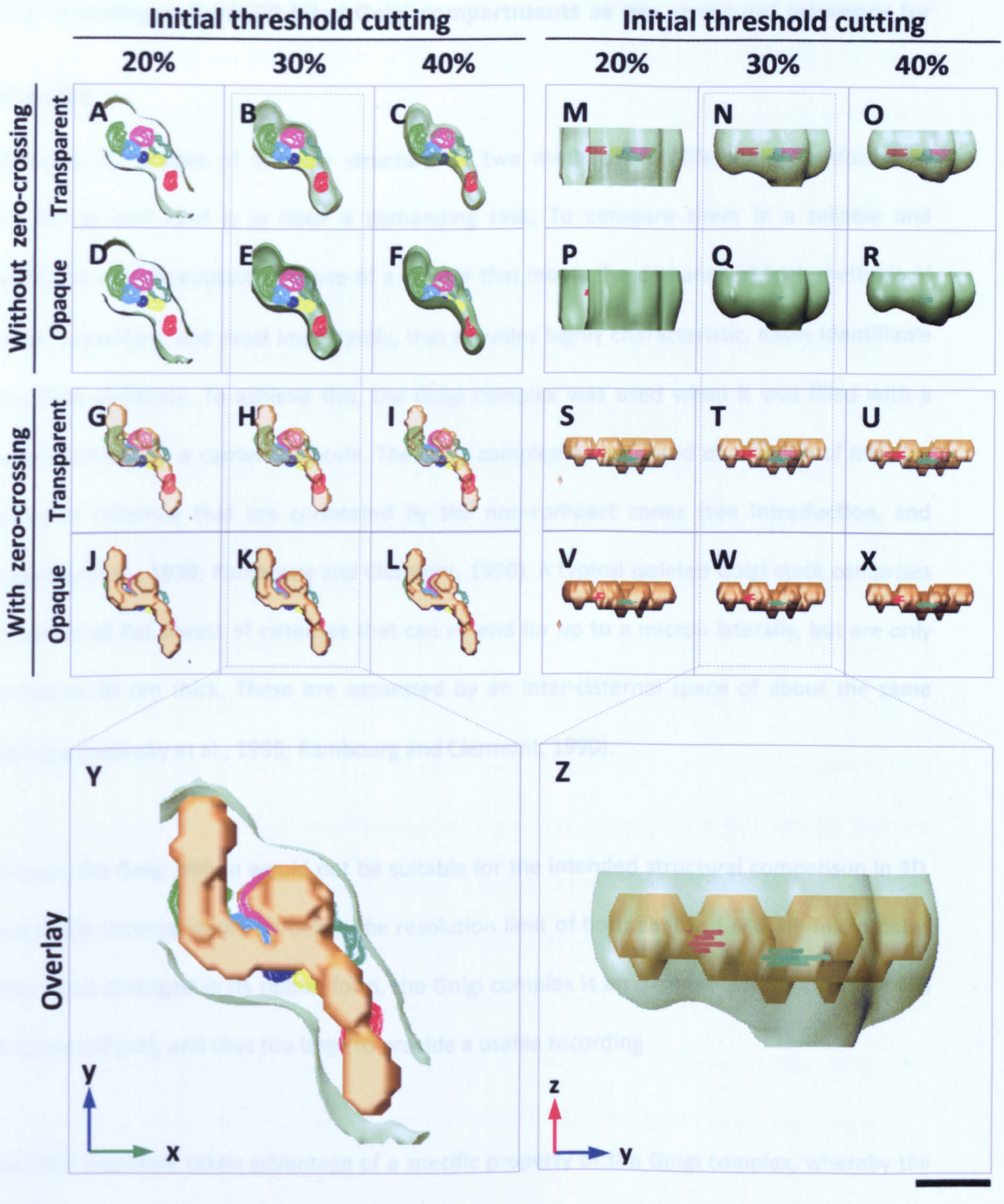

Figure 3.8. The merged confocal and TEM 3D reconstructions of the two mitochondrial structures.

A-Z, Merged confocal microscopy (as compartments) and TEM (as lines) 3D reconstructions. The individual threshold-intensity and zero-crossing reconstructions are shown in both transparent (A-C, M-O and G-I, S-U, respectively) and opaque (D-F, P-R and J-L, V-X, respectively) modes. Y, Z, overlays for the threshold-intensity and zero-crossing 3D reconstructions (transparent and opaque, respectively) with the TEM 3D reconstruction; note Y-X and Z-Y axis orientations, respectively. For clarity, individual endosomal structures are outlined in different colours, which are maintained between this **Figure** and **Figure 3.5**. Bar, 4 µm (A-X); 1,330 nm (Y, Z).

3.2 Procollagen 3-pEGFP-filled Golgi compartments as the structural reference for 4Pi-CLEM

Obtaining 3D images of a single structure by two methods as different as confocal/4Pi-microscopy and TEM is in itself a demanding task. To compare them in a reliable and significant way necessitates the use of a sample that meets the demands of both methods of image acquisition, and most importantly, that provides highly characteristic, easily identifiable structural elements. To achieve this, the Golgi complex was used when it was filled with a fluorescent tag on a carrier molecule. The Golgi complex is composed of a ribbon of multiple stacks of cisternae that are connected by the non-compact zones (see **Introduction**, and (Ladinsky et al., 1999; Rambourg and Clermont, 1990). A typical isolated Golgi stack comprises a number of flat sheets of cisternae that can extend for up to a micron laterally, but are only 20 nm to 30 nm thick. These are separated by an inter-cisternal space of about the same distance (Ladinsky et al., 1999; Rambourg and Clermont, 1990).

As such, the Golgi ribbon would not be suitable for the intended structural comparison in 3D, as a single cisterna would be below the resolution limit of both confocal and 4Pi-microscopy. Also, when arranged in its ribbon form, the Golgi complex is an extremely large structure (up to dozens of μm), and thus too large to provide a usable recording.

We have therefore taken advantage of a specific property of the Golgi complex, whereby the cisternae can become considerably enlarged to accommodate certain large proteins. Our fluorescent carrier here is thus PC, which comprises rod-like proteins of about 300 nm in length and 1.5 nm in diameter (Bachinger et al., 1993). Inclusion of PC in the cisterna lumen leads to the formation of saccular distensions of about 300 nm in diameter, which are located at the lateral ends of the cisternae (Bonfanti et al., 1998). These structures are well below the

axial resolution limit of confocal microscopy, but they should be easily recognisable in 4Pi-microscopy and TEM images. These thus provide an ideal target for this comparative analysis of the 3D reconstructions obtained by the parallel application of the CLEM procedure to 4Pi-microscopy and TEM.

The filling cargo for the Golgi stacks was thus provided by PC type 3 fused with an EGFP tag (PC3-pEGFP), which was expressed in BHK cells. As shown in **Figure 3.9A**, the transfected cells were treated with 300 µM dipyridyl during the 1 h of accumulation at 40 °C. Subsequently, after a washout with new medium containing 100 µg/ml cycloheximide and with 50 µg/ml ascorbic acid the temperature was shifted to 32 °C to allow the PC3-pEGFP to enter the secretory pathway. The the samples were fixed after a further h. Furthermore, to reduce the dimensions of the structures to be recorded, the formation of single Golgi stacks from the Golgi ribbon was induced by treating these cells with 33 µM nocodazole for 1 h (during the PC3-pEGFP traffic block release at 32 °C) before they were fixed. Under these conditions, the Golgi components redistribute from their central position into separate Golgi stacks that are scattered throughout the cytoplasm and have a lateral dimension of about 1 µm (Cole et al., 1996a; Trucco et al., 2004). Under the present experimental conditions, i.e. transport of accumulated cargo in non-polarised cells, such treatment has been shown not to interfere with the transport activity of the PC3-pEGFP through the secretory pathway, at least under the morphological methods of detection employed herein (**Figure 3.9B**) (Trucco et al., 2004).

3.3 Synchronisation of PC3-pEGFP transport in BHK cells

Since hydroxyproline is essential for the creation of the stabilising hydrogen bonds in PC, the folding of the PC triple helices requires hydroxylation of specific prolines by prolyl hydroxylase (Beck et al., 1996). If prolyl hydroxylase is inhibited, PC does not fold and is instead retained in the ER (Beck et al., 1996). Conversely, upon reactivation of prolyl hydroxylase, PC refolds rapidly and exits the ER (Sarras et al., 1991). Thus, by inhibiting and reactivating prolyl hydroxylase, it is possible to synchronise the transport of PC3-pEGFP through the secretory pathway. In detail, 24 h after electroporation with the PC3-pEGFP construct, the cells were treated with 300 µM dipyridyl (Harwood et al., 1976) at 40 °C (Bruckner and Eikenberry, 1984) for 1 h. Both of these treatments completely, but reversibly, inhibit the hydroxylation of the proline residues, thus preventing the exit of PC from the ER (**Figure 3.9**). After dipyridyl washout, new medium containing 50 µg/ml ascorbic acid (an essential reagent for the hydroxylation of the proline residues) was added to allow PC3-pEGFP folding and release (Kim and Peterkofsky, 1997) at 32 °C. One hour was chosen as the timing of the PC3-pEGFP release in the correlative experiments. After fixing of the cells, labelling of the giantin was followed as a Golgi marker, and non-correlative confocal images were recorded (**Figure 3.9**).

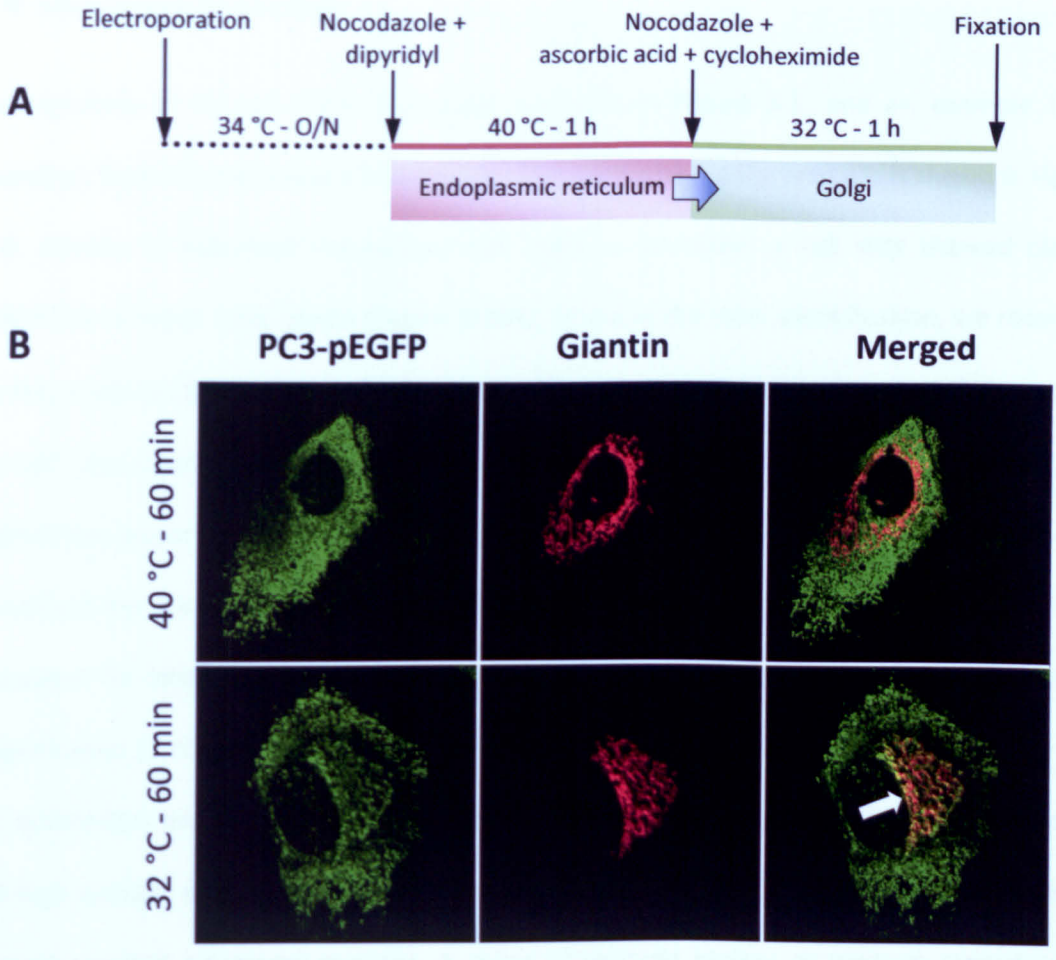

Figure 3.9. Synchronisation of PC3-pEGFP transport in BHK cells.
A, Synchronisation protocol for PC3-pEGFP transport. **B**, After 1 h at 40 °C of block, all of the PC3-pEGFP (green) is in the ER and no co-localisation is seen with the Golgi marker giantin (red). Once the transport is released, the PC3-pEGFP enters the transport pathway through the Golgi complex. In particular, after 1 h of release at 32 °C, co-localisation of PC3-pEGFP with giantin (yellow, white arrow) is evident. Confocal images, 63x magnification.

3.4 Microscopy recordings

The workflow of the 4Pi-CLEM technique is shown in **Figure 3.1**, and an example from recordings from the individual microscopy techniques for two different cells is shown in **Figure 3.10**. Initially, a wide-field microscope was used to pre-select a cell that showed clearly identifiable isolated Golgi stacks (**Figure 3.10A**). To aid in the later identification, we recorded the fluorescence (**Figures 3.1** and **3.10A**) and differential interference contrast (DIC) images of the cell (see **Figures 3.1** and **3.10B**). Next, a confocal 3D sequence of the Golgi stacks of interest was acquired (**Figure 3.10D**), prior to the 4Pi-microscopy recording (**Figure 3.10E**) that completed the fluorescence imaging part of the protocol (**Figure 3.1**).The specimen was then processed for immuno-TEM, and after the cell had again been identified, an initial low-magnification (1,050x) analysis was performed to provide a direct comparison between the DIC microscopy and the TEM imaging (**Figure 3.10C**). Due to the relatively small dimensions and high number of Golgi stacks within the cell, the correct identification of the structures of interest required additional analyses. A series of multiple images at medium magnification (20,500x) was recorded for each slice, to ascertain the identification of the selected Golgi stacks (**Figure 3.10F**). Thereafter, two Golgi stacks of interest (**Figure 3.10D-F**, GS1, GS2) were chosen for the comparative analysis. These Golgi stacks had to be well separated at the light microscopy level and clearly identifiable at the TEM level, while other features regarding their PSFs are detailed below. Moreover, since these Golgi stacks of interest had a different location along the Z-axis, such that they were not identifiable on the same slices, the relative positions with respect to two other reference Golgi stacks were also taken into account (**Figure 3.10D-F**, RG1, RG2). To further test the reliability of 4Pi-microscopy and zero-crossing procedure, the same procedure was carried out with a econd cell (**Figure 3.11**), although without the initial confocal microscopy recording; here, two other larger and structurally more complex Golgi stacks (**Figure 3.11D, E**, GS3, GS4) were analysed.

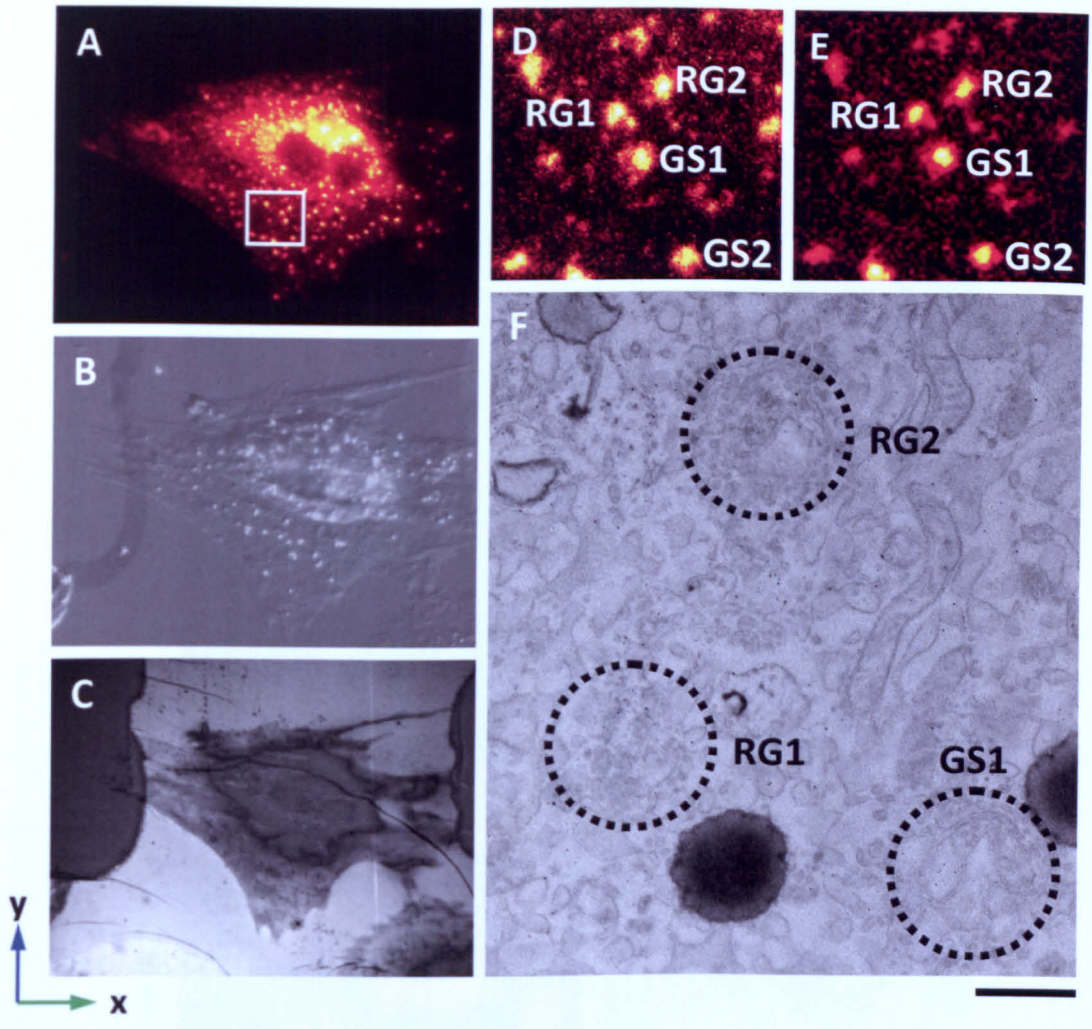

Figure 3.10. Overview of the first BHK cell, with identification of Golgi stacks 1 and 2.
A, Wide-field fluorescent recording. **B**, Wide-field DIC recording. **C**, Low magnification TEM recording. **D** and **E**, Confocal fluorescent and 4Pi-microscopy recordings of Golgi stacks 1 and 2 (GS1, GS2), and reference Golgi stacks 1 and 2 (RG1, RG2). **F**, TEM recording of Golgi stack 1 (GS1), and reference Golgi stacks 1 and 2 (RG1, RG2). Golgi stack 2 is not shown in F, due to its different location along the Z-axis. The white box in **A** represents the field of view for **D** and **E**. Bars, 25 µm (A-C); 5 µm (D, E); 500 µm (F).

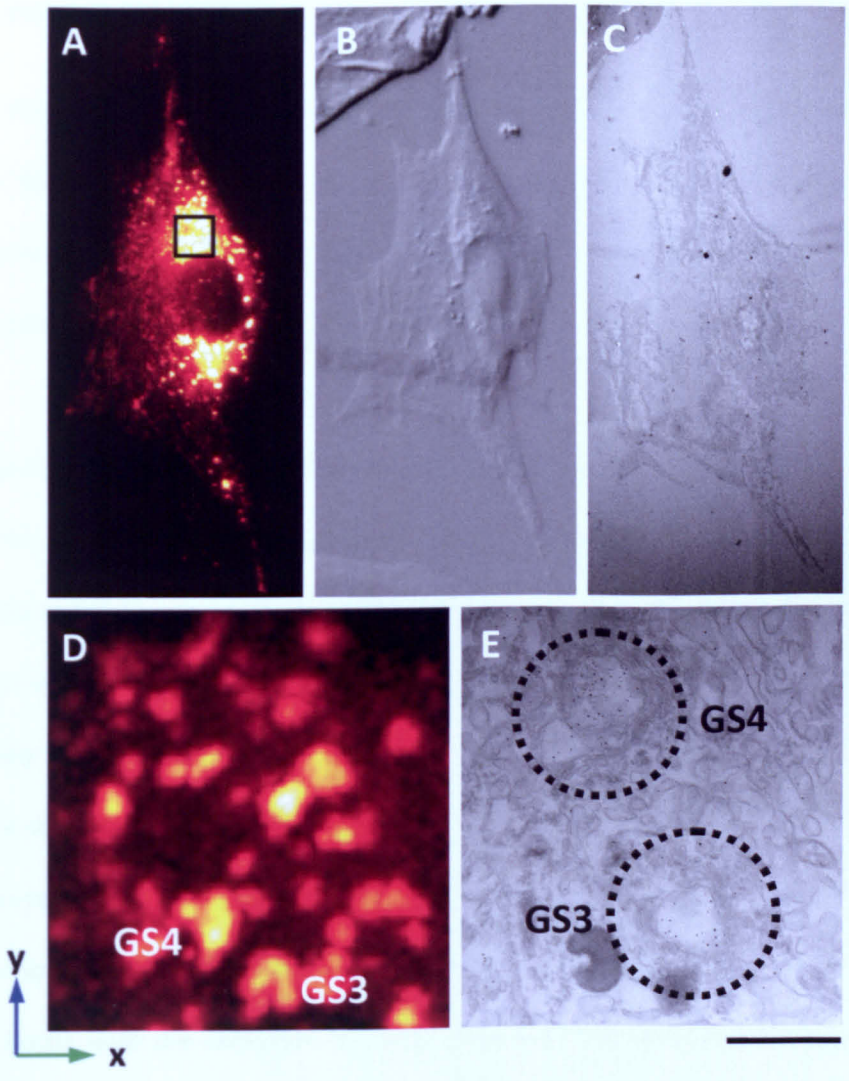

Figure 3.11. Overview of the second BHK cell, with identification of Golgi stacks 3 and 4. **A**, Wide-field fluorescent recording. **B**, Wide-field DIC recording. **C**, Low magnification TEM recording. **D**, 4Pi-microscopy recording of Golgi stacks 3 and 4 (GS3, GS4). **E**, TEM recording of Golgi stacks 3 and 4 (GS3, GS4). The black box in **A** represents the field of view for **D**. Bars, 20 µm (A-C); 15 µm (D); 700 µm (E).

3.5 Three-point deconvolution of the 4Pi-microscopy data

A feature of 4Pi-microscopy recordings is the formation of side lobes as part of the PSF (see **Introduction, Section 1.1.e**) (Hell, 2003). These were initially removed using a deconvolution procedure (Schrader et al., 1998) that was applied prior to the 3D reconstruction (smoothing and segmentation) of the final images (see also **Material and Methods, Section 2.6.c**).

The PSF of the four Golgi stacks 1-4 are shown in **Figure 3.12**. For a better understanding of the reliability of the 4Pi-microscopy principle and three-point deconvolution, Golgi stacks showing PSFs with different features were chosen. In particular, Golgi stacks 1 and 4 of **Figure 3.12** featured symmetrical PSFs, Golgi stack 3 featured a slightly asymmetrical PSF, and Golgi stack 2 featured a fully asymmetrical PSF. The side lobes were also about 50% and 80% as compared with the main lobe in Golgi stacks 1 and 4, respectively. In Golgi stack 3, the side lobes were about 75%, as compared with the main lobe, and finally, in Golgi stack 2 they were about 90% and 40% of the main lobe. All of the PSFs analysed showed a satisfactory spatial invariance through the Z-axis, with the exception for Golgi stack 4 (not shown), and the parameters for filtering in the three-point deconvolution were set by an analysis of the brightest slice of those recorded through the same axis. When a deconvolution was judged unsatisfactory in terms of side lobe removal, a second deconvolution with slightly different parameters was run. The quality of the deconvolution outcomes were based on a subjective judgement (see also **Introduction, Section 1.1.e**).

The results of the deconvolution are also shown in **Figure 3.12**. Different outcomes were noted for the four Golgi stacks. The best side lobe removal was seen for Golgi stack 1, and also for Golgi stack 3, although, here two small shoulders on the main lobe (representing the remaining side lobes) were still present. Golgi stack 4 yielded a final PSF with an irregular

shape, enlarged and asymmetrical, in which more than two shoulders were present after the three-point deconvolution. Finally, Golgi stack 2 produced a symmetrical deconvolved PSF, but with two evident side lobes of up to 40% of the main lobe still present.

Taken together, all of these observations show that the best side lobe removal by three-point deconvolution is achieved when they are not very pronounced within a symmetrical PSF (as in Golgi stack 1). However, if the side lobes are up to 75% of the main lobe, and the PSF has a slightly asymmetrical shape, they can still be removed satisfactorily (as in Golgi stack 3). On the other hand, if the PSF is strongly asymmetrical, as in the case of Golgi stack 2, the results will fail in terms of side lobes removal. Finally, even in cases in which the PSF has a symmetrical shape and well separated side lobes, as in Golgi stack 4, the three-point deconvolution can significantly alter the shape of the main lobe if the spatial invariance through the Z-axis is not preserved during the recording.

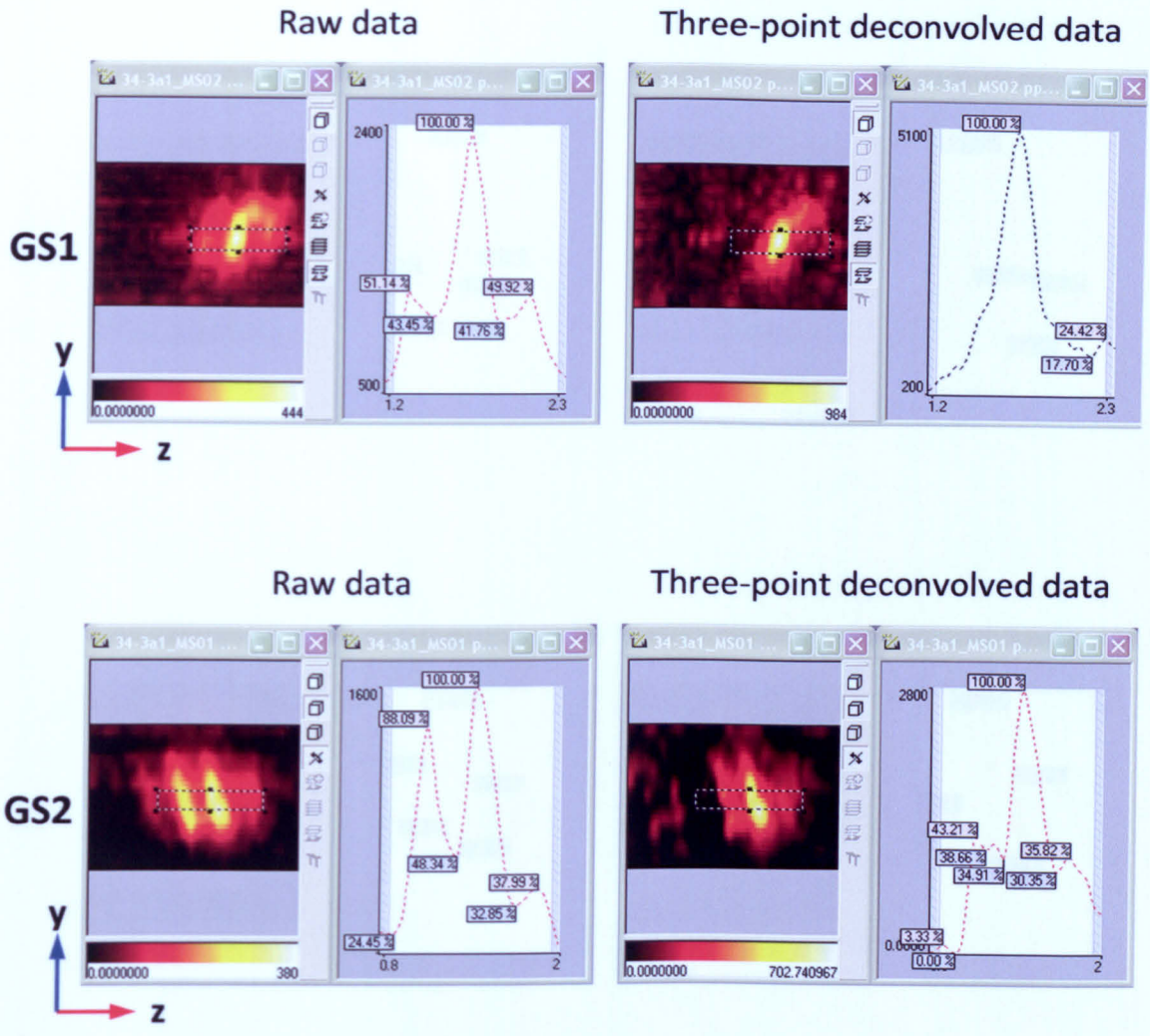

Figure 3.12. Point-spread functions for Golgi stacks 1-4, before (raw data) and after three-point deconvolution.

GS1, Golgi stack 1; **GS2**, Golgi stack 2. In each section, the left panel shows the fluorescent recording, and the right panel shows the PSF relative to the dashed box on the corresponding fluorescent recording (Imspector software output).

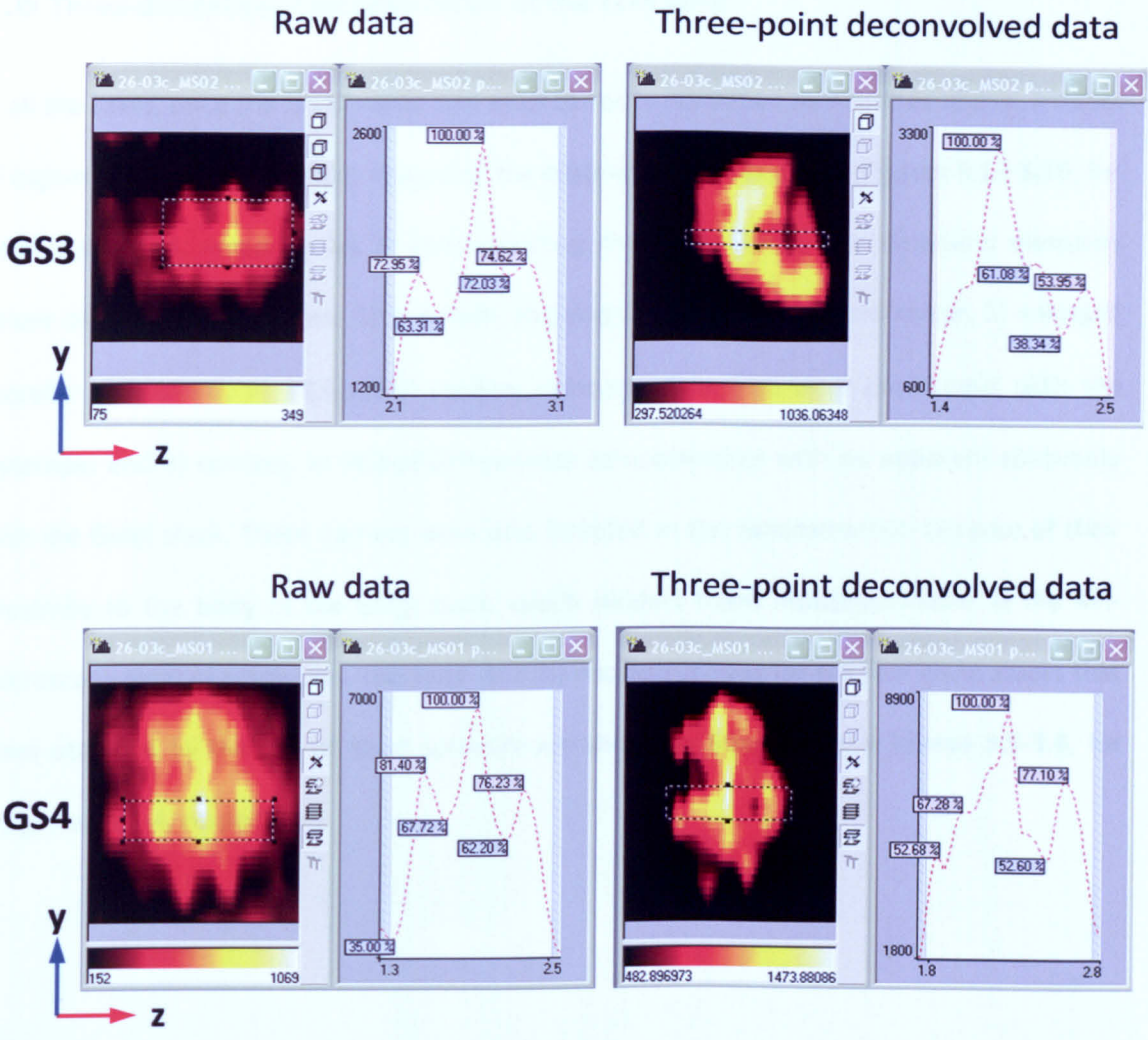

Figure 3.12. Continued.

GS3, Golgi stack 3; **GS4**, Golgi stack. 4. In each section, the left panel shows the fluorescent recording, and the right panel shows the PSF relative to the dashed box on the corresponding fluorescent recording (Imspector software output).

3.6 Three-dimensional reconstruction of the TEM data

In all the cases, once the Golgi stacks had been correctly identified as indicated above, a series of high-magnification (43,500x) images of the organelles was recorded (**Figures 3.13-3.16**, for Golgi stacks 1-4, respectively). In reconstructing the Golgi stacks, the structural elements where categorised as follows: 1) *cisternae*, showing the typical elongated shape; 2) enlarged *saccular distensions*, as PC3-pEGFP-positive compartments that were continuous with the cisternae; and 3) *carriers,* as PC3-pEGFP-positive compartments with no apparent continuity with the Golgi stack. These carriers were also included in the reconstruction because of their proximity to the body of the Golgi stack, which renders them indistinguishable at the 4Pi-microscopy level of resolution. The final TEM 3D reconstructions for the four Golgi stacks that were obtained by the use of Imod software are shown in **Supplemental Videos 3.5-3.8**, for Golgi stacks 1-4, respectively.

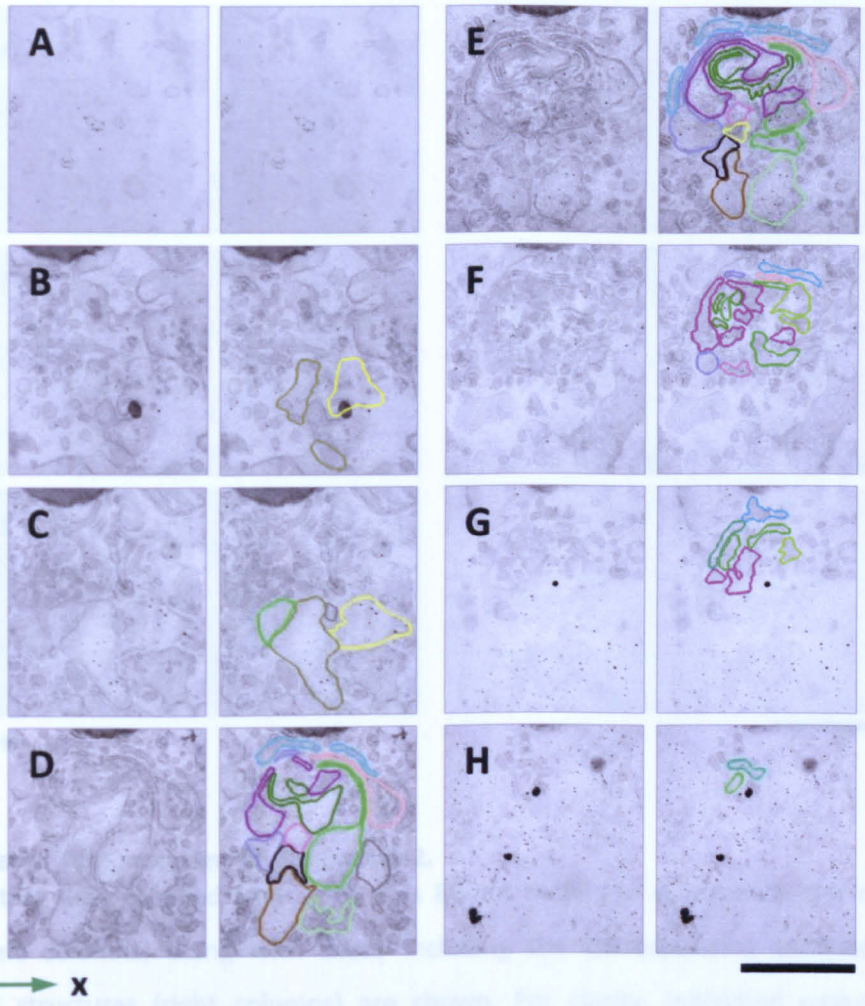

Figure 3.13. Serial TEM recording of Golgi stack 1.
Each consecutive slice, labelled from **A** to **H**, is 80-nm thick. For every slice, the raw TEM recordings (left columns) along with those including the corresponding outlines of the reconstructed structures (right columns) are shown. For clarity, individual cisternae and carriers are outlined in different colours, which are maintained between this **Figure** and **Figure 3.19**. Bar, 500 nm.

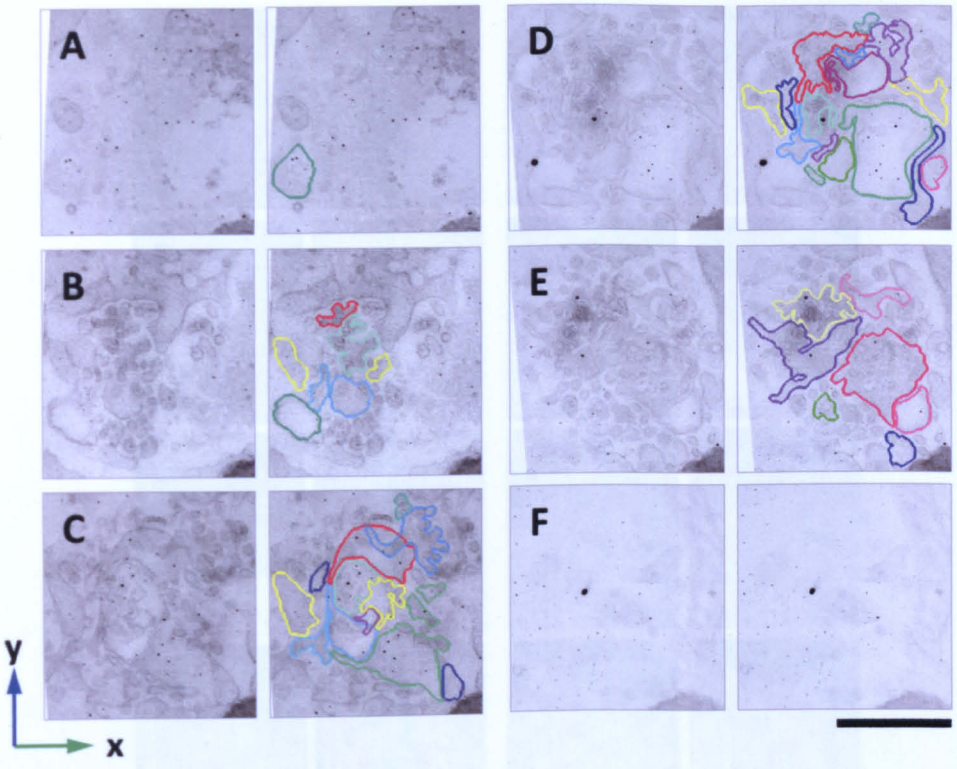

Figure 3.14. Serial TEM recording of Golgi stack 2.
Each consecutive slice, labelled from **A** to **F**, is 80-nm thick. For every slice, the raw TEM recordings (left columns) along with those including the corresponding outlines of the reconstructed structures (right columns) are shown. For clarity, individual cisternae and carriers are outlined in different colours, which are maintained between this **Figure** and **Figure 3.20**. Bar, 1 µm.

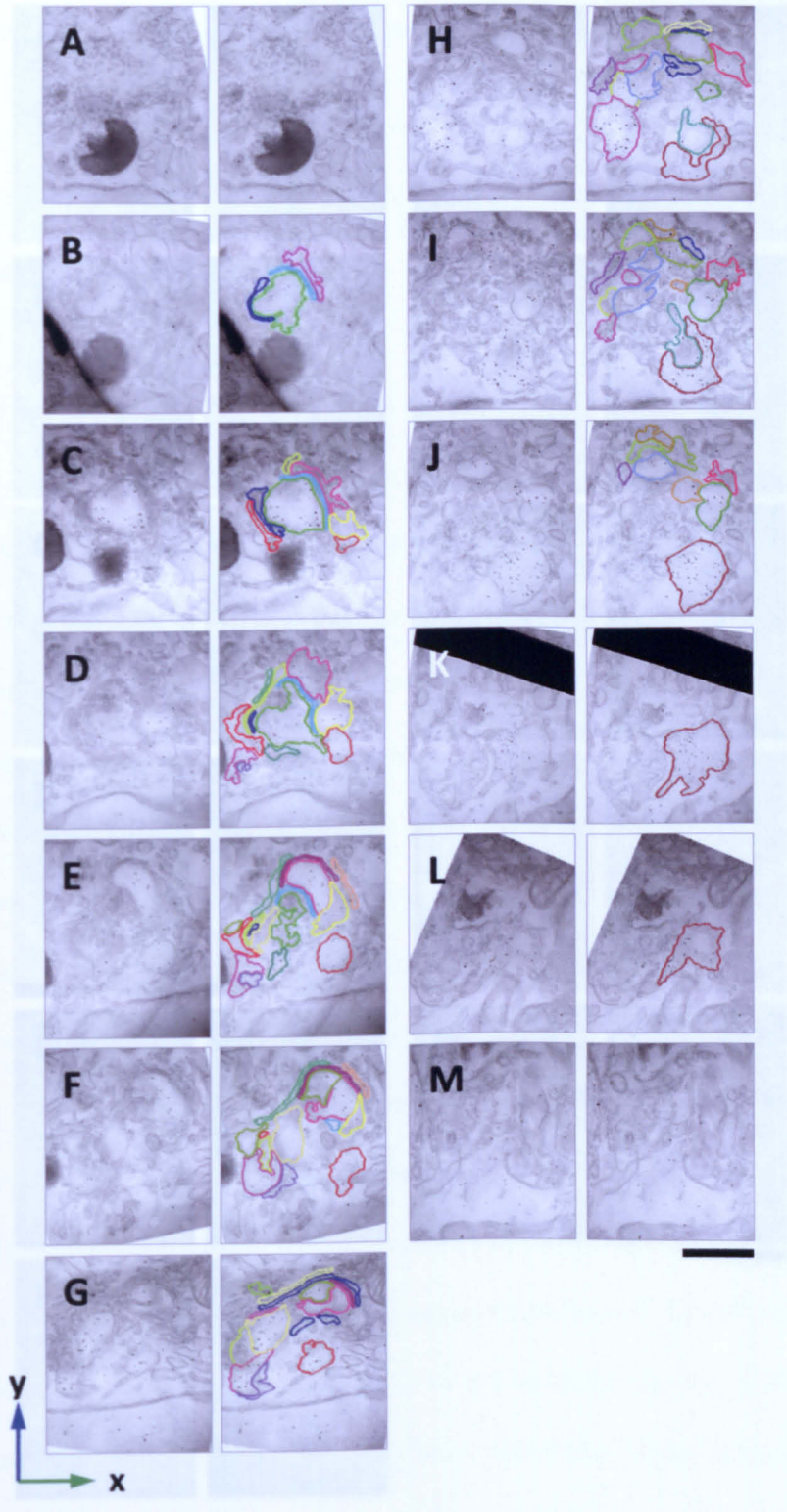

Figure 3.15. Serial TEM recording of Golgi stack 3.
Each consecutive slice, labelled from **A** to **M**, is 80-nm thick. For every slice, the raw TEM recordings (left columns) along with those including the corresponding outlines of the reconstructed structures (right columns) are shown. For clarity, individual cisternae and carriers are outlined in different colours, which are maintained between this **Figure** and **Figure 3.21**. Bar, 500 nm.

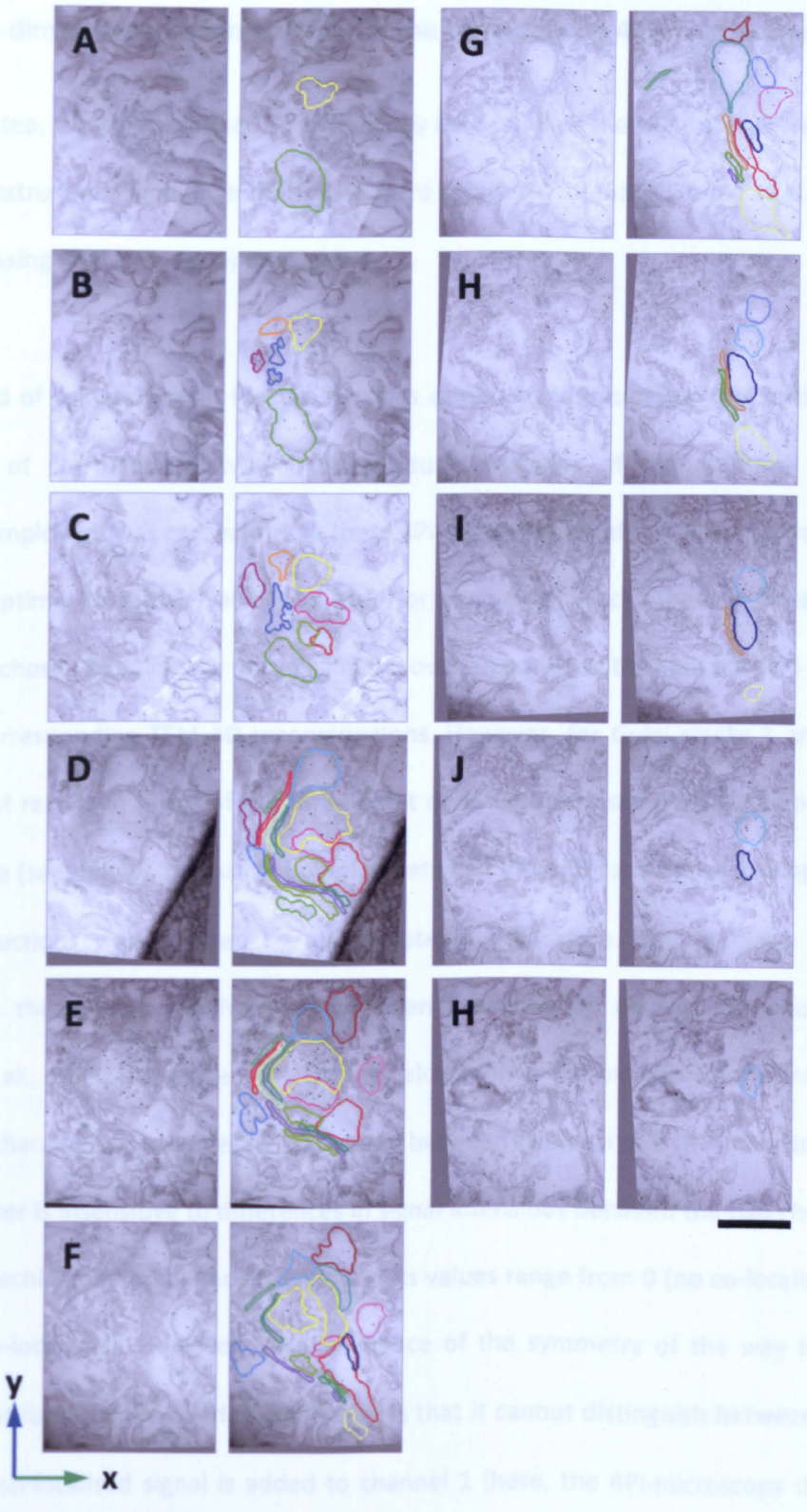

Figure 3.16. Serial TEM recording of Golgi stack 4.
Each consecutive slice, labelled from **A** to **M**, is 80-nm thick. For every slice, the raw TEM recordings (left columns) along with those including the corresponding outlines of the reconstructed structures (right column) are shown. For clarity, individual cisternae and carriers are outlined in different colours, which are maintained between this **Figure** and **Figure 3.22**. Bar, 500 nm.

3.7 Three-dimensional reconstruction of the confocal and 4Pi-microscopy data

In the next step, the confocal and 4Pi-microscopy data of all of the Golgi stacks were used for the 3D reconstruction, again by both the standard threshold-intensity (Young et al., 1995) and the zero-crossing (O'Haver, 1979) procedures.

Here, instead of using different threshold values as above, computiation and optimisation of the degree of correlation between the various thresholds of the confocal microscopy (whenever employed) was carried out. In these 4Pi-microscopy and the TEM reconstructions, a single and optimal threshold value was used for each Golgi stack. These optimal threshold values were chosen by manually maximising the overlap between the confocal/4Pi-microscopy and their corresponding TEM 3D reconstructions. However, for Golgi stacks 1 and 3, which gave the best results in terms of the three-point deconvolution (see above) and overlap with the TEM data (see below), the highest overlap between the different 4Pi-microscopy and TEM 3D reconstructions were chosen by appropriate quantification. The Manders coefficient, representing the overlapping fractions between the volumes of two 3D reconstructions (Manders et al., 1993), were used. Briefly, the calculation of the overlap coefficient is another method for characterising the degree of overlap between two channels in a microscopy image. This parameter is insensitive to differences in signal intensities between the two channels, and to photo-bleaching and amplifier settings, and its values range from 0 (no co-localisation) to 1 (all pixels co-localised). However, a consequence of the symmetry of the way both of the channels contribute to the overlap coefficient is that it cannot distinguish between situations when a not co-localised signal is added to channel 1 (here, the 4Pi-microscopy data) *versus* channel 2 (here, the TEM data). To cancel out this effect, the overlap coefficient can be split into two different coefficients, the so-called Manders coefficients k1 and k2 (Manders et al., 1993). Here, k1 represents the percentage of 4Pi-microscopy 3D reconstruction volume co-

localising with the corresponding TEM 3D reconstruction, while k2 represents its counterparts, which is the fraction of TEM 3D reconstruction volume co-localising with the corresponding 4Pi-microscopy 3D reconstruction. Therefore, using the standard threshold-intensity procedure, the volume of the 4Pi 3D reconstruction, and thus k1 and k2, depend directly on the choice of the threshold value itself. At the best thresholding in terms of maximum co-localisation, k1 and k2 are equal (see **Figure 3.17**). Finally, by analysing the k1 and k2 Manders coefficient curves, the optimal threshold levels for the 4Pi recordings were extrapolated (see **Figure 3.17A, B** for Golgi stacks 1 and 3, respectively). The calculation of the Manders coefficients of confocal/TEM structures was omitted because of the evident mismatch of resolution along the optical axis (see **Figures 3.19** and **3.20**, top rows, for Golgi stacks 1 and 2, respectively), giving any comparison little meaning.

After these manual and quantitative analyses, the full values chosen for the threshold-intensity procedure were between 26% and 38% for the various confocal/4Pi-microscopy 3D reconstructions (see also below). In particular, the use of the intersection of the Manders coefficient resulted in an intensity threshold of the maximum intensity of the corresponding PSF with the values of 26% and 35% chosen for Golgi stacks 1 and 3, respectively, under 4Pi-microscopy (see **Figure 3.17A, B**).

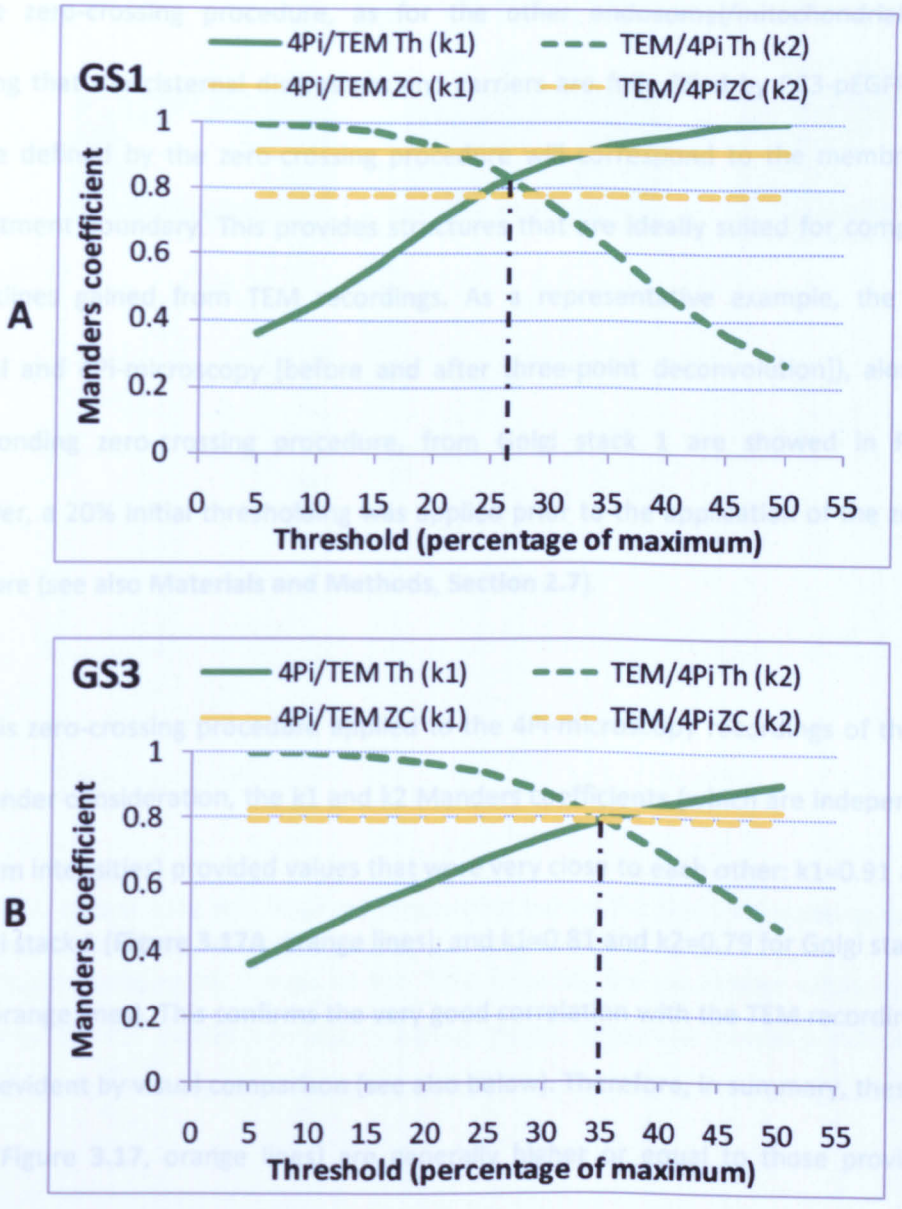

Figure 3.17. Manders coefficients for the 4Pi-microscopy and TEM recordings.
GS1, Golgi stack 1; **GS3**, Golgi stack 3. For the 3D-reconstructions using the threshold-intensity procedure, the crossing of the 4Pi-microscopy/TEM and TEM/4Pi-microscopy (green) curves provides the best Manders coefficients, which correspond to threshold levels of 26% (**A**) and 35% (**B**) of the maximum intensities of the signals for GS1 and GS3, respectively. **4Pi/TEM**, percentage of the 4Pi-microscopy 3D reconstruction filled by the corresponding TEM 3D reconstruction (k1); **TEM/4Pi**, percentage of the TEM 3D reconstruction filled by the corresponding 4Pi-micoscopy 3D reconstruction (k2); **Th**, threshold-intensity procedure; **ZC**, zero-crossing procedure.

For the zero-crossing procedure, as for the other endosomal/mitochondrial structures, assuming that the cisternal distensions and carriers are fully filled by PC3-pEGFP, the edges that are defined by the zero-crossing procedure will correspond to the membranes of the compartment boundary. This provides structures that are ideally suited for comparison with the outlines gained from TEM recordings. As a representative example, the PSFs (from confocal and 4Pi-microscopy [before and after three-point deconvolution]), along with the corresponding zero-crossing procedure, from Golgi stack 1 are showed in **Figure 3.18**. Moreover, a 20% initial thresholding was applied prior to the application of the zero-crossing procedure (see also **Materials and Methods, Section 2.7**).

With this zero-crossing procedure applied to the 4Pi-microscopy recordings of the two Golgi stacks under consideration, the k1 and k2 Manders coefficients (which are independent of the maximum intensities) provided values that were very close to each other: k1=0.91 and k2=0.78 for Golgi stack 1 (**Figure 3.17A**, orange lines); and k1=0.81 and k2=0.79 for Golgi stack 3 (**Figure 3.17B**, orange lines). This confirms the very good correlation with the TEM recordings that was already evident by visual comparison (see also below). Therefore, in summary, these k1 and k2 values (**Figure 3.17**, orange lines) are generally higher or equal to those provided by the intersection of the curves for the threshold-based segmentation procedure (**Figure 3.17**, green lines), indicating higher total overlap and thus superior definition of the organelle boundaries.

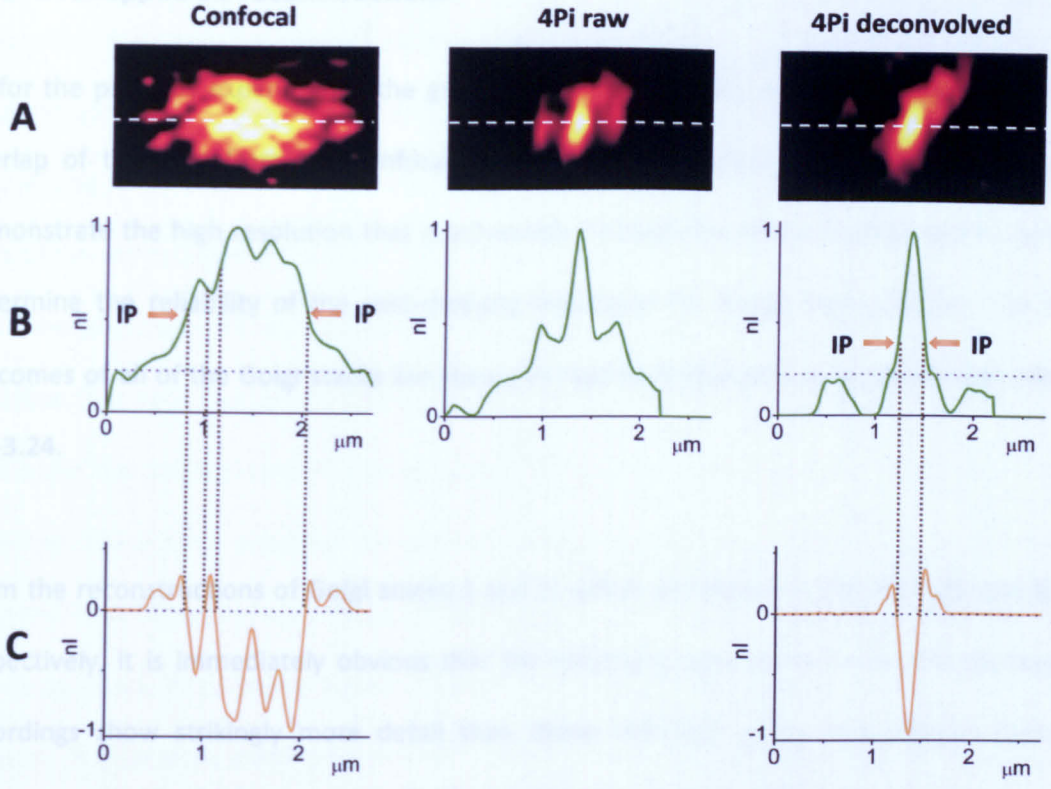

Figure 3.18. Actual PSFs and their corresponding curves for the zero-crossing procedure in the confocal and 4Pi-microscopy recordings of Golgi stack 1.

A, Microscopy imaging; **B**, Curves of the PSFs detected for the dotted white lines in **A**; **C**, Curves from the PSF curves upon zero-crossing. Dotted horizontal lines in B indicate the intial thresholding; **IP**, inflection point (where the slope is maximum); **nI**, normalised intensity.

3.8 Overlapped 3D reconstructions

As for the previous experiments, the goal of this 4Pi-CLEM procedure was to define the 3D overlap of the data from the confocal/4Pi-microscopy and TEM recordings, to ultimately demonstrate the high resolution that is achievable through the 4Pi-technology and to further determine the reliability of the zero-crossing procedure for image segmentation. The final outcomes of all of the Golgi stacks are shown in **Figures 3.19-3.24** and **Supplemental Videos 3.9-3.24**.

From the reconstructions of Golgi stacks 1 and 2, which are shown in **Figures 3.19** and **3.20**, respectively, it is immediately obvious that the structures derived from the 4Pi-microscopy recordings show strikingly more detail than those obtained under conventional confocal microscopy. As would be expected, the four-fold to five-fold resolution enhancement of the 4Pi-microscopy, as compared to the confocal microscopy, leads to significant improvements in the structural reconstruction along the Z-axis for both Golgi stacks 1 and 2 (**Figures 3.19** and **3.20**, top, respectively).

For each of the 4Pi-microscopy recordings, the degree of overlap with the TEM-derived structures was different among the Golgi stacks. In particular, for both Golgi stacks 1 and 3 (**Figures 3.19** and **3.21**, and **Supplemental Videos 3.9-3.12** and **3.17-3.20**, respectively) this overlap was satisfactory.

Analyses of the correlation of the 4Pi-microscopy structures with those from the TEM showed discrepancies between these two techniques that were in the range of 100-200 nm, and thus within the order of magnitude of the resolution difference between 4Pi-microscopy and TEM, as would be expected. Generally, the 3D reconstructions from the 4Pi-microscopy were slightly

larger when compared to those from the corresponding TEM data (**Figures 3.19/3.20A-J**); this is an effect that probably arises from the slight shrinkage that inevitably occurs during sample preparation for TEM. Additionally, a slight overestimation of the Golgi stack volumes in 4Pi-microscopy reconstructions might occur due to minor structural details below the resolution limit of the microscope. At the same time, some of the TEM structures (mainly for Golgi stack 1) extended outside the 4Pi-microscopy reconstructions (**Figure 3.19E-J**). However, these are cisternae that have the classical flat and elongated structures, and as such they are too small to contain the 300-nm-long PC3-pEGF molecules, in contrast to the distensions filled by the EGFP tag. These same cisternae did not show any gold labelling in the non-overlapping areas from the TEM, in parallel with the lack of fluorescent tag in the 4Pi-microscopy reconstructions (for Golgi stack 1, compare **Figure 3.13D-F** with **Figure 3.19E-J**). On the other hand, the distensions that were positive for the EGFP tag in TEM images always appeared to be almost completely within the 4Pi-microscopy reconstructions (**Figures 3.19** and **3.21**, and **Supplemental Videos 3.11** and **3.19**, for Golgi stacks 1 and 3, respectively).

This is also reflected in the Manders coefficients of the structures segmented by the zero-crossing procedure (**Figure 3.17A**, orange lines), where account is not taken of the concept of differential protein distributions within the different structural elements. This would explain the comparatively large difference between k1 and k2 for zero-crossing-segmented Golgi stack 1 (**Figure 3.17A**), and why the Manders coefficients were generally large, at up to 0.9, but not exactly 1.0.

Also of note, with the 4Pi-microscopy data, the intersections of the Manders coefficient curves for Golgi stacks 1 and 3 provided different threshold settings (26% and 35%, respectively), demonstrating the poor repeatability of the threshold method, and thus again the superiority of the zero-crossing procedure.

On the contrary, the other two Golgi stacks, 2 and 4 (**Figures 3.20** and **3.22**, respectively), showed a lower degree of overlap with the corresponding TEM 3D reconstructions, especially for Golgi stack 2. At the 4Pi-microscopy level, either non-genuine extra compartments (Golgi stack 2, **Figure 3.20E-J**) or missing portions (Golgi stack 4, **Figure 3.22A-D, I**) were noted, as compared to the TEM 3D reconstructions (see also **Supplemental Videos 3.13-3.16** and **3.21-3.24**, for Golgi stacks 2 and 4, respectively).

Of note, the two Golgi stacks 1 and 3 that were characterised by symmetrical and invariant PSFs (even with high side lobes) yielded the best results in terms of the overlap with the corresponding TEM data; the other Golgi stacks, 2 and 4, were characterised by asymmetrical or variable PSFs, respectively, and produced less reliable outcomes. These comparative analyses thus initially demonstrate that the reliability of the 4Pi-microscopy outcome can be predicted on the basis of the PSF features before and after the three-point deconvolution. Moreover, they also show the reliability of the objective zero-crossing-based procedure that can be coupled to 4Pi-microscopy.

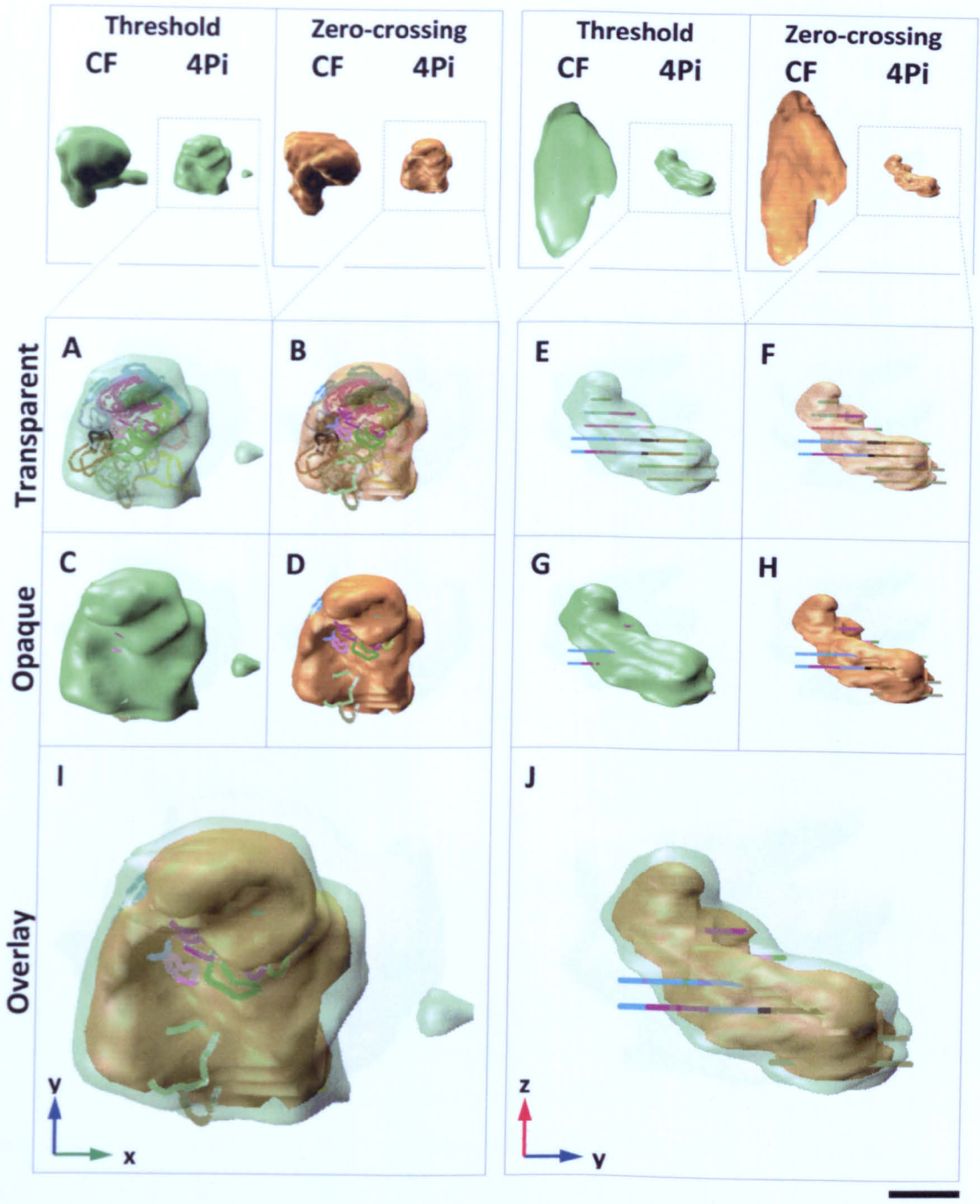

Figure 3.19. Confocal/4Pi-microscopy and TEM 3D reconstructions of Golgi stack 1.
A-J, Merged 4Pi-microscopy (as compartments) and TEM (as lines) 3D reconstructions. The individual threshold-intensity and zero-crossing 4Pi-microscopy 3D reconstructions are shown in both transparent (A, B, E, F) and opaque (C, D, G, H) modes. **I, J,** Overlays for the threshold-intensity and zero-crossing 4Pi-microscopy 3D reconstructions (transparent and opaque, respectively) with the TEM 3D reconstruction; note Y-X and Z-Y axis orientations, respectively. For clarity, individual cisternae and carriers are outlined in different colours, which are maintained between this **Figure** and **Figure 3.13**. Bar, 1,250 nm (top panels); 500 nm (A-H); 250 nm (I, J). **Threshold**, threshold-intensity procedure; **Zero-crossing**, zero-crossing procedure; **CF**, confocal microscopy; **4Pi**, 4Pi-microscopy. The threshold levels for the maximum intensities were set at 35% for the confocal microscopy and 26% for the 4Pi-microscopy.

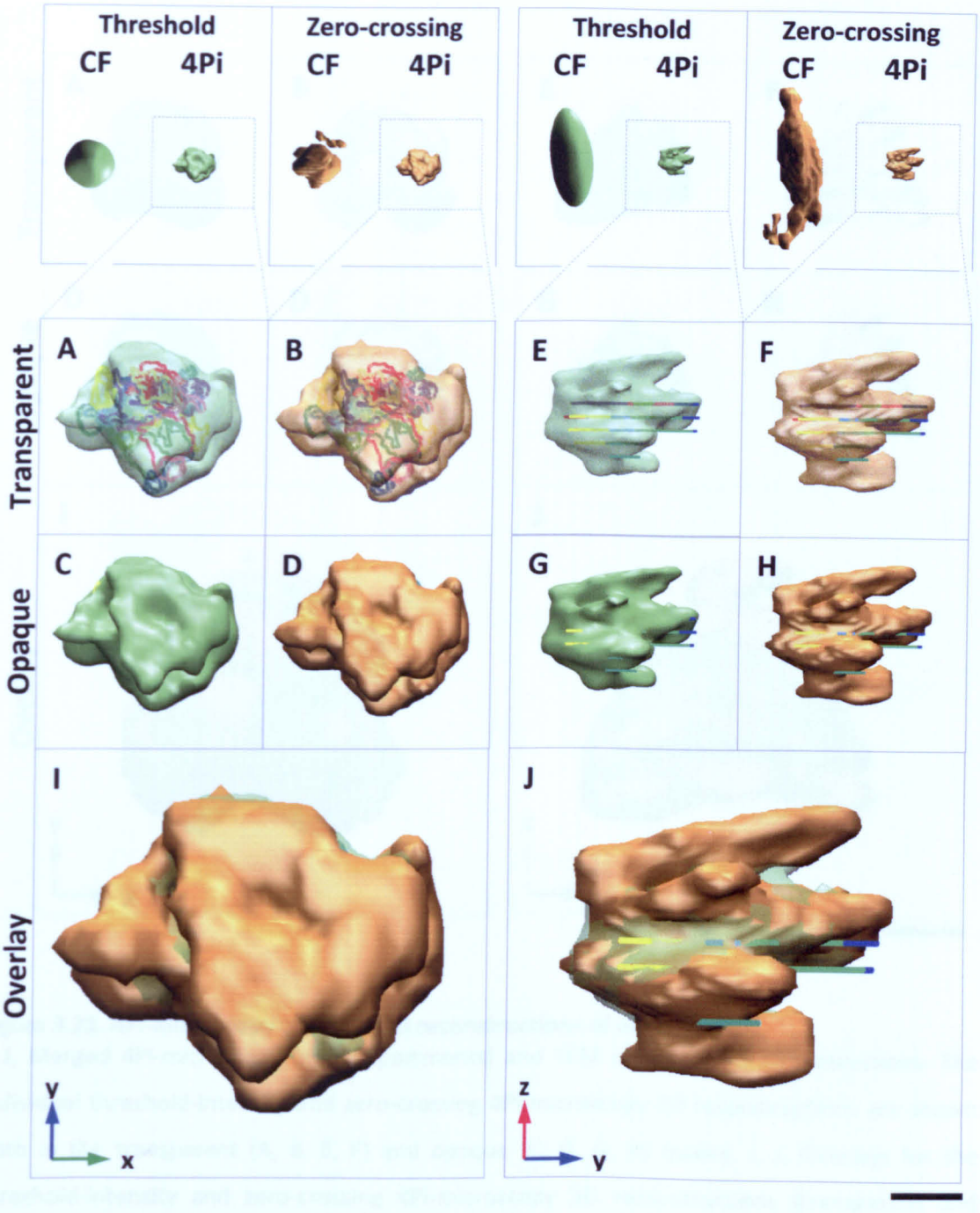

Figure 3.20. Confocal/4Pi-microscopy and TEM 3D reconstructions of Golgi stack 2.
A-J, Merged 4Pi-microscopy (as compartments) and TEM (as lines) 3D reconstructions. The individual threshold-intensity and zero-crossing 4Pi-microscopy 3D reconstructions are shown in both transparent (A, B, E, F) and opaque (C, D, G, H) modes. I, J, Overlays for the threshold-intensity and zero-crossing 4Pi-microscopy 3D reconstructions (transparent and opaque, respectively) with the TEM 3D reconstruction; note Y-X and Z-Y axis orientations, respectively. For clarity, individual cisternae and carriers are outlined in different colours, which are maintained between this **Figure** and **Figure 3.14**. Bar, 2 µm (top panels); 1 µm (A-H); 500 nm (I, J). **Threshold**, threshold-intensity procedure; **Zero-crossing**, zero-crossing procedure; **CF**, confocal microscopy; **4Pi**, 4Pi-microscopy. The threshold levels for the maximum intensities were set at 32% for the confocal microscopy and 27% for the 4Pi-microscopy.

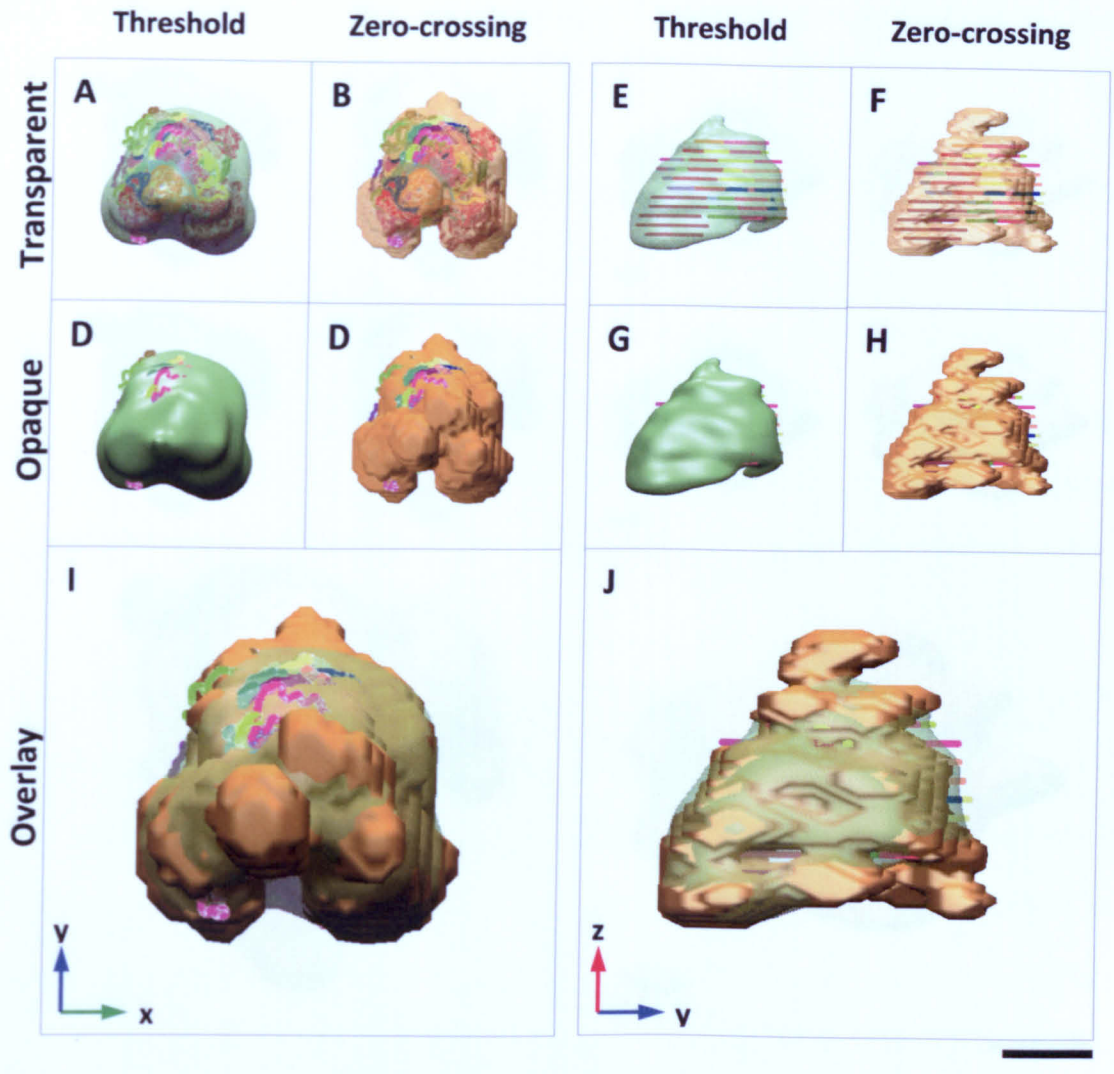

Figure 3.21. 4Pi-microscopy and TEM 3D reconstructions of Golgi stack 3.
A-J, Merged 4Pi-microscopy (as compartments) and TEM (as lines) 3D reconstructions. The individual threshold-intensity and zero-crossing 4Pi-microscopy 3D reconstructions are shown both in the transparent (A, B, E, F) and opaque (C, D, G, H) modes. I, J, Overlays for the threshold-intensity and zero-crossing 4Pi-microscopy 3D reconstructions (transparent and opaque, respectively) with the TEM 3D reconstruction; note Y-X and Z-Y axis orientations, respectively. For clarity, individual cisternae and carriers are outlined in different colours, which are maintained between this **Figure** and **Figure 3.15**. Bar, 1 µm (A-H); 500 nm (I, J). **Threshold**, threshold-intensity procedure; **Zero-crossing**, zero-crossing procedure. The threshold level for the maximum intensity was set at 35%.

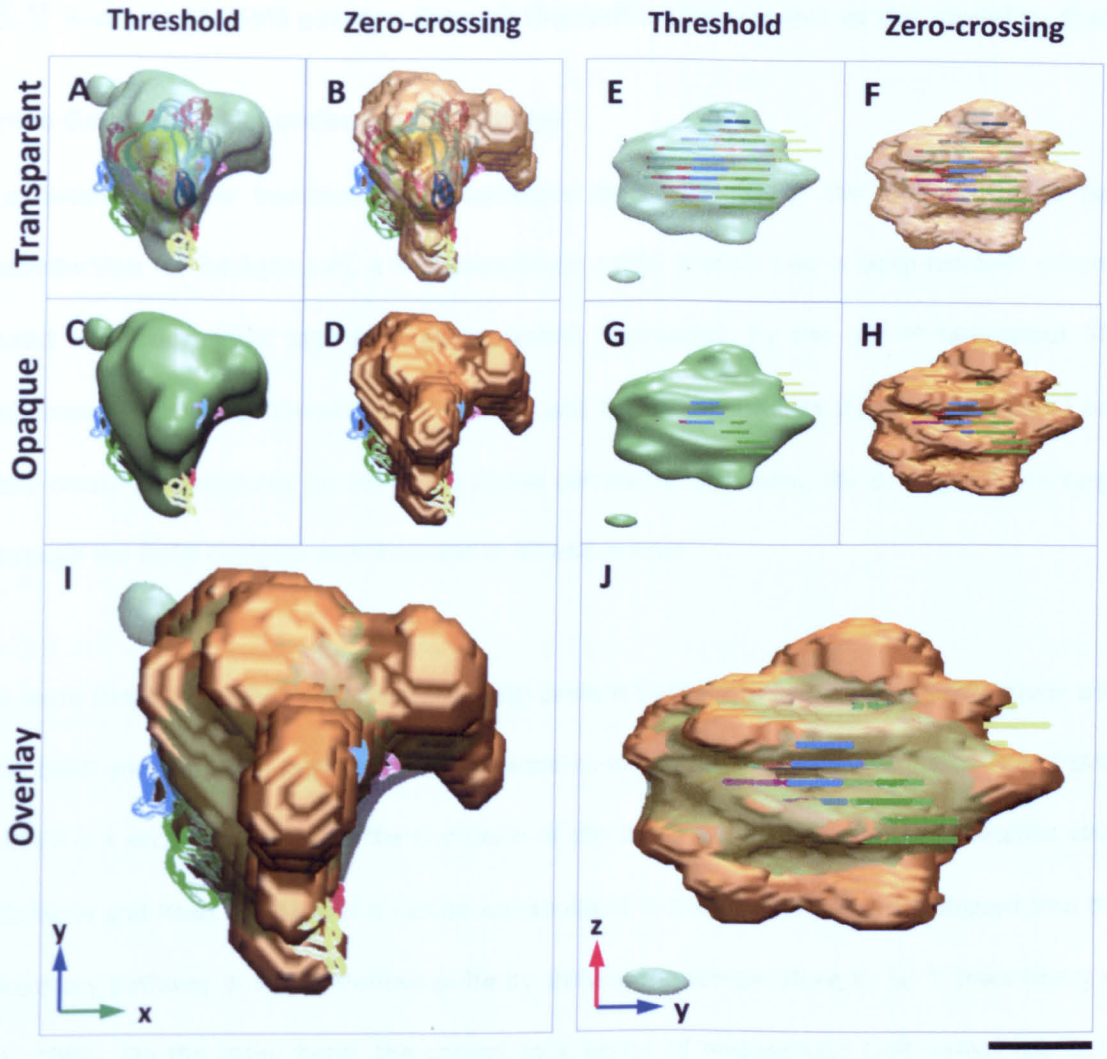

Figure 3.22. 4Pi-microscopy and TEM 3D reconstructions of Golgi stack 4.
A-J, Merged 4Pi-microscopy (as compartments) and TEM (as lines) 3D reconstructions. The individual threshold-intensity and zero-crossing 4Pi-microscopy 3D reconstructions are shown both in the transparent (A, B, E, F) and opaque (C, D, G, H) modes. I, J, Overlays for the threshold-intensity and zero-crossing 4Pi-microcopy 3D reconstructions (transparent and opaque, respectively) with the TEM 3D reconstruction; note Y-X and Z-Y axis orientations, respectively. For clarity, individual cisternae and carriers are outlined in different colours, which are maintained between this **Figure** and **Figure 3.16**. Bar, 1 μm (A-H); 500 nm (I, J). **Threshold**, threshold-intensity procedure; **Zero-crossing**, zero-crossing procedure. The threshold level for the maximum intensity was set at 38%.

3.9 Analysis of VSVG passage through the GalT-compartment as the model to study intra-Golgi transport under 4Pi-microscopy

To determine how transmembrane secretory cargo transverse the Golgi complex (see **Introduction** for background), a transmembrane cargo protein and a Golgi-resident enzyme fused with fluorescent tags were co-expressed. Thereafter, by the use of two-colour 4Pi-microscopy recording (Khimich et al., 2005), and the deconvolution (Egner et al., 2004) and zero-crossing procedures (as set in the above correlative analyses), the passage of this cargo through the Golgi complex was recorded in 3D and in time.

In more detail, the VSVG and the *trans*-Golgi protein GalT (Roth and Berger, 1982) fused with the EGFP and venusYFP tags, respectively, were co-expressed in COS7 cells. Specifically, VSVG-pEGFP is a secretory cargo, as the G protein of the ts045 mutant of vesicular stomatitis virus (Gallione and Rose, 1985), and it can be accumulated in the ER at 40 °C and released into the secretory pathway in a synchronous pulse by shifting the temperature to 32 °C (Hirschberg et al., 1998). On the other hand, the correct localisation of endogenous GalT within the Golgi stack of cisternae is determined by its transmembrane domain, which has been used here instead of full-lenght GalT (Cole et al., 1996a; Egner et al., 2004).

Nonetheless, the *trans*-Golgi localisation of the GalT-venusYFP was also checked by immuno-TEM, as follows. COS7 cells were transfected for GalT-venusYFP and kept at 37 °C. Twenty-four hours later, the samples were fixed and processed for immuno-TEM, as was done previously for the BHK cells expressing PC3-pEGFP. As shown in **Figure 3.23**, the GalT transmembrane domain fused with the venusYFP tag has a sharp localisation in one or two *bona fide* Golgi *trans* cisternae (Cole et al., 1996a; Trucco et al., 2004). The structure of the nocodazole induced stacks was also examined. They usually comprised five to seven cisternae of up to 1

μm in length, and they were morphologically indistinguishable from ribbon-Golgi stacks, except for the lack of the tubular-vesicular non-compact zones connecting the stacks within the Golgi ribbon (see also Trucco et al., 2004).

As for the correlative analyses, the transport of VSVG-pEGFP was followed through single Golgi stacks of cisternae induced by treating these cells with 33 μM nocodazole for 3 h before the temperature shift. Moreover, at the same time as the cargo was released from the ER, 100 μg/ml cycloheximide was added to the medium, to reduce protein synthesis and the secretory load (Trucco et al., 2004). The cycloheximide treatment has previously been shown not to cause cell death, and it did not affect the ability of the cells to carry out VSVG transport (Trucco et al., 2004). Nevertheless, cell viability, cargo synchronisation efficacy, and the normal rate of VSVG-pEGFP transport under the experimental 4Pi-microscopy recording conditions (that require the sample to be mounted between two coverslips) was also checked. As shown in **Figure 3.24**, the co-transfected cells were treated with 33 μM nocodazole during the 3 h of accumulation at 40 °C and, subsequently, with 100 μg/ml cycloheximide (again with nocodazole) during cargo release. The temperature was thus shifted to 32 °C, and the samples were immediately mounted according to the 4Pi-microscopy requirements (i.e. between the two coverslips) without any fixative procedure. Under these conditions, the cells appeared to transport the VSVG-pEGFP to the PM, as was evident after 1 h of cargo release under conventional confocal microscopy (**Figure 3.24B**).

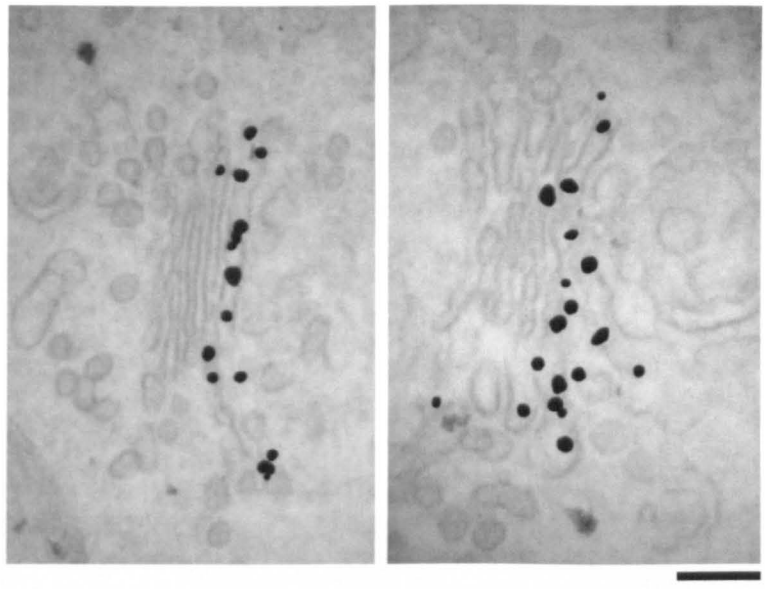

Figure 3.23. GalT–venusYFP immuno-TEM localisation in a Golgi stack of a COS7 cell.
The GalT-venusYFP clearly localises in one or two *bona fide trans* cisternae. Bar, 250 nm.

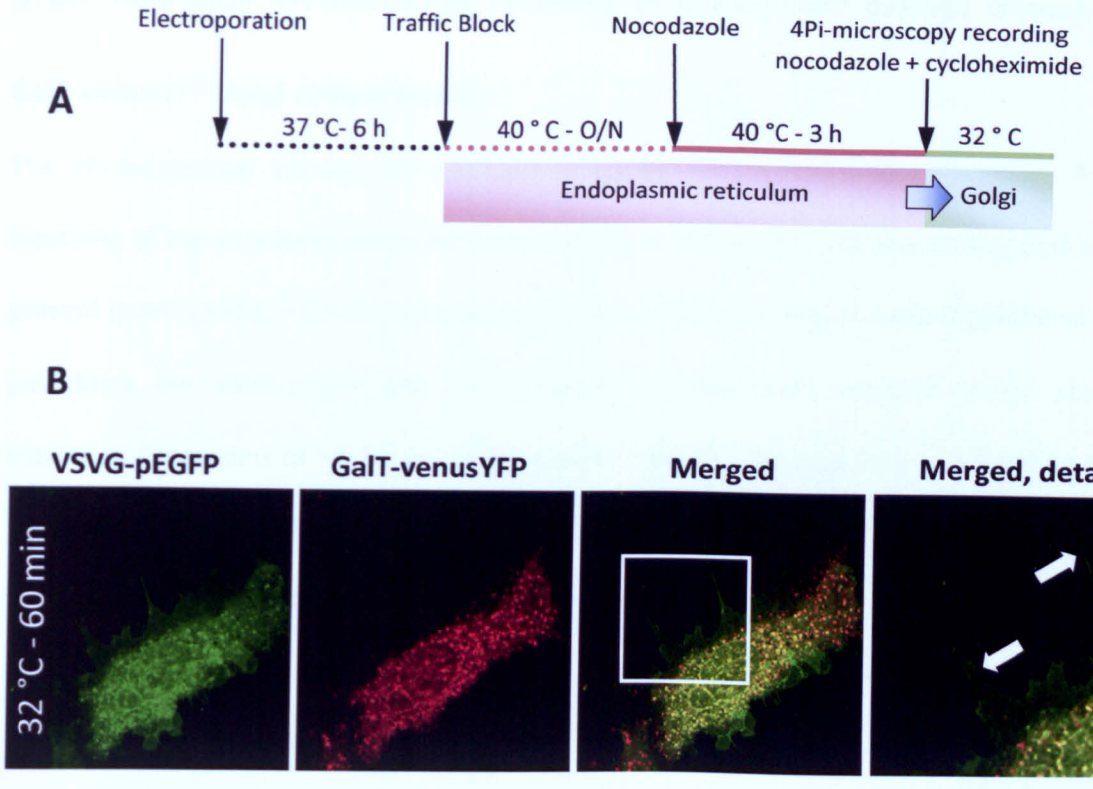

Figure 3.24. VSVG-pEGFP transport synchronisation in COS7 cells co-expressing GalT-venusYFP.

A, Synchronisation protocol for the VSVG-pEGFP transport used for the time-lapse 4Pi-microscopy recordings. **B**, The cells were treated as for the 4Pi-microscopy transport experiment and fixed after 1 h of VSVG-pEGFP (green) release (red, GalT-venusYFP). Once the transport is released, the VSVG-pEGFP enters the transport pathway and after 60 min of release at 32 °C, the arrival of VSVG-pEGFP at the plasma membrane is evident. The white box in B represents the field of view for the detailed merge panel. Confocal images, 63x magnification.

3.10 Time-lapse 4Pi-microscopy recording of VSVG-pEGFP passage through the GalT-venusYFP Golgi compartment

The 4Pi-microscopy allowed 3D recording of up to nine consecutive time points before bleaching of the structures precluded reliable imaging. Moreover, with the setting used in the present investigation, ~1.5 min was necessary for full 3D recording of a cell thickness of ~3.5 µm. Since the VSVG-pEGFP and GalT-venusYFP compartments analysed herein showed maximum dimensions of ~1-1.5 µm, they required ~30-40 s for recording. A total of 13 Golgi stacks from different cells were analysed, covering a range of ~4-30 min after the temperature shift. Among these Golgi stacks, seven were recorded within a unique cell over nine consecutive time points from ~6 to ~19 min of VSVG-pEGFP release. Two of these seven Golgi stacks (herein referred as Golgi stacks 5 and 6) are reported here as representative examples of the entrance and exit of the VSVG-pEGFP into the GalT-venusYFP compartment, respectively.

After the 4Pi-microscopy time-lapse recordings, the three-point deconvolution and zero-crossing-based segmentation were run, as was carried out for the 4Pi-CLEM analysis. Examples of the image segmentation (after deconvolution) of both the pEGFP and venusYFP signals are shown in **Figure 3.25**. The co-localisation of the two channels was also computed both as unweighted and weighted data. The former is computed on the segmented binary images (**Figure 3.25B**), the latter on the segmented 'intensity' images (**Figure 3.25C**). Subsequently, the 3D reconstructions of each compartment (**Figure 3.26A**, **B** and **Supplemental Videos 3.25** and **3.26**), and the merging with the co-localising compartments (**Figure 3.26C**, **D** and **Supplemental Videos 3.27** and **3.28**), were performed as detailed above. Finally, the centres of gravity (as defined in the Materials and Methods) for each of the signals were also computed and included in the 3D reconstructions, as shown in **Figure 3.26E** and **Supplemental Video 3.29**.

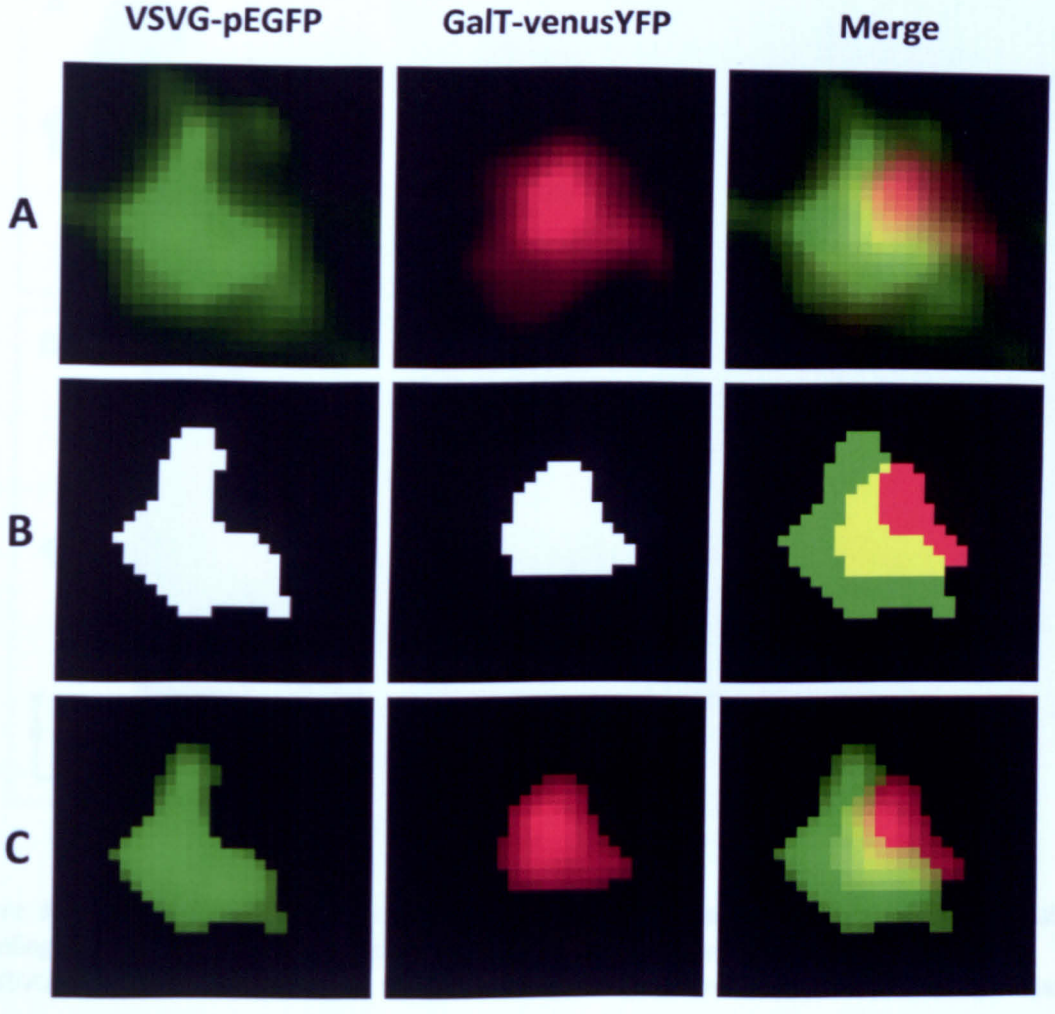

Figure 3.25. Application of the zero-crossing procedure to double labelling in living COS7 cells, as recorded under 4Pi-microscopy.

A, Three-point deconvolved image before segmentation; **B**, Segmented binary images showing the unweighted co-localisation area (yellow); **C**, Segmented intensity images with the weighted co-localisation (yellow) shown. Segmentation procedure included in the following order: 1) Gaussian smoothing, 2) initial thresholding, and 3) zero-crossing edge detection.

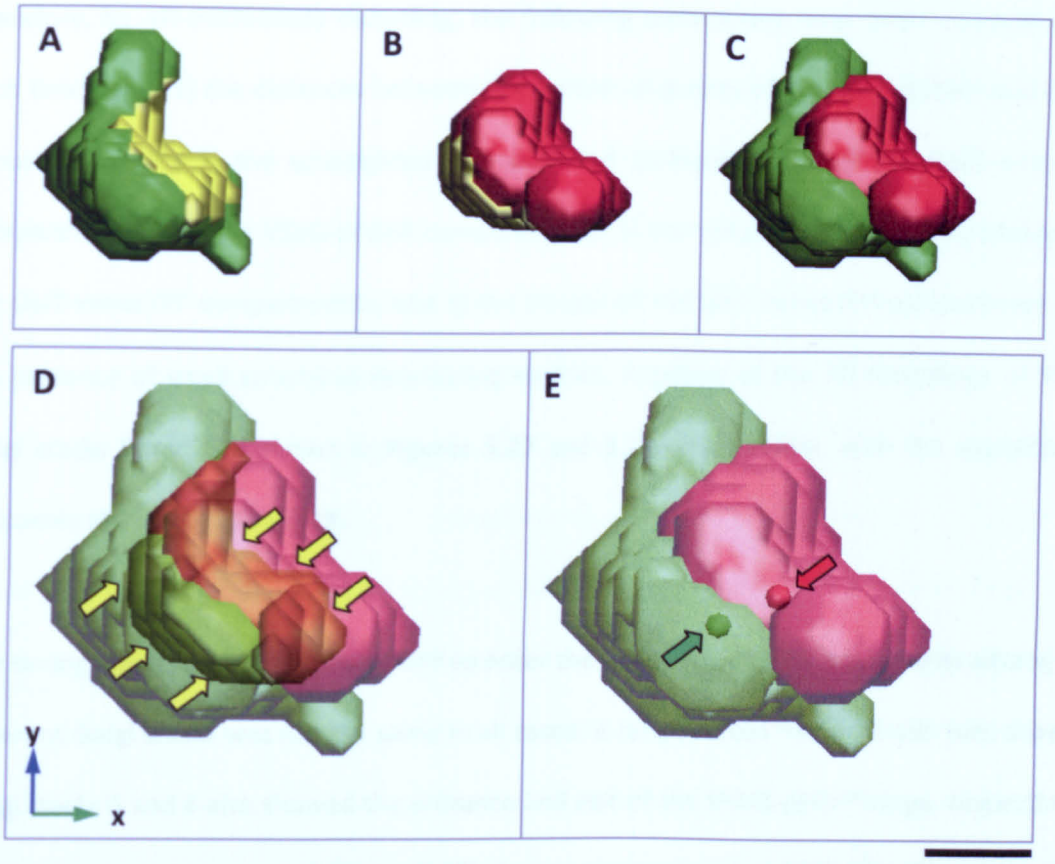

Figure 3.26. Three-dimensional reconstruction after zero-crossing segmentation for double labelling in living COS7 cells, as recorded under 4Pi-microscopy.

A, VSVG-pEGFP compartment; **B**, GalT-venusYFP compartment; **C**, VSVG-pEGFP and GalT-venusYFP merge (combined) compartments in the opaque mode; **D**, VSVG-pEGFP and GalT-venusYFP merge compartments in the transparent mode, showing the co-localising volumes (yellow arrows); **E**, VSVG-pEGFP and GalT-venusYFP merge compartments in the transparent mode, showing the centres of gravity (green and red arrows, respectively). Yellow surfaces in A and B represent the co-localising regions. This Golgi stack is the same as that of the **Figure 3.25**. Bar, 380 nm (A-C); 250 nm (D, E).

Therefore, by 4Pi-microscopy recording, the following parameters have been computed for each time-point: 1) the distances between the centres of gravity of the VSVG-pEGFP and GalT-venusYFP signals; 2) the unweighted and weighted co-localisations of the GalT-venusYFP compartments with the VSVG-pEGFP compartments; 3) the volumes and 4) the intensities of the GalT-venusYFP compartments; and 5) the shapes of the GalT-venusYFP compartment and the presence of small structures resembling vesicles. A gallery of the 3D recordings of these Golgi stacks 5 and 6 is shown in **Figures 3.27** and **3.28**, respectively, with the quantitative outcomes shown in **Figure 3.29**.

The timing required for the VSVG-pEGFP to enter the GalT-venusYFP compartments among the different Golgi stacks was not the same in all cases; it ranged from ~4 to ~8 min (not shown). Golgi stacks 5 and 6 also showed the entrance and exit of the VSVG-pEGFP cargo, respectively, within the same time interval (**Figure 3.29**). As a consequence, a quantitative mean behaviour for all of the Golgi stacks, i.e. the degree of co-localisation, cannot be computed. Here, an individual analysis is more appropriate, with the exception of the comparison between the unweighted and weighted co-localisations (see below).

As expected, as the VSVG-pEGFP bulk moves towards the GalT-venusYFP compartment, their centres of gravity become closer (Golgi stack 5, **Figure 3.29A**), and *vice versa* when VSVG-pEGFP leaves this compartment (Golgi stack 6, **Figure 3.29B**). The lowest distance between the two centres of gravity recorded across all of the 13 Golgi stacks and time points was 57 nm. The relationship seen between this parameter and the GalT-venusYFP compartment volume, which underwent changes during the passage of VSVG-pEGFP, is also of interest. In particular, as the distance between the centres of gravity dropped below ~130 nm (entrance of VSVG, Golgi stack 5, **Figure 3.29A**), the GalT-venusYFP volume increased, and *vice versa* (exit of VSVG, Golgi stack 6, **Figure 3.29B**). Moreover, although less clear, these volume changes appear to

also be related to the presence (rather than the degree) of co-localisation (**Figure 3.29**). Also of note, although the specific fluorescence intensities of the GalT-venusYFP compartments showed a rough inverse correlation with the corresponding volumes (**Figure 3.29**). This would indicate a dilution of the GalT-venusYFP as the VSVG-pEGFP arrived, and that the two compartments fused with each other, as was previously detected by immuno-TEM in actively transporting Golgi stacks for another *trans*-Golgi enzyme (Trucco et al., 2004).

The mean unweighted and weighted co-localisations of the GalT-venusYFP compartments with the VSVG-pEGFP compartments were also calculated at each time point for every Golgi stack, for comparison. However, to compare the two parameters, only the seven Golgi stacks from the same cell (and thus recorded at the very same time points) were included in this analysis. This thus overcomes the limits imposed by the non-synchronous entrance/exit of VSVG-pEGFP into/from the GalT-venusYFP compartments. Therefore, the comparison of the unweighted and weighted co-localisations was performed at each of these nine time points, and due to the high variability of the outcomes, non-parametric methods (Wilcoxon paired sing-rank test) were used to test the significance of their differences. Generally, the weighted co-localisation was greater as compared to the unweighted co-localisation, with the exception of the first and last time points (see median values, **Table 3.1**). Moreover, from 9.4 min to 15.9 min of VSVG-pEGFP release (six time points) the differences were statistically significant. These observations indicate that a differential distribution of the proteins (either cargoes or Golgi resident enzymes) may exist within the corresponding compartment, and thus for the best use of the co-localisation parameters weighting is required. A further reason for this diffrerences may reside in the concept that, even after the Gaussian smoothing and initial thresholding, some weak spourius signal could remain in the segmented image. Due to the weakness in the intensity of this residual signals, they may have an impact only in non-weighted co-localisations (i.e. on bynary image where the intensity information is lost), while the weighted

co-localisation would be less affected (see **Introduction, Section 1.2.b**). For this reason, the weighted co-localisation was used in the following observations.

An interesting and unexpected finding was the incomplete filling of the GalT-venusYFP compartments by the VSVG-pEGFP (i.e. partial co-localisation), which lasted for the entire process of its passage through the Golgi complex (**Figure 3.29**, and for all of the other Golgi stacks not shown). The median weighted co-localisation for the seven Golgi stacks ranged from 0.14 to 0.47, while individual Golgi stacks gave co-localisation values of between 0.00 and 0.78 (**Table 3.1**). Moreover, all of the 3D reconstructions (for all of the Golgi stacks and time points) of both the VSVG-pEGFP and GalT-venusYFP compartments were decomposed into their single 2D (XY) slices. This is shown in **Figure 3.30** (from Golgi stack 5, as recorded at 7.8 min after block release), which is representative of all of the recordings (compare **Figure 3.30** with the 3D reconstruction in **Figure 3.27**). This allowed an analysis of the patterns of the areas of co-localisation, which appear to have no preferential distributions on the GalT-venusYFP compartment, and in most of the cases, a unique overlapping area is seen per time point.

Appreciable changes in the shape of the GalT compartments were seen in all of the cases (see **Figures 3.27** and **3.28**), while small structures resembling peri-Golgi vesicles, either positive for VSVG-pEGFP or GalT-venusYFP, were not seen. However, the possibility that small 50-60-nm vesicles are close enough to the main compartments in a way to become indistinguishable at the 4Pi-microscopy level of resolution has to be taken into account.

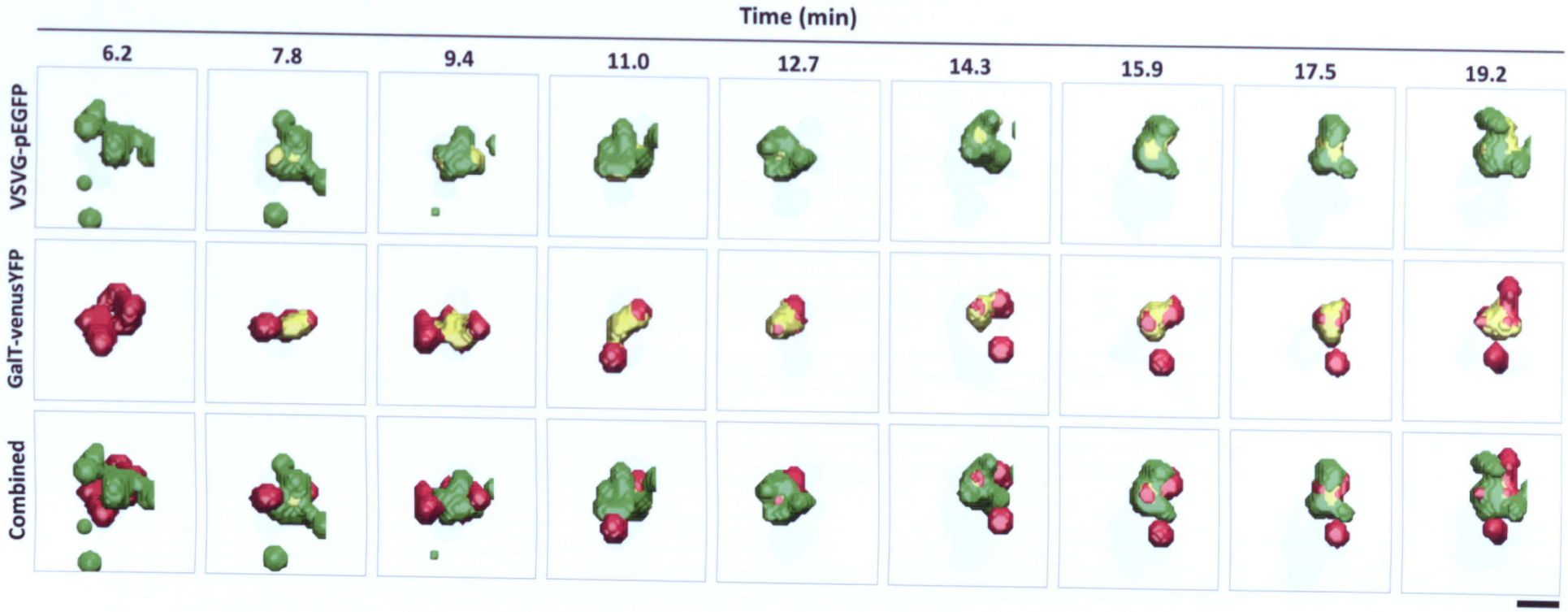

Figure 3.27. Time-lapse 4Pi-microscopy recordings of Golgi stack 5.
The 3D reconstructions and calculations, deconvolution and the zero-crossing segmentation procedures were carried out as reported in the correlative analysis. The entrance of the VSVG-pEGFP to the GalT-venusYFP compartment is shown. The time (in min) of the consecutive recordings is as indicated (6.2 to 19.2 min). **Green**, VSVG-pEGFP, **Red**, GalT-venusYFP, **Yellow**, co-localising areas. Bar, 300 nm.

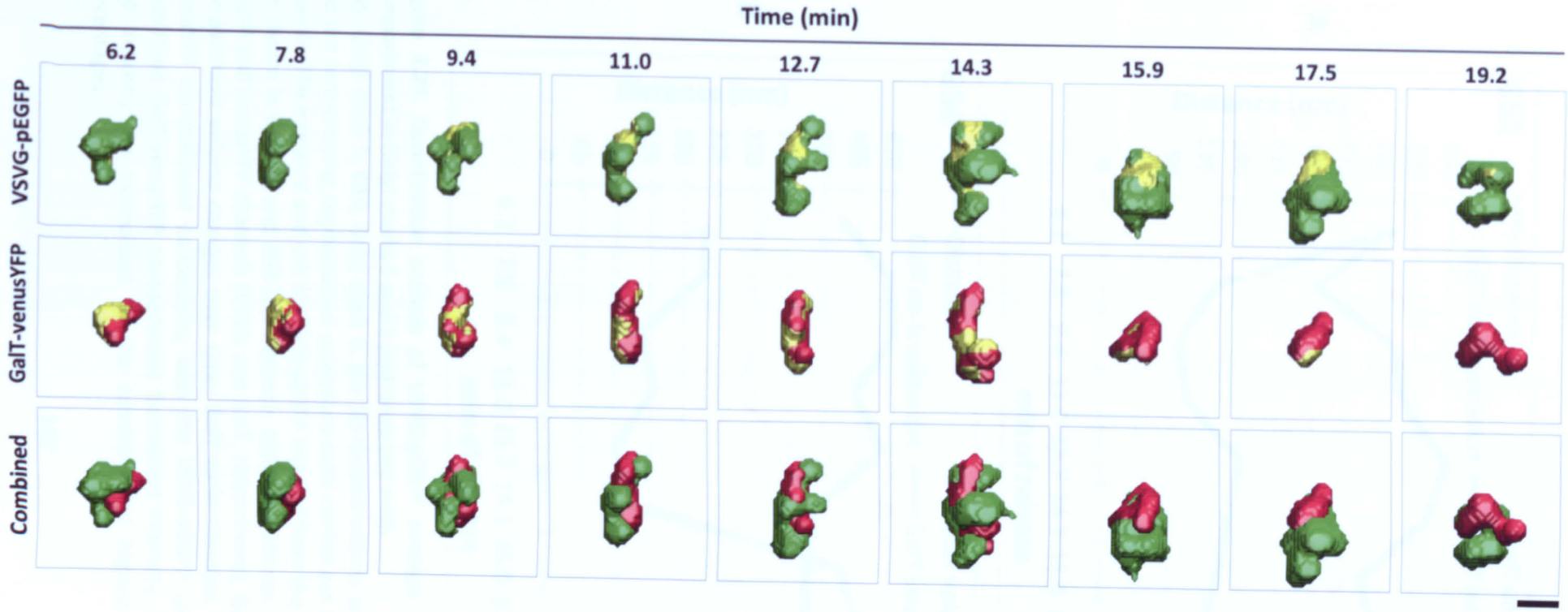

Figure 3.28. Time-lapse 4Pi-microscopy recordings of Golgi stack 6.
The 3D-reconstructions and calculations, deconvolution and the zero-crossing segmentation procedure were carried out as reported in the correlative analysis. The exit of the VSVG-pEGFP to the GalT-venusYFP compartment is shown. The time (in min) of the consecutive recordings is as indicated (6.2 to 19.2 min). **Green**, VSVG-pEGFP, **Red**, GalT-venusYFP, **Yellow**, colocalising areas. Bar, 300 nm.

A

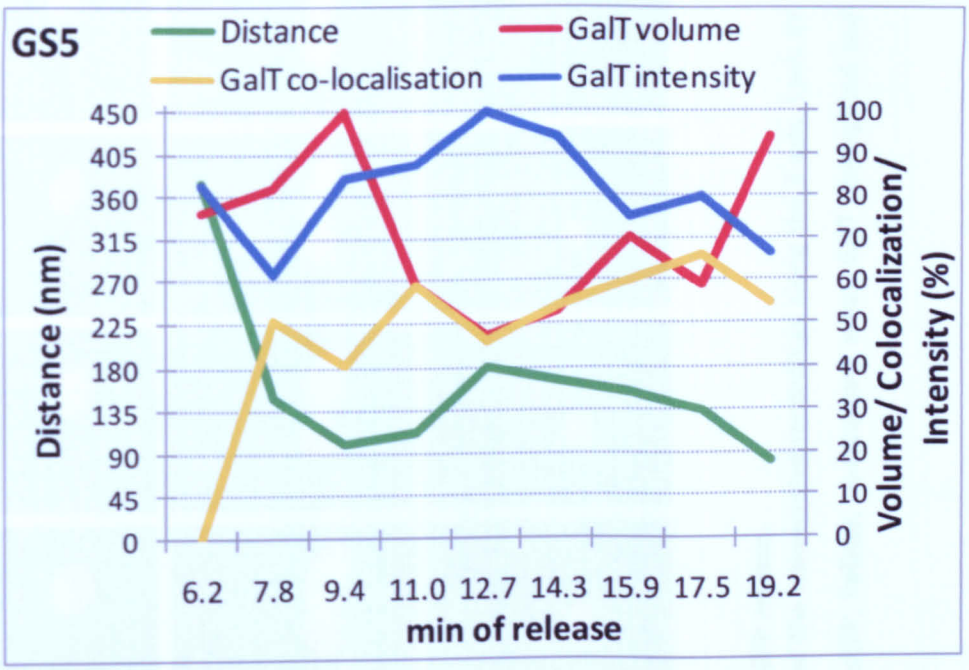

B

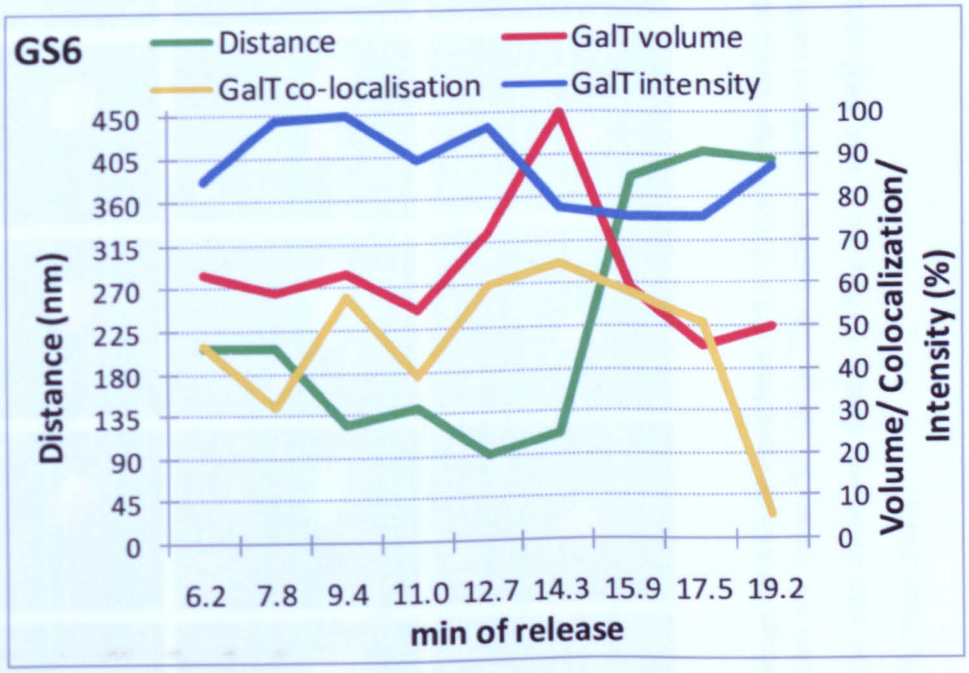

Figure 3.29. Quantitative analysis of VSVG-pEGFP passage through the GalT-venusYFP compartment in Golgi stacks 5 and 6 (entrance and exit).

GS5, Golgi stack 5; **GS6**, Golgi stack 6. the 3D-reconstructions and calculation, deconvolution and the zero-crossing segmentation procedure were carried out as reported in the correlative analysis. The entrance and exit of VSVG-pEGFP into and from the GalT-venusYFP compartment are shown in GS5 (**A**) and GS6 (**B**). **Distance**, distance between the centres of gravity of the pEGFP and venusYFP channels (VSVG and GalT, respectively); **GalT volume**, normalised GalT compartment volume changes over time; **GalT co-localisation**, normalised degree of GalT-venusYFP compartment co-localising with the VSVG-pEGFP compartment; **GalT intensity**, normalised GalT-venusYFP compartment fluorescent intensity. GalT volume, co-localisation and intensity are normalised to the corresponding highest values and presented as percentages.

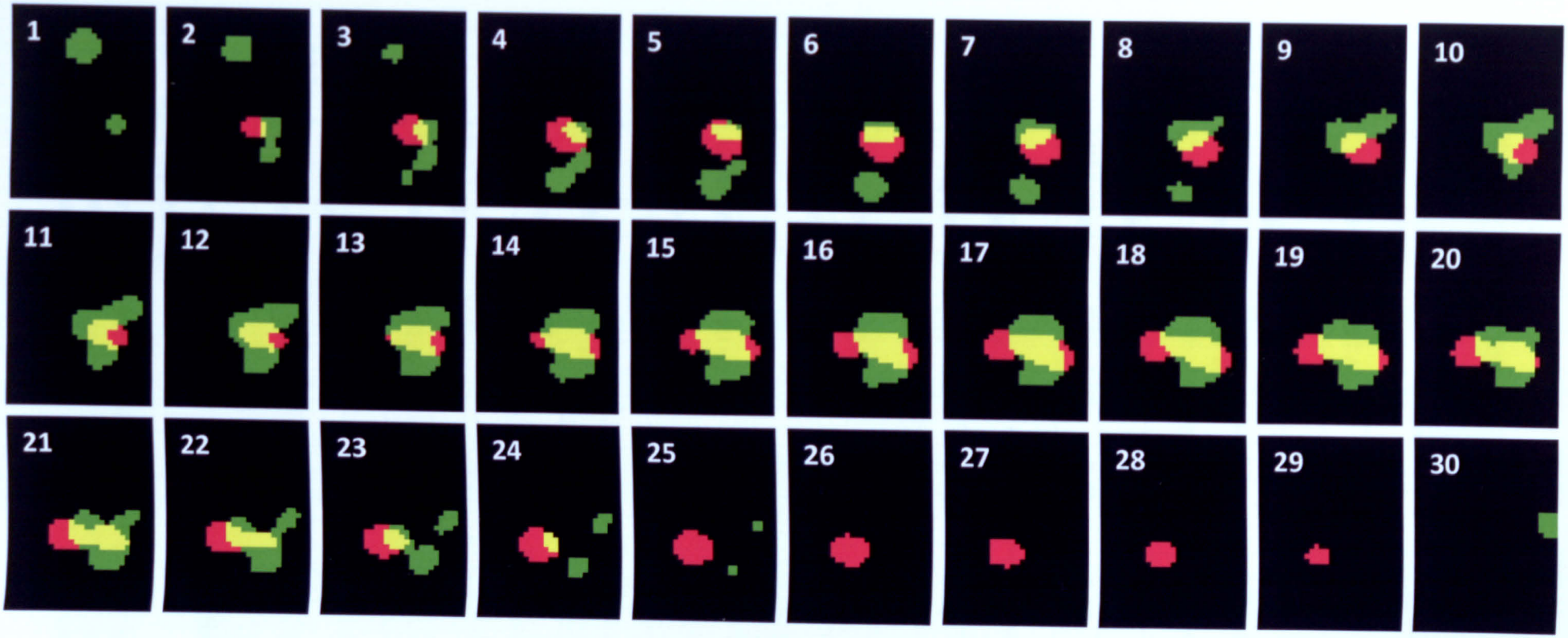

Figure 3.30. 4Pi-microscopy serial XY recordings for a Golgi stack from 5.0 at 7.8 min after VSVG-pEGFP release.
Binary images with unweighted co-localisation are shown for clarity. The numbers represent each of the consecutive recordings along the Z-axis. Each XY recording was 100 nm thick, and axially separated by 80 nm. **Green**, VSVG-pEGFP, **Red**, GalT-venusYFP, **Yellow**, co-localising areas. GalT unweighted and weighted co-localisations were 45% and 51%, respectively.

Time (min)	Weighting	Mean ±SE	Median	Minimum	Maximum	Difference
6.2	Unweighted	0.18 ±0.06	0.15	0	0.36	p =0.223; NS
	Weighted	0.27 ±0.11	0.14	0	0.70	
7.8	Unweighted	0.28 ±0.08	0.30	0	0.57	p =0.138; NS
	Weighted	0.34 ±0.10	0.34	0	0.78	
9.4	Unweighted	0.31 ±0.06	0.32	0.11	0.52	p =0.041; S
	Weighted	0.41 ±0.08	0.47	0.10	0.67	
11.0	Unweighted	0.32 ±0.05	0.33	0.15	0.51	p =0.028; S
	Weighted	0.41 ±0.07	0.41	0.18	0.70	
12.7	Unweighted	0.26 ±0.07	0.28	0.04	0.52	p =0.042; S
	Weighted	0.34±0.10	0.38	0.04	0.67	
14.3	Unweighted	0.29 ±0.06	0.34	0.09	0.55	p =0.028; S
	Weighted	0.38 ±0.08	0.42	0.11	0.65	
15.9	Unweighted	0.27 ±0.05	0.23	0.16	0.48	p =0.034; S
	Weighted	0.37 ±0.07	0.40	0.15	0.60	
17.5	Unweighted	0.36 ±0.07	0.29	0.07	0.61	p =0.108; NS
	Weighted	0.40 ±0.08	0.34	0.06	0.66	
19.2	Unweighted	0.26 ±0.05	0.29	0.05	0.48	p =0.753; NS
	Weighted	0.30 ±0.08	0.26	0.06	0.64	

Table 3.1. Weighted and unweighted co-localisations of the GalT-venusYFP and VSVG-pEGFP in time-lapse experiments.

Co-localisation data derived from all of the seven Golgi stacks (including Golgi stacks 5 and 6) recorded within the same cell over the different time points. SE, standard error of the mean; NS, difference not statistically significant; S, difference statistically significant.

Chapter 4. Discussion

The present study was aimed at testing the reliability of super-resolution fluorescence microscopy coupled with the intensity-independent zero-crossing segmentation procedure. This ultimately shows that 4Pi-microscopy can indeed be reliably applied to the recording of complex-shaped intracellular compartments. To accomplish this task, dedicated CLEM and 4Pi-CLEM techniques were used. Finally, as a biological application, the procedure was tested by the correlative analysis used to follow the passage of VSVG-pEGFP through the *trans*-Golgi complex, which was labelled with GalT-venusYFP, in a time-lapse manner. Through these experiments, the *trans*-Golgi complex has been recorded for the first time at unprecedented resolution under living conditions during the passage of cargo.

4.1 The zero-crossing procedure in confocal microscopy

The threshold procedure used in the 3D reconstructions of the endosomal/mitochondrial structures recorded under confocal microscopy provided less reliable results when compared to those from the zero-crossing procedure. Indeed, none of the different thresholding levels provided a structure that satisfactorily fitted the corresponding TEM data (**Figures 3.7** and **3.8**). This failure was probably due to the concept that the threshold intensity procedure forces the structure boundaries into an isosurface (see **Figure 1.12**). It is then likely that the fluorescence intensities at the true boundaries of the structures differ among the areas. For the same reason, the zero-crossing procedure that allows the boundaries to have a variable intensity (see **Figure 1.12**) appears to be more reliable. Moreover, also assuming that the standard threshold-intensity procedure may produce reliable 3D reconstructions, the problem of how to set the correct threshold cutting in every case still remains a crucial and open issue. The zero-crossing-based procedure has thus the noted advantage of being objective, while the

threshold-intensity procedure is set in a subjective manner. Of note, the different thresholding (from 10% to 30% of the maximum intensity) applied before the zero-crossing segmentation did not dramatically alter the reliability of the 3D reconstructions thus obtained (**Figures 3.7G-L, S-X** and **3.8G-L, S-X**). This is due to the relatively high positions of the inflection points (where the segmentation is set by the zero-crossing) on the PSF, as compared to those of the initial thresholding level (up to 30% of the maximum intensity). Therefore, while removing the background signals, the initial thresholding does not include the inflection points, and thus does not interfer with the zero-crossing procedure. This concept further illustrates the general applicability of this method when analysing bright and well-defined cellular compartments, such as mitochondria, endosomes and Golgi stacks. However, the usefulness of this procedure in the segmentation of structures with diffuse staining, characterised by a flatter PSF (i.e. ER), has still to be tested.

Therefore, this procedure promises to be a powerful method that can be extended to all types of fluorescence microscopy, for 3D as well as for 2D analysis. In addition to purely morphological studies, other quantitative analyses, i.e. co-localisation of two or three fluorescent markers, widely used in studying trafficking events, would also greatly benefit from this zero-crossing procedure, as it is objective and independent from the absolute and local intensity maxima. In time-lapse experiments under living-cell conditions, this procedure can also be expected to yield reconstructions that are less altered by the levels of progressive bleaching that can follow repeated measurements.

4.2 4Pi-CLEM analysis

As indicated above (see **Introduction**), the crucial determinant of the reliability in 4Pi-microscopy is represented by the optimal laser interference at the recorded object (Hell,

2003). This is accomplished when the refractive indices of the bodies (i.e. the two cellular sides) that the laser beams have to cross are the same (Blanca et al., 1998). However, these refractive indices are not controllable inside a cell (see **Introduction, Section 1.1.e**) and only 4Pi-CLEM analysis can reveal if the phase changes induced by their variations (including those between the aqueous medium and the cell interior) yield a space invariance of the PSF (Blanca et al., 1998; Egner et al., 1998) that may be deconvolved. Interestingly, we saw how this phenomenon does not significantly affect the reliability of 4Pi-microscopy. Indeed, even the use of water immersion lenses with lower aperture angle (leading to greater side lobes, see **Introduction, Section 1.1.e**), and the recording of structures in close proximity to the nucleus (as for Golgi stack 3) with a non-homogeneous distribution of refractive indices, do not alter significantly the phase relation between the focused illumination wave fronts, producing reliable outcomes in 3D analyses.

The use of correct linear three-point deconvolution (used herein for side lobe removal) followed by the zero-crossing procedure (after Gaussian smoothing and initial thresholding) were crucial steps for the obtaining of reliable imaging that can also be used for morphometric analyses (i.e. volume, co-localisation, etc.). Moreover, the reliability of the linear three-point deconvolution, which directly affects the validity of the resulting 3D structure, has been shown herein to be assessable by a visual comparison of the PSF before and after, neglecting the possibility of a structural alteration that was unnoticed by this procedure. A further interesting observation is related to the intensity of the side lobes. As mentioned above, as rule of thumb, this mathematical removal is possible if the side lobes are <50% of the main lobe (Lang et al., 2007). In the present study, the side lobes were in the range of 75% to 80% (**Figure 3.12**). In spite of this not being optimal, reliable 3D reconstructions in Golgi stacks 1 and 3 were still obtained (**Figures 3.19** and **3.21**). Interestingly, the space invariance of the PSF through the Z-axis was seen to be a strong indicator of the reliability of the final outcome, as seen for Golgi

stack 4, which lacked this important feature (**Figure 3.22**). Overall, these results are very encouraging, and taken together, all of these observations suggest that the final outcome can be predictable when an accurate analysis of the side lobes and deconvolution is made.

However, the intensity of the side lobes has to be kept to a minimum if an increase of the reliability of the 4Pi-microscopy is desired. To solve this problem, two side lobe-suppression mechanisms were introduced in the prototype used in the present investigation: 1) confocal detection (Hell and Stelzer, 1992b); and 2) two-photon excitation (Hell and Stelzer, 1992a) (see also **Introduction, Section 1.1.e**). Therefore, abandoning confocal detection or two-photon excitation would probably compromise the practicability of this interference-based technique when cells are immersed in an aqueous medium. However, the limitations of the multi-photon strategy are that it usually requires expensive mode-locked lasers and that it is usually accompanied by stronger bleaching within the in-focus plane. The last limitation is particularly important in time-lapse experiments, were the same structure has to be recorded continuously over time. In such experiments, careful adjustment of the excitation intensity by the use of transmission filters reduced bleaching in consecutive image stacks to an average of only 10%. In the case of other cargoes, such as VSVG-pEGFP, up to nine consecutive recordings could still be made with a satisfactory signal-to-noise ratio (see **Results, Section 3.10**).

Promising achievements will probably come with the advent of a new 4Pi-microscopy configuration, with one-photon excitation (Lang et al., 2007) and/or simultaneous coherent addition of the illumination and fluorescence wavefronts both at the object and detector levels (Type C 4Pi-microscopy) (see **Introduction, Section 1.1.e**).

The zero-crossing segmentation procedure was tested successfully here for the 3D reconstructions of two of the four Golgi stacks (Golgi stacks 1 and 3, with favourable PSF and

deconvolution features [see **Results, Section 3.5**]). This further shows that zero-crossing segmentation can be used to overcome the limits of structural uncertainties that are introduced by the standard threshold-intensity procedure. Despite the zero-crossing procedure being a powerful method that has had widespread application in spectrometry and fluorescence spectrophotometry (O'Haver, 1979), to date, this procedure has seen only very limited use in microscopy (Raman et al., 2007). Indeed, no previous studies have investigated the reliability of this procedure in depth and the present investigation is the first using a correlative analysis to evaluate the reliability of a segmentation procedure. Thus, the present study has demonstrated the reliability of the zero-crossing procedure, if applied after a proper smoothing and an initial thresholding (see **Introduction, Section 1.2.b**). We would propose to extend the application of this procedure to all fluorescence microscopy techniques.

The reconstructed structures using zero-crossing generally lead to greater correlations with the TEM-derived structures, which is also reflected in the higher Manders coefficients (**Figure 3.17A, B**). The standard threshold-intensity procedure predicts that the whole surface of the 3D reconstructed structure has the same intensity (see **Introduction, Section 1.2.b**), a condition that may not fit with reality, and especially for larger organelles, such as for Golgi stack 3, with its complex structural organisation. On the other hand, in the case of the simpler and smaller Golgi stack 1, the thresholding was also satisfactorily accurate, although it must be noted that the threshold values were set *a posteriori*, following the computing of the overlap with the TEM-derived structures. Moreover, in the present case, the standard threshold-intensity procedure can induce further errors, as the distribution of the fluorescent tag is fitted to a TEM structure that does not contain any information about the protein concentration or distribution. The differences among the threshold-intensity values computed for the four Golgi stack reconstructions here also clearly show the poor repeatability of this fixed-threshold segmentation. This limitation is of particular importance when there is the need for objective

segmenting of multiple structural elements in one image, or of objects with a highly complex intensity distribution. An unreliable method of image segmentation can only lead to false structures, and the benefit of increased resolution present in the raw data (as in 4Pi-microscopy) will not be fully conserved in the final image. Therefore, what is a basic need in conventional confocal microscopy becomes an issue of tremendous importance in super-resolved fluorescent imaging techniques.

Through this comparative analysis of the structures provided by 4Pi-CLEM and TEM-based CLEM, we have also shown that the combination of super-resolution microscopy with this objective, intensity-independent, zero-crossing image segmentation technique provides a tool for investigations into highly resolved organelle structures that has unprecedented power. Importantly, this technique can now also be combined with the potential for working under living-cell conditions. Indeed, even though the viability of the recorded cells was questioned by the fact that 4Pi-microscopy requires the sample to be mounted between two coverslips (**Figure 1.4**), our transport experiments showed that the cells can maintain VSVG-pEGFP transport up to 1 h (**Figure 3.24B**) without detectable differences from a control sample. Moreover, appropriate sample chambers with optimal air and CO_2 conditions that allow further cell viability (up to 48 h) have recently been successfully used in combination with 4Pi-microscopy (Egner et al., 2004).

The present results, along with previous observations (Egner et al., 2004; Medda et al., 2006), show that 4Pi-microscopy can be applied with reasonable reliability when optical conditions are far from being perfect. Two-photon 4Pi-microscopy with its robust PSF proves to be especially applicable to living-cell imaging (Egner et al., 2004; Medda et al., 2006). Even though, at least until very recently, 4Pi-microscopes have been relatively difficult to operate, this limitation has been overcome by the development of a compact commercial 4Pi-

microscope (Leica TCS 4Pi, Mannheim, Germany) (Medda et al., 2006) (see **Introduction, section 1.1.e**), making its standard operation in biological research on a daily basis now possible.

Any cellular structures with details of interest in the range of 100-500 nm, thus below the limit of confocal axial resolution (Pawley, 2006), can benefit from applying this method. Currently, one to two seconds per image slice are needed, making 3D recordings of small structures available in steps of one or two min.

4.3 Intra-Golgi transport as revealed by 4Pi-microscopy

The mechanisms by which cargoes transverse the Golgi complex are still controversial (Mironov et al., 2005). Indeed, several models have been proposed, including: 1) the vesicular-shuttle model (Palade, 1975); 2) the cisternal progression/maturation model, in its different variants (Bonfanti et al., 1998; Losev et al., 2006; Matsuura-Tokita et al., 2006; Trucco et al., 2004); 3) the carrier progression/maturation model (Mironov et al., 2005; White et al., 2001); 4) the cargo flow via continuities model (Marsh et al., 2004; Mironov et al., 2005; Rambourg et al., 1993); and 5) the partitioning within a two-phase membrane system (Patterson et al., 2008) (see **Introduction**). The reasons for these inconsistencies derive from the concept that most of the results have been derived indirectly, i.e. by TEM analysis, with only few studies based on living cells (Losev et al., 2006; Matsuura-Tokita et al., 2006; Patterson et al., 2008; White et al., 2001). Unfortunately, even these living-cell-based studies have provided contrasting results, as they have been seen to be in favour of the cisternal maturation model (Losev et al., 2006; Matsuura-Tokita et al., 2006) or to predict the cisternae as stable compartments (Patterson et al., 2008; White et al., 2001).

In the present investigation, nocodazole-induced Golgi stacks were selected for 4Pi-microscopy. This was due to the concept that isolated Golgi stacks represent a simple and reliable model to investigate intra-Golgi transport (Trucco et al., 2004), and also that their relatively small size allows substantial gain in speed of signal acquisition, which also results in a reduction in specimen bleaching.

The rapid entrance and exit of cargo through the GalT-venusYFP compartments seen herein fits with the data from a recent *in-vivo* investigation (Patterson et al., 2008) in which a similar protocol was used to show transmembrane cargo molecules entering the Golgi and being quickly distributed throughout the system, before their differentially partitioning between two different membrane environments. Although the present 4Pi-microscopy recordings do not allow a full kinetic analysis, the mode of exit of the VSVG-PEGFP from Golgi stack 6 (**Figures 3.28** and **3.29B**, last 2 time points) appears to be rapid, in the range of ~1-2 min. This rapid exit might fit the view of the exponential kinetics of exit of the cargo from the Golgi that was proposed recently (Patterson et al., 2008). In contrast, the linear exit of the cargo from the Golgi complex, as would be expected for the cisternal progression/maturation model, would last significantly longer than 2 min (Patterson et al., 2008; Trucco et al., 2004). However, the different protocols used in the VSVG synchronisation could also explain apparent inconsistencies in the present findings and those previously reported by immune-TEM by Trucco et al. (2004). Indeed, the 15 °C temperature used to block the cargo at the IC level could be responsible for the different export kinetics from the Golgi complex. In particular, previous simulation and experimental testing has shown a gradient in the SL/GPL composition, with the lowest and highest ratios in the *cis* and *trans* cisterna, respectively (Patterson et al., 2008). Resident proteins with different SL/GPL preferences can be enriched in different cisternae within the Golgi despite the continuous circulation of processing enzymes and cargo up and down the stack. Finally, these simulations have revealed a cargo wave pattern across the Golgi

stack in response to the short 15 °C temperature block and release of membrane trafficking, which is consistent with that observed in immuno-TEM experiments (Trucco et al., 2004).

The unexpected incomplete cargo-Golgi enzyme co-localisation seen in the present investigation fits with previous reports (Patterson et al., 2008; White et al., 2001). Interestingly, the segregation of the cargo and Golgi enzymes has been explained by the formation of a cargo domain, which would remain connected with the Golgi complex to allow the correct biochemical reactions to take place. However, these previous investigation were based on conventional 2D confocal microscopy, the resolution limits of which hampered their full quantification of the degree of co-localisation. This has left open other important issues, such as the real spatial relationships between the Golgi and the cargo domains (i.e. side-by-side segregation), and the eventual volume changes in the GalT-venusYFP compartment. The present study instead has shown how although the GalT-venusYFP compartment remains segregated from the VSVG-PEGFP compartment, it reversibly increases in volume upon the arrival of cargo (**Figure 3.29**). This increase can be explained by the arrival of membranes following the temperature shift to 32 °C. Interestingly, a previous TEM analysis showed an increase in length and number of Golgi cisternae upon the arrival of cargo (Trucco et al., 2004). It is then hypothesised that the overlapping region is composed mainly of membranes derived from the cargo compartment, and that the Golgi-resident enzymes diffuse to this area of intermixing to allow the necessary biochemical reactions.

Also of note, the present study does not show the side-by-side type of segregation of the VSVG-pEGFP compartment with respect to the GalT-venusYFP compartment that has been described in previous studies (Patterson et al., 2008; White et al., 2001). Indeed, a random spatial relationship was seen between these two compartments (sometimes with one compartment in the apparent centre of the other, **Figure 3.30**), which would fit better with the

immuno-TEM data showing that cargo labelling can be found throughout the Golgi cisternae (Bonfanti et al., 1998; Trucco et al., 2004), and which is less easy to reconcile with the idea that the cargo domain corresponds to an exit compartment, as proposed by (Patterson et al., 2008). Future investigations on the machinery responsible for this a segregation are warranted.

The role and content of peri-Golgi vesicles is another aspect that remains controversial (for reviews, see Bethune et al., 2006; Kartberg et al., 2005), with some evidence seen for the absence of both anterograde cargoes (Martinez-Menarguez et al., 2001) and Golgi-resident enzymes (Orci et al., 2000; Trucco et al., 2004) within such vesicles. In the present study, structures resembling small vesicles that were positive for either VSVG-PEGFP or GalT-venusYFP were not seen (see **Figures 3.27** and **3.28**). However, since our 4Pi-microscopy settings would only detect vesicles further than 100-150 nm from the rims of the cisternae (Hell, 2003), these data simply indicate that enzyme- or cargo-containing vesicles cannot be detected beyond this distance during trafficking.

Finally, besides the limitations discussed above, several advantages of the 4Pi-microscopy over other established methods for the investigation of the living Golgi can be considered. For instance, 4Pi-microscopy has revealed some details of Golgi dynamics upon the arrival of cargo (such as the enlargement of GalT-venusYFP compartment) that could be appreciated in the past only by immuno-TEM (Trucco et al., 2004). On the other hand, we see here that in contrast to TEM, 4Pi-microscopy can be successfully used in living cells. This has provided a high resolution tool to investigate transport through individual Golgi stacks. Under certain circumstances, this feature of 4Pi-microscopy will be especially important, such as for observation that different Golgi stacks do not received material from the ER simultaneously (see **Results**). In this case, methods based on the evaluation of the average parameters for the

entire Golgi stack population (as with immuno-TEM) might well provide biased conclusions for the kinetics of VSVG-pEGFP progression through the stack.

4.4 Conclusion

For the first time, and as representative for the full range of new super-resolution fluorescent microscopy techniques, 4Pi-microscopy has been pushed to the limit of its spatial resolution to show that it is a powerful enough technique to image substructures of trafficking organelles in 3D. The present study is thus the first to precisely characterise to what extent the domains of applicability of light and electron microscopy overlap. Moreover, when combined with the intensity-independent, zero-crossing-based segmentation procedure, accurate 3D reconstructions can now be produced.

As a result, we have shown that 4Pi-microscopy provides a fast, easy to use, and reliable tool for the study of the 3D organelle morphology in living cells. This includes here the passage of a cargo through to the *trans*-Golgi under living conditions at unprecedented resolution limits, which are still not attainable by other fluorescence light microscopy techniques. We would therefore propose this 4Pi-microscopy technology as a new and powerful tool for the study of intracellular trafficking events when coupled with the application of the zero-crossing procedure as the image segmentation procedure. Of note, the reliability of this zero-crossing technique should also now be further investigated across all uses of fluorescence microscopy. These results will thus contribute to the advent of the new era of super-resolution light microscopy or "nanoscopy".

List of abbreviations

2D	Bi-dimensional
3D	Three-dimensional
α	Aperture angle
λ	Wavelength
μM	Micromolar
σ	Gaussian sigma
ATP	Adenosine triphosphate
avi	Audio video interleave
bit	Byte
BHK	Baby hamster kidney cells
BSA	Bovine serum albumin
CGN	*Cis*-Golgi network
CLEM	Correlative light-electron microscopy
CCD	Charge coupled device
COPI	Coat protein I
COS7	African green monkey cells
$cPLA_2\varepsilon$	Cytosolic phospholipase A_2 ε
dbl	Double binary
DIC	Differential interference contrast
DMEM	Dulbecco's modified Eagle's medium
DNA	Deoxyribonucleic acid
dpi	Dots per inch
dx	Explorer
EDTA	Ethylenediamine tetracetic acid
EGFP	Enhanced green fluorescent protein
ER	Endoplasmic reticulum
FCS	Foetal calf serum
FPALM	Fluorescence photoactivation localisation microscopy
FWHM	Full width at half maximum
GalT	β-1,4-galactosyltransferase
GalT-venusYFP	β-1,4-galactosyltransferase-venus yellow fluorescent protein
GlcNAc	N-acetylglucosamine
GM130	Golgi matrix protein 130 kDa

GPLs	Glycerophospholipids
GSH	Glutathione
h	Hour
HEPES	N-2-hydroxyethylpiperazine-N-2-ethanasulfonic acid
I^5M	Interference microscopy
IC	Intermediate compartment
IP	Inflection point
LB	Luria Broth
lif	Leica image file format
lsm	Laser scanning microscopy
min	Minutes
Mito-pEGFP	Mito-enanched green fluorescent protein
ml	Milliliter
mM	Millimolar
msr	ImSpector measurement
n	Refractive index
nM	Nanomolar
O/N	Overnight
PALM	Photoactivated localisation microscopy
PALMIRA	PALM with independently running acquisition
PBS	Phosphate buffered saline
PC	Phosphatidylcholine
PC3-pEFGP	Procollagen-3-enhanched green fluorescent protein
PCI	Procollagen I
pEGFP	Enhanched green fluorescent protein plasmid
Pixel	Picture element
PM	Plasma membrane
PSF	Point spread function
RGB	Red - green - blue
RESOLFT	Reversible saturable optical (fluorescence) transitions
RT	Room temperature
SE	Standard error of the mean
SEM	Scanning electron microscopy
SL	Sphingolipid
SNP	Signal-to-noise ratio

spe	Winspec files
ss-YFP	Signal sequence peptide-yellow fluorescent protein
STED	Stimulated emission depletion microscopy
STORM	Stochastic optical reconstruction microscopy
TE	Tris(hydroxymethyl)aminomethane-ethylene di-amine tetracetic acid
TEM	Transmission electron microscopy
TGN	*Trans*-Golgi network
TGN38	TGN protein 38 kDa
tiff	Tagged image file format
TrisHCl	tris(hydroxymethyl)aminomethane-hydrocloric acid
Venus-YFP	Venus yellow fluorescent protein
VMD	Visual molecular dynamics
Voxel	Volume element
VSVG-pEGFP	Vescicular stomatitis virus G protein-enhanced green fluorescent protein

Supplemental Video Legends

Supplemental Video 3.1. The 3D overlap of the confocal-microscopy reconstruction made by the zero-crossing procedure, after 30% of initial thresholding (opaque), and the TEM recordings for the endosomal structures.

Supplemental Video 3.2. The 3D overlap of the confocal-microscopy reconstruction made by the zero-crossing procedure, after 30% of initial thresholding (transparent), and the TEM recordings for the endosomal structures.

Supplemental Video 3.3. The 3D overlap of the confocal-microscopy reconstruction made by the zero-crossing procedure, after 30% of initial thresholding (opaque), and the TEM recordings for the mitochondrial structures.

Supplemental Video 3.4. The 3D overlap of the confocal-microscopy reconstruction made by the zero-crossing procedure, after 30% of initial thresholding (transparent), and the TEM recordings for the mitochondrial structures.

Supplemental Video 3.5. The TEM 3D reconstruction of Golgi stack 1.Each colour represents a single Golgi cisternae or carrier.

Supplemental Video 3.6. The TEM 3D reconstruction of Golgi stack 2.Each colour represents a single Golgi cisternae or carrier.

Supplemental Video 3.7. The TEM 3D reconstruction of Golgi stack 3.Each colour represents a single Golgi cisternae or carrier.

Supplemental Video 3.8. The TEM 3D reconstruction of Golgi stack 4.Each colour represents a single Golgi cisternae or carrier.

Supplemental Video 3.9. The 3D overlap of the 4Pi-microscopy reconstruction made by threshold-intensity procedure (opaque) and the TEM recordings for Golgi stack 1.

Supplemental Video 3.10. The 3D overlap of the 4Pi-microscopy reconstruction made by the threshold-intensity procedure (transparent) and the TEM recordings for Golgi stack 1.

Supplemental Video 11. The 3D overlap of the 4Pi-microscopy reconstruction made by the zero-crossing procedure (opaque) and the TEM recordings for Golgi stack 1.

Supplemental Video 12. The 3D overlap of the 4Pi-microscopy reconstruction made by the zero-crossing procedure (transparent) and the TEM recordings for Golgi stack 1.

Supplemental Video 13. The 3D overlap of the 4Pi-microscopy reconstruction made by threshold-intensity procedure (opaque) and the TEM recordings for Golgi stack 2.

Supplemental Video 3.14. The 3D overlap of the 4Pi-microscopy reconstruction made by the threshold-intensity procedure (transparent) and the TEM recordings for Golgi stack 2.

Supplemental Video 3.15. The 3D overlap of the 4Pi-microscopy reconstruction made by the zero-crossing procedure (opaque) and the TEM recordings for Golgi stack 2.

Supplemental Video 3.16. The 3D overlap of the 4Pi-microscopy reconstruction made by the zero-crossing procedure (transparent) and the TEM recordings for Golgi stack 2.

Supplemental Video 3.17. The 3D overlap of the 4Pi-microscopy reconstruction made by threshold-intensity procedure (opaque) and the TEM recordings for Golgi stack 3.

Supplemental Video 3.18. The 3D overlap of the 4Pi-microscopy reconstruction made by the threshold-intensity procedure (transparent) and the TEM recordings for Golgi stack 3.

Supplemental Video 3.19. The 3D overlap of the 4Pi-microscopy reconstruction made by the zero-crossing procedure (opaque) and the TEM recordings for Golgi stack 3.

Supplemental Video 3.20. The 3D overlap of the 4Pi-microscopy reconstruction made by the zero-crossing procedure (transparent) and the TEM recordings for Golgi stack 3.

Supplemental Video 3.21. The 3D overlap of the 4Pi-microscopy reconstruction made by threshold-intensity procedure (opaque) and the TEM recordings for Golgi stack 4.

Supplemental Video 3.22. The 3D overlap of the 4Pi-microscopy reconstruction made by the threshold-intensity procedure (transparent) and the TEM recordings for Golgi stack 4.

Supplemental Video 3.23. The 3D overlap of the 4Pi-microscopy reconstruction made by the zero-crossing procedure (opaque) and the TEM recordings for Golgi stack 4.

Supplemental Video 3.24. The 3D overlap of the 4Pi-microscopy reconstruction made by the zero-crossing procedure (transparent) and the TEM recordings for Golgi stack 4.

Supplemental Video 3.25. The 4Pi-microscopy 3D reconstruction of the VSVG-pEGFP compartment in living COS7 cell made by the zero-crossing procedure (opaque). Yellow surfaces represents the co-localising regions.

Supplemental Video 3.26. The 4Pi-microscopy 3D reconstruction of the GalT-venusYFP compartment in living COS7 cell made by the zero-crossing procedure (opaque). Yellow surfaces represents the co-localising regions.

Supplemental Video 3.27. The 4Pi-microscopy 3D reconstruction of the VSVG-pEGFP and GalT-venusYFP combined compartments in living a COS7 cell made by the zero-crossing procedure (opaque).

Supplemental Video 3.28. The 4Pi-microscopy 3D reconstruction of the VSVG-pEGFP and GalT-venusYFP combined compartments *in living a COS7 cell made by the zero-crossing procedure* (transparent). The co-localising volumes (opaque) are in yellow.

Supplemental Video 3.28. The 4Pi-microscopy 3D reconstruction of the VSVG-pEGFP and GalT-venusYFP combined compartments in living a COS7 cell made by the zero-crossing procedure (transparent). The centres of gravity (opaque) are in green and red, respectively.

References

Abbe E. Beitrœege zur Theorie des Mikroskops und der mikroskopischenWahrnehmung. Arch f Mikroskop Anat 1873;9:413-420.

Bachinger H.P., Morris N.P., Davis J.M. Thermal stability and folding of the collagen triple helix and the effects of mutations in osteogenesis imperfecta on the triple helix of type I collagen. Am J Med Genet 1993;45:152-162.

Balch W.E., Dunphy W.G., Braell W.A., Rothman J.E. Reconstitution of the transport of protein between successive compartments of the Golgi measured by the coupled incorporation of N-acetylglucosamine. Cell 1984;39:405-416.

Bannykh S.I., Balch W.E. Membrane dynamics at the endoplasmic reticulum-Golgi interface. J Cell Biol 1997;138:1-4.

Barr F.A., Short B. Golgins in the structure and dynamics of the Golgi apparatus. Curr Opin Cell Biol 2003;15:405-413.

Beck K., Boswell B.A., Ridgway C.C., Bachinger H.P. Triple helix formation of procollagen type I can occur at the rough endoplasmic reticulum membrane. J Biol Chem 1996;271:21566-21573.

Bethune J., Wieland F., Moelleken J. COPI-mediated transport. J Membr Biol 2006;211:65-79.

Betzig E., Patterson G.H., Sougrat R., Lindwasser O.W., Olenych S., Bonifacino J.S., Davidson M.W., Lippincott-Schwartz J., Hess H.F. Imaging intracellular fluorescent proteins at nanometer resolution. Science 2006;313:1642-1645.

Blanca C.M., Bewersdorf J., Hell S.W. Determination of the unknown phase difference in 4Pi-confocal microscopy through the image intensity Opt Commun 1998;206:281-285.

Bolte S., Cordelières F.P. A guided tour into subcellular colocalization analysis in light microscopy. J Microsc 2006;224:213-232.

Bonfanti L., Mironov A.A., Jr., Martinez-Menarguez J.A., Martella O., Fusella A., Baldassarre M., Buccione R., Geuze H.J., Mironov A.A., Luini A. Procollagen traverses the Golgi stack without leaving the lumen of cisternae: evidence for cisternal maturation. Cell 1998;95:993-1003.

Bruckner P., Eikenberry E.F. Procollagen is more stable in cellulo than in vitro. Eur J Biochem 1984;140:397-399.

Clermont Y., Rambourg A., Hermo L. Connections between the various elements of the cis- and mid-compartments of the Golgi apparatus of early rat spermatids. Anat Rec 1994;240:469-480.

Cole N.B., Sciaky N., Marotta A., Song J., Lippincott-Schwartz J. Golgi dispersal during microtubule disruption: regeneration of Golgi stacks at peripheral endoplasmic reticulum exit sites. Mol Biol Cell 1996a;7:631-650.

Cole N.B., Smith C.L., Sciaky N., Terasaki M., Edidin M., Lippincott-Schwartz J. Diffusional mobility of Golgi proteins in membranes of living cells. Science 1996b;273:797-801.

Costes S.V., Daelemans D., Cho E.H., Dobbin Z., Pavlakis G., Lockett S. Automatic and quantitative measurement of protein-protein colocalization in live cells. Biophys J 2004;86:3993-4003.

Dahan S., Ahluwalia J.P., Wong L., Posner B.I., Bergeron J.J. Concentration of intracellular hepatic apolipoprotein E in Golgi apparatus saccular distensions and endosomes. J Cell Biol 1994;127:1859-1869.

Dalton A.J., Felix M.D. Cytologic and cytochemical characteristics of the Golgi substance of epithelial cells of the epididymis in situ, in homogenates and after isolation. Am J Anat 1954;94:171-207.

Drummond D.R., Carter N., Cross R.A. Multiphoton versus confocal high resolution z-sectioning of enhanced green fluorescent microtubules: increased multiphoton photobleaching within the focal plane can be compensated using a Pockels cell and dual widefield detectors. J Microsc 2002;206:161-169.

Egner A., Geisler C., von Middendorff C., Bock H., Wenzel D., Medda R., Andresen M., Stiel A.C., Jakobs S., Eggeling C., Schonle A., Hell S.W. Fluorescence nanoscopy in whole cells by asynchronous localization of photoswitching emitters. Biophys J 2007;93:3285-3290.

Egner A., Hell S.W. Fluorescence microscopy with super-resolved optical sections. Trends Cell Biol 2005;15:207-215.

Egner A., Jakobs S., Hell S.W. Fast 100-nm resolution three-dimensional microscope reveals structural plasticity of mitochondria in live yeast. Proc Natl Acad Sci U S A 2002;99:3370-3375.

Egner A., Schrader M., Hell S.W. Refractive index mismatch induced intensity and phase variations in fluorescence confocal, multiphoton and 4Pi-microscopy. Opt Commun 1998;153:211-217.

Egner A., Verrier S., Goroshkov A., Soling H.D., Hell S.W. 4Pi-microscopy of the Golgi apparatus in live mammalian cells. J Struct Biol 2004;147:70-76.

Elsner M., Hashimoto H., Nilsson T. Cisternal maturation and vesicle transport: join the band wagon! (Review). Mol Membr Biol 2003;20:221-229.

Farquhar M.G., Palade G.E. The Golgi apparatus (complex)-(1954-1981)-from artifact to center stage. J Cell Biol 1981;91:77s-103s.

Gallione C.J., Rose J.K. A single amino acid substitution in a hydrophobic domain causes temperature-sensitive cell-surface transport of a mutant viral glycoprotein. J Virol 1985;54:374-382.

Gillingham A.K., Munro S. Long coiled-coil proteins and membrane traffic. Biochim Biophys Acta 2003;1641:71-85.

Glick B.S. Organization of the Golgi apparatus. Curr Opin Cell Biol 2000;12:450-456.

Glick B.S., Elston T., Oster G. A cisternal maturation mechanism can explain the asymmetry of the Golgi stack. FEBS Lett 1997;414:177-181.

Glick B.S., Malhotra V. The curious status of the Golgi apparatus. Cell 1998;95:883-889.

Golgi C. On the structure of nerve cells. 1898. J Microsc 1898;155:3-7.

Gonzalez R., Woods R. Digital Image Processing. Addison-Wesley Publishing Company, 1992.

Graf R.F. Modern Dictionary of Electronics. Newnes, 1999.

Grubinger M., Gimona M. CRP2 is an autonomous actin-binding protein. FEBS Lett 2004;557:88-92.

Gugel H., Bewersdorf J., Jakobs S., Engelhardt J., Storz R., Hell S.W. Cooperative 4Pi excitation and detection yields sevenfold sharper optical sections in live-cell microscopy. Biophys J 2004;87:4146-4152.

Gustafsson M.G.L., Agard D.A., Sedat J.W. Sevenfold improvement of axial resolution in 3D widefield microscopy using two objective lenses. Proc. SPIE 1995;2412:147-156.

Hänninen P.E., Hell S.W., Salo J., Soini E., Cremer C. Two-photon excitation 4pi confocal microscope: Enhanced axial resolution microscope for biological research. Appl Phys Lett 1995;66:1698-1700.

Harwood R., Grant M.E., Jackson D.S. The route of secretion of procollagen. The influence of alphaalpha'-bipyridyl, colchicine and antimycin A on the secretory process in embryonic-chick tendon and cartilage cells. Biochem J 1976;156:81-90.

Hell S.W. Double-scanning confocal microscope. European Patent: S. W. Hell, 1990.

Hell S.W. Far-field optical nanoscopy. Science 2007;316:1153-1158.

Hell S.W. Toward fluorescence nanoscopy. Nat Biotechnol 2003;21:1347-1355.

Hell S.W., Schrader M., van der Voort H.T. Far-field fluorescence microscopy with three-dimensional resolution in the 100-nm range. J Microsc 1997;187:1-7.

Hell S.W., Stelzer E.H.K. Fundamental improvement of resolution with a 4Pi-confocal fluoresence microscope using two-photon exitation. Opt Commun 1992a;93:277-282.

Hell S.W., Stelzer E.H.K. Properties of a 4Pi-confocal fluorescence microscope. J Opt Soc Am 1992b;A9:2159-2166.

Hell S.W., Wichmann J. Breaking the diffraction resolution limit by stimulated emission: stimulated emission depletion microscopy. Opt. Lett. 1994;19:780-782.

Hess S.T., Girirajan T.P.K., Mason M.D. Ultra-High Resolution Imaging by Fluorescence Photoactivation Localization Microscopy. Biophys. J. 2006;91:4258-4272.

Hirschberg K., Miller C.M., Ellenberg J., Presley J.F., Siggia E.D., Phair R.D., Lippincott-Schwartz J. Kinetic analysis of secretory protein traffic and characterization of golgi to plasma membrane transport intermediates in living cells. J Cell Biol 1998;143:1485-1503.

Ho W.C., Allan V.J., van Meer G., Berger E.G., Kreis T.E. Reclustering of scattered Golgi elements occurs along microtubules. Eur J Cell Biol 1989;48:250-263.

Ho W.C., Storrie B., Pepperkok R., Ansorge W., Karecla P., Kreis T.E. Movement of interphase Golgi apparatus in fused mammalian cells and its relationship to cytoskeletal elements and rearrangement of nuclei. Eur J Cell Biol 1990;52:315-327.

Hofmann M., Eggeling C., Jakobs S., Hell S.W. Breaking the diffraction barrier in fluorescence microscopy at low light intensities by using reversibly photoswitchable proteins. Proc Natl Acad Sci U S A 2005;102:17565-17569.

Hueve J., Wesselmann R., Kahms M., Peters R. 4Pi microscopy of the nuclear pore complex. Biophys J 2008.

Humphrey W., Dalke A., Schulten K. VMD: visual molecular dynamics. J Mol Graph 1996;14:33-38, 27-38.

Jamieson J.D., Palade G.E. Intracellular transport of secretory proteins in the pancreatic exocrine cell. I. Role of the peripheral elements of the Golgi complex. J Cell Biol 1967;34:577-596.

Jaskolski F., Mulle C., Manzoni O.J. An automated method to quantify and visualize colocalized fluorescent signals. J Neurosci Methods 2005;146:42-49.

Kartberg F., Elsner M., Froderberg L., Asp L., Nilsson T. Commuting between Golgi cisternae--mind the GAP! Biochim Biophys Acta 2005;1744:351-363.

Khimich D., Nouvian R., Pujol R., Dieck S.T., Egner A., Gundelfinger E.D., Moser T. Hair cell synaptic ribbons are essential for synchronous auditory signalling. Nature 2005;434:889-894.

Kim Y.R., Peterkofsky B. Differential effects of ascorbate depletion and alpha,alpha'-dipyridyl treatment on the stability, but not on the secretion, of type IV collagen in differentiated F9 cells. J Cell Biochem 1997;67:338-352.

Krstic R. [Electron microscopic study of the striated muscle fibers in the pineal body of Wistar rats]. Z Zellforsch Mikrosk Anat 1972;128:227-240.

Ladinsky M.S., Mastronarde D.N., McIntosh J.R., Howell K.E., Staehelin L.A. Golgi structure in three dimensions: functional insights from the normal rat kidney cell. J Cell Biol 1999;144:1135-1149.

Lang M.C., Engelhardt J., Hell S.W. 4Pi microscopy with linear fluorescence excitation. Opt Lett 2007;32:259-261.

Lippincott-Schwartz J., Cole N., Presley J. Unravelling Golgi membrane traffic with green fluorescent protein chimeras. Trends Cell Biol 1998;8:16-20.

Lodish H.F., Kong N., Snider M., Strous G.J. Hepatoma secretory proteins migrate from rough endoplasmic reticulum to Golgi at characteristic rates. Nature 1983;304:80-83.

Losev E., Reinke C.A., Jellen J., Strongin D.E., Bevis B.J., Glick B.S. Golgi maturation visualized in living yeast. Nature 2006;441:1002-1006.

Majoul I., Straub M., Hell S.W., Duden R., Soling H.D. KDEL-cargo regulates interactions between proteins involved in COPI vesicle traffic: measurements in living cells using FRET. Dev Cell 2001;1:139-153.

Manders E.M.M., Verbeek F.J., Aten J.A. Measurement of co-localization of object in dual-colour confocal images. J Microsc 1993;169:375-382.

Marsh B.J., Howell K.E. The mammalian Golgi--complex debates. Nat Rev Mol Cell Biol 2002;3:789-795.

Marsh B.J., Mastronarde D.N., McIntosh J.R., Howell K.E. Structural evidence for multiple transport mechanisms through the Golgi in the pancreatic beta-cell line, HIT-T15. Biochem Soc Trans 2001;29:461-467.

Marsh B.J., Volkmann N., McIntosh J.R., Howell K.E. Direct continuities between cisternae at different levels of the Golgi complex in glucose-stimulated mouse islet beta cells. Proc Natl Acad Sci U S A 2004;101:5565-5570.

Martinez-Menarguez J.A., Prekeris R., Oorschot V.M., Scheller R., Slot J.W., Geuze H.J., Klumperman J. Peri-Golgi vesicles contain retrograde but not anterograde proteins consistent with the cisternal progression model of intra-Golgi transport. J Cell Biol 2001;155:1213-1224.

MATLAB. The MathWorks, Inc., R2006b.

Matsuura-Tokita K., Takeuchi M., Ichihara A., Mikuriya K., Nakano A. Live imaging of yeast Golgi cisternal maturation. Nature 2006;441:1007-1010.

Medda R., Jakobs S., Hell S.W., Bewersdorf J. 4Pi microscopy of quantum dot-labeled cellular structures. J Struct Biol 2006;156:517-523.

Mellman I., Simons K. The Golgi complex: in vitro veritas? Cell 1992;68:829-840.

Mironov A., Jr., Luini A., Mironov A. A synthetic model of intra-Golgi traffic. Faseb J 1998;12:249-252.

Mironov A.A., Beznoussenko G.V., Nicoziani P., Martella O., Trucco A., Kweon H.S., Di Giandomenico D., Polishchuk R.S., Fusella A., Lupetti P., Berger E.G., Geerts W.J., Koster A.J., Burger K.N., Luini A. Small cargo proteins and large aggregates can traverse the Golgi by a common mechanism without leaving the lumen of cisternae. J Cell Biol 2001;155:1225-1238.

Mironov A.A., Beznoussenko G.V., Polishchuk R.S., Trucco A. Intra-Golgi transport: a way to a new paradigm? Biochim Biophys Acta 2005;1744:340-350.

Mironov A.A., Weidman P., Luini A. Variations on the intracellular transport theme: maturing cisternae and trafficking tubules. J Cell Biol 1997;138:481-484.

Nagai T., Ibata K., Park E.S., Kubota M., Mikoshiba K., Miyawaki A. A variant of yellow fluorescent protein with fast and efficient maturation for cell-biological applications. Nat Biotechnol 2002;20:87-90.

Nagorni M., Hell S.W. 4Pi-confocal microscopy provides three-dimensional images of the microtubule network with 100- to 150-nm resolution. J Struct Biol 1998;123:236-247.

Nilsson T., Pypaert M., Hoe M.H., Slusarewicz P., Berger E.G., Warren G. Overlapping distribution of two glycosyltransferases in the Golgi apparatus of HeLa cells. J Cell Biol 1993;120:5-13.

O'Haver T.C. Potential clinical applications of derivative and wavelength-modulation spectrometry. Clin Chem 1979;25:1548-1553.

Ohto T., Uozumi N., Hirabayashi T., Shimizu T. Identification of novel cytosolic phospholipase A(2)s, murine cPLA(2){delta}, {epsilon}, and {zeta}, which form a gene cluster with cPLA(2){beta}. J Biol Chem 2005;280:24576-24583.

Orci L., Amherdt M., Ravazzola M., Perrelet A., Rothman J.E. Exclusion of golgi residents from transport vesicles budding from Golgi cisternae in intact cells. J Cell Biol 2000;150:1263-1270.

Orci L., Stamnes M., Ravazzola M., Amherdt M., Perrelet A., Sollner T.H., Rothman J.E. Bidirectional transport by distinct populations of COPI-coated vesicles. Cell 1997;90:335-349.

Ostermann J., Orci L., Tani K., Amherdt M., Ravazzola M., Elazar Z., Rothman J.E. Stepwise assembly of functionally active transport vesicles. Cell 1993;75:1015-1025.

Palade G. Intracellular aspects of the process of protein synthesis. Science 1975;189:347-358.

Patterson G.H., Hirschberg K., Polishchuk R.S., Gerlich D., Phair R.D., Lippincott-Schwartz J. Transport through the Golgi apparatus by rapid partitioning within a two-phase membrane system. Cell 2008;133:1055-1067.

Pawley J. Handbook of biological confocal microscopy, third edition. New York: SpringerScience Business Media, 2006.

Pistor S., Chakraborty T., Niebuhr K., Domann E., Wehland J. The ActA protein of Listeria monocytogenes acts as a nucleator inducing reorganization of the actin cytoskeleton. Embo J 1994;13:758-763.

Plecita-Hlavata L., Lessard M., Santorova J., Bewersdorf J., Jezek P. Mitochondrial oxidative phosphorylation and energetic status are reflected by morphology of mitochondrial network in INS-1E and HEP-G2 cells viewed by 4Pi microscopy. Biochim Biophys Acta 2008.

Polishchuk R.S., Polishchuk E.V., Marra P., Alberti S., Buccione R., Luini A., Mironov A.A. Correlative light-electron microscopy reveals the tubular-saccular ultrastructure of carriers operating between Golgi apparatus and plasma membrane. J Cell Biol 2000;148:45-58.

Rabouille C., Hui N., Hunte F., Kieckbusch R., Berger E.G., Warren G., Nilsson T. Mapping the distribution of Golgi enzymes involved in the construction of complex oligosaccharides. J Cell Sci 1995;108 (Pt 4):1617-1627.

Raman S., Maxwell C.A., Barcellos-Hoff M.H., Parvin B. Geometric approach to segmentation and protein localization in cell culture assays. J Microsc 2007;225:22-30.

Rambourg A., Clermont Y. Three-dimensional electron microscopy: structure of the Golgi apparatus. Eur J Cell Biol 1990;51:189-200.

Rambourg A., Clermont Y., Kepes F. Modulation of the Golgi apparatus in Saccharomyces cerevisiae sec7 mutants as seen by three-dimensional electron microscopy. Anat Rec 1993;237:441-452.

Richardson W.H. Bayesian-based iterative method of image restoration. J. Opt. Soc. Am. 1972;62:55-59.

Roth J., Berger E.G. Immunocytochemical localization of galactosyltransferase in HeLa cells: codistribution with thiamine pyrophosphatase in trans-Golgi cisternae. J Cell Biol 1982;93:223-229.

Rothman J.E., Miller R.L., Urbani L.J. Intercompartmental transport in the Golgi complex is a dissociative process: facile transfer of membrane protein between two Golgi populations. J Cell Biol 1984a;99:260-271.

Rothman J.E., Urbani L.J., Brands R. Transport of protein between cytoplasmic membranes of fused cells: correspondence to processes reconstituted in a cell-free system. J Cell Biol 1984b;99:248-259.

Rust M.J., Bates M., Zhuang X. Sub-diffraction-limit imaging by stochastic optical reconstruction microscopy (STORM). Nat. Methods 2006;3:793-796.

Sarras M.P., Jr., Meador D., Zhang X.M. Extracellular matrix (mesoglea) of Hydra vulgaris. II. Influence of collagen and proteoglycan components on head regeneration. Dev Biol 1991;148:495-500.

Schrader M., Bahlmann K., Giese G., Hell S.W. 4Pi-confocal imaging in fixed biological specimens. Biophys J 1998;75:1659-1668.

Shapiro L.G., Stockman G.C. Computer vision. Prentice-Hall, 1992.

Slusarewicz P., Nilsson T., Hui N., Watson R., Warren G. Isolation of a matrix that binds medial Golgi enzymes. J Cell Biol 1994;124:405-413.

Storrie B., Nilsson T. The Golgi apparatus: balancing new with old. Traffic 2002;3:521-529.

Tanaka K., Fukudome H. Three-dimensional organization of the Golgi complex observed by scanning electron microscopy. J Electron Microsc Tech 1991;17:15-23.

Tanaka K., Mitsushima A., Fukudome H., Kashima Y. Three-dimensional architecture of the Golgi complex observed by high resolution scanning electron microscopy. J Submicrosc Cytol 1986;18:1-9.

Trucco A., Polishchuk R.S., Martella O., Di Pentima A., Fusella A., Di Giandomenico D., San Pietro E., Beznoussenko G.V., Polishchuk E.V., Baldassarre M., Buccione R., Geerts W.J., Koster A.J., Burger K.N., Mironov A.A., Luini A. Secretory traffic triggers the formation of tubular continuities across Golgi sub-compartments. Nat Cell Biol 2004;6:1071-1081.

Tsien R.Y. The green fluorescent protein. Annu Rev Biochem 1998;67:509-544.

Volchuk A., Amherdt M., Ravazzola M., Brugger B., Rivera V.M., Clackson T., Perrelet A., Sollner T.H., Rothman J.E., Orci L. Megavesicles implicated in the rapid transport of intracisternal aggregates across the Golgi stack. Cell 2000;102:335-348.

Weidman P., Roth R., Heuser J. Golgi membrane dynamics imaged by freeze-etch electron microscopy: views of different membrane coatings involved in tubulation versus vesiculation. Cell 1993;75:123-133.

White J., Keller P., Stelzer E.H. Spatial partitioning of secretory cargo from Golgi resident proteins in live cells. BMC Cell Biol 2001;2:19.

Yeo K.T., Parent J.B., Yeo T.K., Olden K. Variability in transport rates of secretory glycoproteins through the endoplasmic reticulum and Golgi in human hepatoma cells. J Biol Chem 1985;260:7896-7902.

Young T.Y., Gerbrands J.J., van Vliet L.J. Fundamentals of Image Processing. 1995.

Zimmermann T., Rietdorf J., Pepperkok R. Spectral imaging and its applications in live cell microscopy. FEBS Letters 2003;546:87-92.

Acknowledgments

I wish to thank Dr. Roberto Buccione as the Coordinator of the PhD Programme within the Consorzio Mario Negri Sud, as well as my external Supervisor, Prof. Chris Hawes, for his excellent support. Thanks also go to the staff of the Department of NanoBiophotonics at the Max-Planck-Institute for their fundamental contribution to this study.

Apart from these collaborative experiences in my PhD training, I wish to thank all of the best friends I have ever meet at the Mario Negri Sud for sharing good times together, and especially Raman, Alex, Oliviano and Meri for our coffee breaks and pleasant chats, Massimo for having been my flatmate, and Daniele and Fabio for all of the wonderful "Abruzzese" dinners we have had of late. It is a pleasure to me to remember also the fun times I had with Alessio and Mariagrazia when we were all still working in the Laboratory. Special mentions go to Enry, for having introduced me to microscopy, to Mariella, for having been my patient neighbour, to Annalisa, for having taught me many culinary "tricks", and to Viviana, one of the most sincere and frank people I have ever meet.

At the end of this intense step in my career, I wish to mention Prof. Giuseppe Spoto and Prof. Michele Paolantonio, who initially believed and invested in my scientific development, from when I was only in the first year of my dental studies.

Finally, I would like to leave my very last acknowledgment to Chris Berrie, a real English Gentlemen and a fine Scientist, who has contributed more then anyone else to my scientific growth, even long before my PhD training, and to whom I owe a significant part of my success.